FACULTY
OF MATHEMATICS
AND PHYSICS
Charles University

and University of Strasbourg

DOCTORAL THESIS

Vít Kučera

Study of strange particle production in jets with the ALICE experiment at the LHC

Institute of Particle and Nuclear Physics

Supervisors of the doctoral thesis:	RNDr. Jana Bielčíková, Ph.D., Dr. Christian Kuhn
Study programme:	Physics
Study branch:	Subnuclear Physics

Prague 2016

I declare that I carried out this doctoral thesis independently, and only with the cited sources, literature and other professional sources.

I understand that my work relates to the rights and obligations under the Act No. 121/2000 Sb., the Copyright Act, as amended, in particular the fact that the Charles University has the right to conclude a license agreement on the use of this work as a school work pursuant to Section 60 subsection 1 of the Copyright Act.

In Prague, 22 August 2016   Vít Kučera

Title: Study of strange particle production in jets with the ALICE experiment at the LHC

Author: Vít Kučera

Institute: Institute of Particle and Nuclear Physics

Supervisors: RNDr. Jana Bielčíková, Ph.D., Nuclear Physics Institute of the CAS; Dr. Christian Kuhn, Institut Pluridisciplinaire Hubert CURIEN

Abstract: Quark–gluon plasma is a state of matter existing under extreme energy densities and temperatures where quarks and gluons are deconfined. Complex phenomena occurring in the plasma emerge from the strong interaction of its constituents. This hot and dense strongly interacting matter can be created in ultra-relativistic heavy-ion collisions and its properties can be studied by measuring particles produced in the collisions. Partons produced in hard scatterings interact with the medium which modifies the production of particles in jets. Measurements of spectra of identified particles produced in jets represent an important tool for understanding the interplay of various hadronization mechanisms which contribute to the particle production in the medium created in heavy-ion collisions. In this thesis, we present the measurement of the p_{T} spectra of Λ baryons and $\mathrm{K}^0_{\mathrm{S}}$ mesons produced in charged jets in central Pb–Pb collisions at the energy $\sqrt{s_{\mathrm{NN}}} = 2.76\,\mathrm{TeV}$, measured in the ALICE experiment at the LHC. The results of the analysis are used to discuss the origin of the enhancement of the baryon-to-meson ratio observed for the inclusive production of light-flavour particles in heavy-ion collisions.

Keywords: ALICE, heavy-ion collisions, jets, fragmentation, strange particles, baryon-to-meson ratio

Acknowledgments

Contents

Introduction

According to the current level of understanding, our Universe came into existence in an event called the Big Bang. In this initial moment of the evolution of the Universe, extreme conditions (high energy densities and temperatures) were present. During a period which lasted up to several microseconds after the beginning of the Universe, the most fundamental known constituents of nuclear matter, quarks, anti-quarks and gluons, were deconfined in a state called "quark–gluon plasma" (QGP). Only later, when the Universe cooled down, the energy density dropped below the critical value and quarks, anti-quarks and gluons could be clustered by the strong interaction into the first hadrons which then formed the first atomic nuclei. This energy of the strong interaction binding the constituents of matter into hadrons is at the origin of most of the mass of the visible matter in the Universe.

The strong interaction is described by Quantum Chromodynamics (QCD), a theory which allows to derive characteristics of the basic processes with an extraordinary precision. Predictions of the QCD calculations have been extensively verified experimentally over several decades in particle collisions at high energies in many research facilities.

In systems containing many particles, the strong interaction gives origin to phenomena that are difficult to derive from the theory. Collective phenomena emerging from the interaction of quarks and gluons can be studied in larger systems of particles created in ultra-relativistic collisions of atomic nuclei (heavy-ion collisions) which enable probing different regions of the phase diagram of the strongly interacting matter. The most revealing results in this field have been provided in the last few decades by the measurements of heavy-ion collisions at the Super Proton Synchrotron (SPS) at the European Organization for Nuclear Research (CERN), the Relativistic Heavy Ion Collider (RHIC) in Brookhaven National Laboratory and the Large Hadron Collider (LHC) at CERN. Existence of QGP is predicted by QCD and experiments carried out at these colliders confirmed that QGP can be recreated and studied in laboratory conditions. Results of studying QGP in heavy-ion collisions have shown that this strongly coupled medium behaves like an almost perfect liquid.

Properties of the hot and dense strongly interacting matter created in heavy-ion collisions may be studied by using jets. Production of jets is well described theoretically and occurs at the early stages of the collision. When propagating through the medium created in a heavy-ion collision, jets are modified by interaction with this medium and therefore can be used as probes for measuring properties of QGP. Studying the medium in heavy-ion collisions is the main task of the ALICE experiment at the LHC. Its performance enables to carry out this task using different probes including fully reconstructed jets and identified particles over a wide range of momentum.

In heavy-ion collisions, the ratio between the inclusive production of baryons and mesons measured for light-flavour particles at intermediate transverse momenta ($2\,\mathrm{GeV}/c \lesssim p_\mathrm{T} \lesssim 6\,\mathrm{GeV}/c$) is observed to be enhanced with respect to the ratio measured in proton–proton (p–p) collisions. The origin of the enhancement of the baryon-to-meson ratio is not completely explained and might

be better unravelled by measuring production of hadrons from individual sources that contribute to the total bulk of particles. Measurements of the production of individual particle species in jets provide a more detailed insight into the interplay of hadronization mechanisms in heavy-ion collisions and allow to determine how the presence of the QGP modifies the process of jet fragmentation.

This doctoral thesis presents a study of the production of neutral strange particles K_S^0 and Λ in charged jets reconstructed in lead–lead (Pb–Pb) collisions at the centre-of-mass energy per nucleon pair $\sqrt{s_{NN}} = 2.76$ TeV recorded with ALICE in 2011.

In Chapter 1, I first introduce the basic concepts of the theory of the strong interaction and the motivation for studying heavy-ion collisions. Then I explain how the interaction of jets with the medium in heavy-ion collisions is theoretically described and how it can be measured in experiments. I mention potential hadronization mechanisms in the QGP and introduce the enhancement of the baryon-to-meson ratio as a motivation for studying the production of strange particles in jets. Chapter 2 is dedicated to the presentation of the ALICE experiment. The main detectors are described and their performance is specified. I also briefly explain the procedures of event characterization and the reconstruction of momenta of detected particles. In Chapter 3, I present the service task project consisting in performing characterization tests for determining the performance of prototypes of the ALPIDE chips designed for the upgrade of the tracking detectors of the ALICE experiment. In Chapter 4, I describe the structure of the analysis of the production of neutral strange particles in jets in Pb–Pb collisions. The steps of the analysis are explained in detail, including reconstruction of the strange particles, reconstruction of jets, association of particles with jets, application of corrections and evaluation of systematic uncertainties. Results of the analysis are presented in Chapter 5. Spectra of neutral strange particles in jets and their ratios are presented, described, interpreted and compared with results of other related analyses. Limitations and ideas for potential improvements are discussed. In the conclusion, I summarize the analysis and mention the main findings following from the presented results.

1. Theoretical introduction

1.1 Quantum chromodynamics

Quantum chromodynamics (QCD) is a theory that describes the strong interaction between quarks and gluons. Quarks and gluons together are referred to as partons. Quarks are massive fermions with spin one half. They appear in six flavours and represent the most fundamental known constituents of nuclear matter. Gluons are massless bosons with spin one which mediate strong interaction between quarks. The charge of the strong interaction is called "colour" and it can take three values (labelled commonly as red, green and blue) for quarks and three opposite values ("anti-colours") for anti-quarks. Gluons are not only mediators of the interaction but carry themselves eight combinations of colours and anti-colours which allows them to interact with each other. By exchanging gluons, quarks are kept together inside colourless particles called hadrons.

1.1.1 The QCD Lagrangian

QCD is a non-Abelian gauge theory with gauge group of symmetry SU(3). In the formalism of quantum field theory, the Lagrangian density of QCD is expressed as:

$$\mathcal{L}_{\text{QCD}} = \sum_f \overline{\psi}_{f,i} \left(i\boldsymbol{\gamma}^\mu D_{\mu,ij} - m_f \delta_{ij} \right) \psi_{f,j} - \frac{1}{4} F_{\mu\nu}^a F^{a,\mu\nu}, \tag{1.1}$$

where $\psi_{f,i}$ is a quark-field spinor for a quark of flavour f and colour i with mass m_f, $\boldsymbol{\gamma}^\mu$ are the Dirac γ-matrices, $D_{\mu,ij}$ is the covariant derivative, δ_{ij} is the Kronecker delta, $\boldsymbol{F}^a$ is a gluon-field tensor for a gluon of colour combination a. The covariant derivative in QCD is expressed as:

$$D_{\mu,ij} = \partial_\mu \delta_{ij} - i g_{\text{s}} t_{ij}^a A_\mu^a, \tag{1.2}$$

where g_{s} is the QCD coupling constant, $\boldsymbol{t}^a$ are eight 3×3 matrices which correspond to generators of the SU(3) colour group, A^a are eight gluon fields corresponding to gluons of different colour combinations. Elements of the gluon-field tensors $\boldsymbol{F}^a$ have the following form:

$$F_{\mu\nu}^a = \partial_\mu A_\nu^a - \partial_\nu A_\mu^a + g_{\text{s}} f^{abc} A_\mu^b A_\nu^c, \tag{1.3}$$

where f^{abc} are the structure constants of the SU(3) group [1]. The Lagrangian density is invariant under local gauge transformations.

1.1.2 The coupling constant of the strong interaction

In the calculations, the coupling constant is usually referred to as α_{s} which is related to g_{s} by the relation

$$\alpha_{\text{s}} = \frac{g_{\text{s}}^2}{4\pi}. \tag{1.4}$$

Cross sections of QCD processes and related quantities can be calculated using techniques of the perturbation theory if the coupling constant is small enough. However, this is not always the case for the strong interaction.

QCD is a renormalizable theory which allows to handle infinite contributions from integrals in loop diagrams by redefining the parameters and fields used in the theory. The renormalized coupling constant becomes a function of a renormalization scale μ. The scale is an unphysical parameter that must not affect results of calculations of observable quantities which are expressed in terms of the renormalized coupling constant [1]. Strength of the strong interaction in a process with a transfer of 4-momentum Q is given by evaluating the coupling constant at $\mu \approx Q$ [1] which means that the value of the coupling constant for a particular QCD process depends on the energy scale of the interaction. This behaviour is known as running of the coupling constant. The dependence of the renormalized coupling constant on the renormalization scale is expressed by the β-function in the renormalization group equation [1]

$$\beta(\alpha_{\mathrm{s}}(\mu)) \stackrel{\text{def}}{=} \mu^2 \frac{\mathrm{d}\alpha_{\mathrm{s}}(\mu)}{\mathrm{d}\mu^2} = -(b_0 \alpha_{\mathrm{s}}^2 + b_1 \alpha_{\mathrm{s}}^3 + \ldots). \tag{1.5}$$

The coefficient b_0 of the lowest-order term can be expressed as [1]

$$b_0 = (33 - 2n_{\mathrm{f}})/12\pi > 0, \tag{1.6}$$

where n_{f} is the number of quark flavours in loop diagrams considered to be light (i.e. $m_f \ll \mu$) [1]. The non-Abelian nature of QCD reflects the gluon self-interaction which makes the β-function negative [2]. As a result, the coupling constant is decreasing with increasing transfer Q of 4-momentum in the interaction. In the approximation of considering only the lowest-order term of the β-function, we have [1, 2]

$$\alpha_{\mathrm{s}}(Q) \approx \frac{1}{b_0 \ln(Q^2/\Lambda_{\mathrm{QCD}}^2)}, \tag{1.7}$$

where $\Lambda_{\mathrm{QCD}} \approx 200\,\mathrm{MeV}$ is a scale parameter that depends on μ and indicates the energy scale at which α_{s} is large, i.e. QCD becomes non-perturbative and the perturbative QCD calculations are no longer reliable [2]. This behaviour can be interpreted as an anti-screening of the colour charge at small distances and it has been confirmed by numerous measurements of various interactions. The results of measurements of the coupling constant are summarized in Fig. 1.1.

In long-distance interactions (involving small momentum transfers, roughly below $1\,\mathrm{GeV}$), QCD processes are governed by the non-perturbative regime at large α_{s}. This corresponds to conditions where quarks are confined in bound systems and where fragmentation functions, parton distribution functions or calculations of QCD on lattice can be used. Although not proved yet within the theory, the colour confinement is believed to be an essential feature of QCD and responsible for preventing quarks and gluons from getting isolated and observed as free particles. The idea that the intensity of the strong interaction between quarks increases with distance is supported by the experimental evidence which suggests that it is impossible to directly observe an isolated quark and measure its properties.

If the interaction distance between quarks becomes small enough, which corresponds to processes involving large momentum transfers, the strong interaction becomes weak and in the limit of infinite energies vanishes completely:

$$\alpha_{\mathrm{s}}(Q) \stackrel{Q \longrightarrow \infty}{\Longrightarrow} 0. \tag{1.8}$$
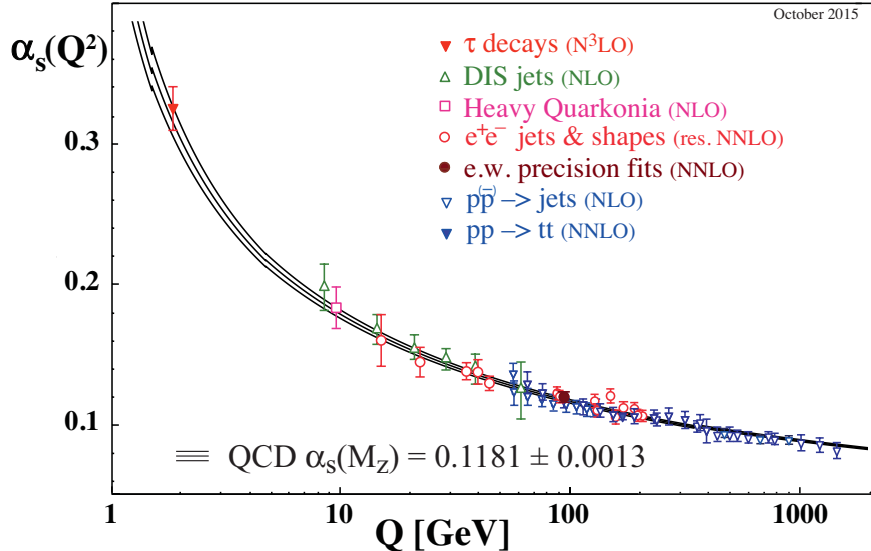
Figure 1.1: Summary of measurements of α_s as a function of the energy scale Q [1].

This phenomenon is called asymptotic freedom because the interaction between quarks becomes so weak that they are no longer coupled and their relative motion is almost free.

The small value of the coupling constant enables performing very accurate calculations using perturbation theory. For this reason collisions of particles at high energies are very important for verifying predictions of perturbative QCD (pQCD).

1.1.3 Quark–gluon plasma and the QCD phase diagram

A direct consequence of the asymptotic freedom in QCD is the prediction of a possible phase transition from hadronic matter at low energies to a state of quark–gluon plasma (QGP) at high temperatures and/or high energy densities. Such extreme conditions would essentially "melt" hadrons and make quarks and gluons deconfined and free to move in the whole volume of the QGP. Current theories suggest that for some microseconds after the Big Bang, our Universe was filled with QGP [3]. That makes studies of the QGP important also for better understanding of the early stages of the evolution of our Universe.

Different phases of strongly interacting matter and transitions between them can be represented as regions in the phase diagram as a function of baryon chemical potential μ_B and temperature T. Figure 1.2 shows the phase diagram of strongly interacting matter together with labels indicating approximate regions explored using different accelerators.

Parameters of the phase transition and properties of the plasma are calculated using techniques of the lattice QCD. Calculations suggest that the critical energy density for deconfinement is $e_c \approx 0.6$–$0.7\,\mathrm{GeV/fm^3}$ [3] and the critical temperature is $T_c \approx 150$–$170\,\mathrm{MeV}$ [3, 5, 6]. According to the results from the lattice QCD, the transition at $\mu_B = 0$ from hadron resonance gas to QGP at T_c is rather a rapid but continuous crossover whereas at non-zero values of the potential μ_B the boundary between hadron gas and QGP is expected to become a first order transition
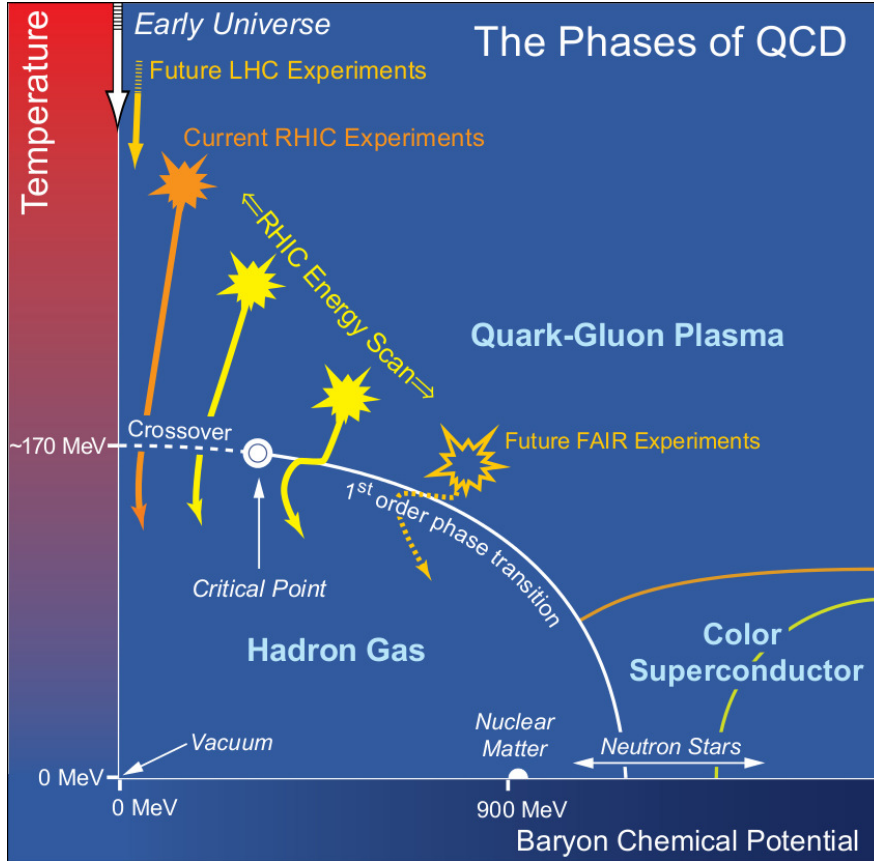
Figure 1.2: Phase diagram of strongly interacting matter [4].

represented in the diagram by a critical line with constant critical energy density, ended by a critical point at low μ_B [3]. The nature of the transition and its exact location in the diagram are still subject to further calculations and experimental research.

As the nuclear matter changes into plasma during the deconfinement around the critical temperature, the dynamically-generated masses of quarks vanish and approximate chiral symmetry in QCD is restored as quarks become lighter. At temperatures above the critical temperature, the deconfinement leads to the release of a large number of gluons which can produce additional pairs of quarks and anti-quarks. This process is facilitated by the decrease of quark masses and allows the system to reach chemical equilibrium among light-flavour quarks, anti-quarks and gluons which is important especially for the production of strange quarks. The dissolution of massive hadrons into almost massless quarks and gluons represents a significant increase of the number of degrees of freedom which is accompanied by a rapid rise of the ratio e/T^4 [3].

Significant progress in studying the QCD diagram has been made over the last few decades using ultra-relativistic collisions of atomic nuclei (heavy ions). Before a heavy-ion collision, the matter in nuclei is situated at the coordinates of the cold nuclear matter at $T = 0$ and $\mu_B \approx 940\,\mathrm{MeV}$ in the diagram. Right after the collision, the matter goes through an early non-equilibrium stage (which cannot be mapped onto the phase diagram) and after thermalizing reappears in the diagram at a high temperature [3]. When the centre-of-mass energy per nucleon is larger than about $100\,\mathrm{GeV}$, the colliding nuclei tend to pass through each other

and the matter produced between the receding nuclei has a high energy density and temperature but a low baryon density [7]. With increasing the centre-of-mass energy of the collision, a decreasing fraction of the energy of incoming baryons gets stopped in the centre-of-mass system. The bulk of matter created in the collision ("fireball") therefore contains relatively fewer of the original baryons which balances the ratio between the numbers of baryons and anti-baryons and lowers the potential μ_B [3]. The matter then cools down and, if QGP was created, passes through the hadronization phase transition where quarks and gluons undergo confinement binding them back into hadrons and the system eventually reaches back the region of hadronic matter. The trajectory corresponding to the cooling of the early Universe follows the temperature axis at $\mu_B \approx 0$.

Results of measurements of heavy-ion collisions at different energies have confirmed that QGP can be recreated in laboratory conditions and extensively studied. First evidence of creating a new state of strongly interacting matter featuring signatures of QGP was observed in 2000 at the Super Proton Synchrotron (SPS) at The European Organization for Nuclear Research (CERN) in collisions of lead beams at energy $158\,\mathrm{GeV}$ per nucleon with fixed targets [8, 9]. Creation of QGP in heavy-ion collisions was announced as confirmed first in 2010 based on the results from collisions of gold ions at the Relativistic Heavy Ion Collider (RHIC) in Brookhaven National Laboratory [10]. Measurements of collisions at RHIC have shown that the QGP behaves as nearly perfect freely flowing liquid composed of strongly interacting quarks and gluons [10] and brought many important results extending our knowledge about properties of the QGP. In 2010, the Large Hadron Collider (LHC) at CERN joined this effort with its programme of colliding lead nuclei at the centre-of-mass energy per nucleon pair $\sqrt{s_{\mathrm{NN}}} = 2.76\,\mathrm{TeV}$. After an increase of performance, enabled by the upgrade in years 2013–2014, the LHC produced collisions at $\sqrt{s_{\mathrm{NN}}} = 5.02\,\mathrm{TeV}$ during Run 2 in 2015.

1.2 Heavy-ion collisions

1.2.1 Evolution of a heavy-ion collision

Ultra-relativistic heavy-ion collisions allow to create a volume of QGP large enough to study properties of this state of matter. Heavy-ion collisions have been studied at several accelerators with different energies which has provided results of measurements at different values of temperature and baryon chemical potential. This diversity thus allows one to probe different regions of the phase diagram of strongly interacting matter.

In the very early (pre-equilibrium) stages of a relativistic heavy-ion collision, particles with large transverse momenta ($p_T \gg 1\,\mathrm{GeV}/c$) or large masses are produced in hard processes involving large momentum transfers ($Q^2 \gg 1\,\mathrm{GeV}^2$). Using the uncertainty relation, one can estimate that this production occurs at a time scale of the order of $0.1\,\mathrm{fm}/c$. Partons created in the collision rescatter off each other and create hot and dense strongly interacting matter with large energy density. This matter reaches local thermal equilibrium after about $1\,\mathrm{fm}/c$ of proper time (τ) and becomes a QGP. The thermalized bulk of partons has thermal pressure which causes a collective hydrodynamic expansion. Expansion makes matter in the fireball cool down and decreases its energy density. When

the energy density reaches the critical value at $\tau \approx 10$–$15\,\mathrm{fm}/c$, phase transition occurs and partons convert to hadrons. At this stage, the final abundance of hadrons of different species is fixed which is called "chemical freeze-out". After hadronization, hadrons keep rescattering with each other elastically and through resonances, average distance between hadrons increases and the matter becomes more dilute. When the average distance between hadrons exceeds the typical interaction distance of the strong interaction, elastic scattering stops and hadrons decouple. This stage is called "kinetic freeze-out" [3].

1.2.2 Centrality

Properties and spatial distribution of particles created in heavy-ion collisions depend strongly on the initial geometry of the system of colliding nuclei. The basic parameter characterizing the size and shape of the interaction region is the impact parameter b which can be defined as the distance between centres of colliding nuclei in the transverse plane with respect to the collision axis. Since the impact parameter cannot be measured directly, related quantities that can be estimated from measurements are used for describing the geometry of a collision.

The most relevant quantity that allows to discriminate collisions with different impact parameters is centrality.

Centrality is expressed as a percentage of the total cross section of the interaction of two nuclei [11]. The most central collisions (corresponding to $b \approx 0$) are labelled with centrality of $0\,\%$ and the most peripheral collisions have centrality of $100\,\%$.

In order to establish a relation between centrality and the impact parameter, collision geometry has to be described using a model. A Glauber model [12, 13] is usually used for this purpose. A Glauber model allows to simulate spatial distribution of nucleons during the collisions and to calculate the corresponding impact parameter b, the number of participating nucleons N_{part} (i.e. nucleons which undergo at least one inelastic nucleon–nucleon collision) and the number of binary collisions of nucleons N_{coll} [13]. Soft processes are sensitive to the value of N_{part}, whereas N_{coll} is the scale for the hard processes [3]. According to QCD, hard particles are produced on short time scales and their production in the nucleon collisions therefore happens incoherently [3], so the nucleus–nucleus collision may be considered a superposition of independent nucleon–nucleon interactions [13, 14]. The production of partons with high transverse momenta p_{T} can therefore be calculated perturbatively and is proportional to the number of binary nucleon–nucleon collisions [3]. The parameters of the Glauber model can be used as input for models of charged-particle production in order to estimate the number of charged particles created in the collision. The simulated distribution of the number of charged particles may be mapped on the measured signal response of a detector which allows to determine centrality classes and relate them with intervals of impact parameter values [13].

The formalism used to describe the geometry of a collision of two nuclei is introduced in Fig. 1.3. The impact parameter of nuclei A and B is expressed by a vector $\boldsymbol{b}$ lying in the transverse plane. The coordinates of a point in the transverse plane are determined by a vector $\boldsymbol{s}$ relative to the centre of the nucleus A and by a vector $\boldsymbol{s} - \boldsymbol{b}$ relative to the centre of the nucleus B.
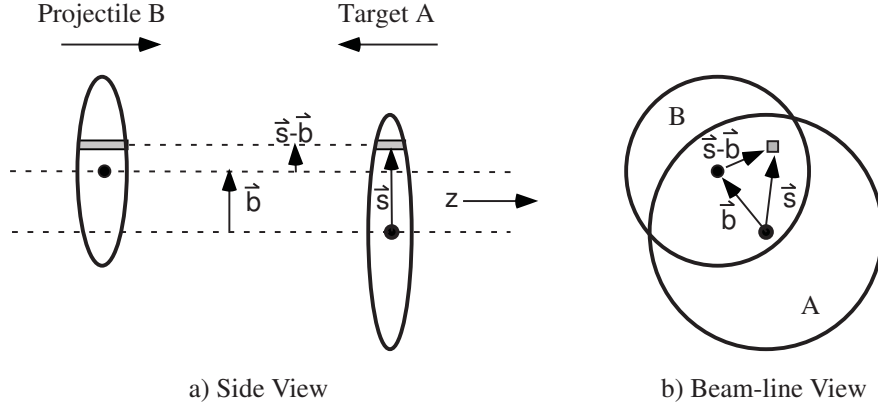
a) Side View   b) Beam-line View

Figure 1.3: Schematic representation of the Optical Glauber Model geometry, with transverse (a) and longitudinal (b) views [13].

Let $\rho_\mathrm{A}(\boldsymbol{s}, z_\mathrm{A})$ be the probability density of finding a given nucleon from the nucleus A at the space point $(\boldsymbol{s}, z_\mathrm{A})$ where z_A is the relative longitudinal coordinate within the nucleus A. This function is given by the Woods–Saxon nuclear density profile [14]. The probability density of that nucleon being located at point $\boldsymbol{s}$ is obtained by integrating over z_A as [13]

$$T_\mathrm{A}(\boldsymbol{s}) = \int_\mathrm{A} \rho_\mathrm{A}(\boldsymbol{s}, z_\mathrm{A})\,\mathrm{d}z_\mathrm{A}. \tag{1.9}$$

An analogous expression follows for a nucleon from the nucleus B. The probability density of finding both nucleons at the same point in the transverse plane for a given impact parameter $\boldsymbol{b}$ is given by the "thickness function" T_AB which can be obtained as a convolution [13]

$$T_\mathrm{AB}(\boldsymbol{b}) = \int T_\mathrm{A}(\boldsymbol{s})T_\mathrm{B}(\boldsymbol{s} - \boldsymbol{b})\,\mathrm{d}^2 s. \tag{1.10}$$

If the nuclei are not polarized, the thickness function depends only on the scalar impact parameter b. For $\sigma_\mathrm{NN}^\mathrm{inel}$ being the cross section of an inelastic nucleon–nucleon interaction, the probability of such interaction is then $T_\mathrm{AB}(b)\sigma_\mathrm{NN}^\mathrm{inel}$. The resulting number of nucleon–nucleon collisions for a collision of nucleus A composed of A nucleons and nucleus B composed of B nucleons is then [13]

$$N_\mathrm{coll}(b) = AB T_\mathrm{AB}(b)\sigma_\mathrm{NN}^\mathrm{inel}. \tag{1.11}$$

The number of participating nucleons can be calculated using a more complicated expression [13]:

$$N_\mathrm{part}(\boldsymbol{b}) = A \int T_\mathrm{A}(\boldsymbol{s}) \left\{ 1 - \left[1 - T_\mathrm{B}(\boldsymbol{s} - \boldsymbol{b})\sigma_\mathrm{NN}^\mathrm{inel} \right]^B \right\} \mathrm{d}^2 s +$$
$$+ B \int T_\mathrm{B}(\boldsymbol{s} - \boldsymbol{b}) \left\{ 1 - \left[1 - T_\mathrm{A}(\boldsymbol{s})\sigma_\mathrm{NN}^\mathrm{inel} \right]^A \right\} \mathrm{d}^2 s. \tag{1.12}$$

1.3 Jets

1.3.1 Production of jets in QCD

In the framework of QCD, a jet is a cascade of successive emissions of partons induced by a parton created in an initial hard scattering [14, Sec. 6.8]. A high-p_T

parton produced in a hard scattering has a large virtuality Q which decreases by parton showering as the parton subsequently radiates gluons and/or splits into quark–anti-quark pairs. Such a parton branching evolution is governed by the DGLAP evolution equations down to low virtualities ($Q \approx 1\,\mathrm{GeV}$) when the parton converts by the non-perturbative process of fragmentation into a collimated spray of final-state hadrons which is called a jet [1, 2, 15]. The parton showering and the subsequent hadronization are together referred to as parton fragmentation [14, Sec. 6.8]. Hard partons are typically produced in pairs and emitted back-to-back in the centre-of-mass system of that pair which leads to the observation of a pair of jets going in opposite directions (in the centre-of-mass system) [3].

In hadronic interactions, jets are produced by the hard scattering of the constituent partons of the colliding hadrons. Production of high-p_{T} hadrons in elementary collisions ($\mathrm{e^-} + \mathrm{e^+}$, $\mathrm{p} + \mathrm{p}$, $\mathrm{p} + \overline{\mathrm{p}}$) is quite well understood and can be described using factorization theorems [3, 16]. The cross section can be factorized into a perturbative (short-distance) part and a non-perturbative (long-distance) part [2]. Therefore the partonic process with a large momentum transfer can be described as the convolution of the parton distribution functions (PDFs) of partons in colliding hadrons, a hard parton scattering and fragmentation functions (FFs) of the produced partons [16]. The same formalism can be applied for collisions of nuclei. Production of a hard hadron h in a high-energy hadron–hadron or nucleus–nucleus collision $A + B$ can be calculated as [15]

$$\mathrm{d}\sigma^{\mathrm{hard}}_{AB \to h} = f_{a/A}(x_a, Q^2) \otimes f_{b/B}(x_b, Q^2) \otimes \mathrm{d}\sigma^{\mathrm{hard}}_{ab \to c}(x_a, x_b, Q^2) \otimes D_{c \to h}(z, Q^2), \quad (1.13)$$

where $\sigma^{\mathrm{hard}}_{ab \to c}(x_a, x_b, Q^2)$ is the perturbative cross section of the hard partonic process $a + b \to c + X$, $f_{a/A}(x, Q^2)$ is the parton distribution function (PDF) related to the probability of finding a parton of flavour a inside the projectile A carrying momentum fraction $x = p_a/p_A$ of the projectile momentum, $D_{c \to h}(z, Q^2)$ is the fragmentation function related to the probability that the parton c fragments into a hadron h with a momentum fraction $z = p_h/p_c$ of the parton momentum.

Parton distribution functions and fragmentation functions are non-perturbative distributions which are assumed to be universal (process-independent), depend on the factorization scale, can be evolved by DGLAP equations and can be determined experimentally by global fits to data from measurements of elementary collisions [15, 16].

1.3.2 Parton interaction in medium

Partons with large transverse momenta are produced at the early (pre-equilibrium) stage of heavy-ion collisions during hard processes with large transfers of momentum which occur on short time scales before QGP is formed. That allows to calculate their production using pQCD. In a central collision between two lead nuclei, the reaction region has a transverse diameter of about $12\,\mathrm{fm}$, so a hard particle created near the edge and moving inwards needs roughly $12\,\mathrm{fm}/c$ before it reaches the other side of the region (if the medium is not expanding quickly). That provides enough time for probing all evolution stages of the medium as the hard particle scatters off the evolving medium and loses energy while propagating to the opposite border of the fireball [3]. A hard parton eventually converts by fragmentation into a shower of hadrons which can be observed as a jet.

A hard parton with $E \gg 1\,\mathrm{GeV}$ traversing the dense matter produced in heavy-ion collisions loses energy mainly by gluon radiation induced by multiple scattering off the medium. The colour charge of the fast parton interacts with the colour charges of the constituents of the medium and makes the parton emit a much softer bremsstrahlung gluon which in turn interacts with the colour charges in the medium. The reinteractions of the emitted gluon with the medium are characterized by a mean free path λ_g [3, 14]. A theoretical description of this mechanism of energetic losses in the strongly interacting medium was first proposed by Baier, Dokshitzer, Mueller, Peigné and Schiff in their BD-MPS model [3, 17–19]. In a simplified picture, the medium is considered to be a static set of scattering centres with Debye screened Coulomb potentials, and with a corresponding Debye screening mass μ, [18] distributed with a spatial density ρ within a volume of a finite size. Multiple scatterings that the parton undergoes in the dense medium are characterized as a sequence of independent random events with a mean free path [17, 18]

$$\lambda \gg \mu^{-1} \tag{1.14}$$

which depends on the medium density ρ and the cross section of the parton–medium interaction σ as [19, 20]

$$\lambda = \frac{1}{\rho\sigma}. \tag{1.15}$$

Each scattering in the random walk corresponds to a transfer of transverse momentum q_T from the medium to the projectile parton with a typical average value given by [18, 19, 21, 22]

$$\left\langle q_\mathrm{T}^2 \right\rangle \approx \mu^2. \tag{1.16}$$

Properties of the medium are encoded in the transport coefficient $\hat{q}$, defined as the average transverse momentum squared transferred to the projectile per unit path length [3, 14, 16, 20–22]

$$\hat{q} \overset{\mathrm{def}}{=} \frac{\left\langle q_\mathrm{T}^2 \right\rangle}{\lambda} = \rho \int q_\mathrm{T}^2 \frac{\mathrm{d}\sigma}{\mathrm{d}^2 q_\mathrm{T}} \mathrm{d}^2 q_\mathrm{T}. \tag{1.17}$$

The characteristic energy ω_c of the radiated gluons depends on the path length L in medium and on the properties of the medium as [14, 18, 22]

$$\omega_\mathrm{c} = \frac{1}{2}\hat{q}L^2. \tag{1.18}$$

The average energy loss of the parton after traversing a distance L in the medium has the following dependence [18]

$$-\left\langle \Delta E \right\rangle = \frac{\alpha_\mathrm{s} C_\mathrm{R}}{8} \frac{\mu^2}{\lambda_\mathrm{g}} L^2 \ln\left(\frac{L}{\lambda_\mathrm{g}}\right), \tag{1.19}$$

where $\mu^2/\lambda_\mathrm{g} \propto \hat{q}$ and C_R is the QCD coupling (Casimir) factor [14].

This model however does not consider the evolution of the medium which plays an important role in the process of a heavy-ion collision. The effect of the medium expansion on the interaction with fast partons is considered in some

more recent models, e.g. YaJEM [23] or EPOS [24]. Advanced models also have to include contribution to the energy loss by collisions with constituents of the medium (collisional or elastic energy loss) which becomes dominant at low parton momentum [15].

Numerous models of parton energy loss in medium have been developed with improving or extending the BDMPS formalism or using different approaches. However, all currently used models are based on the same common assumptions [16]:

- Interactions of the energetic parton and the radiated gluon with the medium can be calculated via factorized pQCD approach.

- The parton energy E and the energy of the emitted gluon ω are much larger than the transverse momentum exchanged with the medium q_{T}.

- The energy of the emitted gluon is much larger than its transverse momentum, i.e. the gluon is emitted under a small angle with respect to the parton momentum.

- The mean free path of the parton–medium interaction λ is much larger than the Debye screening length μ^{-1}.

Further significant assumptions and approximations are mostly related to the virtuality and branching of the hard parton, the nature of the medium traversed by the parton and kinematical approximations for the interaction between medium and projectile parton. More important differences come from approximations concerning treatment of energy–momentum constraints and large-angle radiation [16].

Depending on the approach to modelling the medium and its interaction with the parton, the existing models can be categorized into four classes [15, 16]:

1. Path-integral approach to the opacity expansion (BDMPS-LCPI/BDMPS–Z, ASW): The medium is modelled as a set of static scattering centres and the expansion of the medium is approximated by its decreasing density. The projectile interaction with the medium is approximated via multiple soft scattering processes. Propagation of the parton and the gluon radiation are calculated using a path-integral that resums multiple scatterings. The model includes the interference between vacuum radiation and medium-induced radiation but, by construction, cannot account for elastic mechanisms of parton energy loss. This approach was pioneered by Baier, Dokshitzer, Mueller, Peigné and Schiff (BDMPS) and independently by Zakharov (Light-Cone-Path-Integral, LCPI) and is further developed by Armesto, Salgado and Wiedemann (ASW) [22].

2. Reaction Operator approach to the opacity expansion (DGLV): The medium is assumed to consist of (almost) static scattering centres, as in the BDMPS approach. This approach is based on an expansion of the calculation in terms of the number of scatterings using the path-integral formalism from BDMPS–Z. It starts with a radiation spectrum of a single hard gluon and expands it to account for gluons emitted from multiple scatterings.

It also includes the interference between vacuum radiation and medium-induced radiation. This approach was pioneered by Gyulassy, Lévai and Vitev (GLV) [25] and developed further by Djordjevic and Gyulassy [26].

3. Higher Twist (HT): In the higher-twist approximation, properties of the medium are described by matrix elements of gauge field operators. Multiple scatterings of a parton are described as power corrections to the leading-twist cross section. The interference between vacuum radiation and medium-induced radiation is included as well. The higher-twist approach was pioneered by Guo and Wang [27, 28].

4. Finite temperature field theory approach (AMY): The medium is characterized as being in a state of perfect thermal equilibrium described within Hard Thermal Loop improved finite-temperature perturbation theory. Properties of the medium are specified by its temperature and baryon chemical potential. The model does not consider branching of the projectile parton in vacuum and applies only at very high temperatures $T \gg T_{\mathrm{c}}$. This approach was developed by Arnold, Moore and Yaffe [29, 30].

1.3.3 Parton fragmentation

Parton fragmentation is the process of hadron production from an energetic parton produced in a hard scattering. The primary parton undergoes parton showering until virtuality of the created partons decreases to some low value. Then hadronization occurs and gives origin to a collimated spray of hadrons observed as a jet.

The process of converting a hard parton into an observable hadron is associated with a fragmentation function $D_{a \to h}(z, Q^2)$ (or $D_a^h(z, Q^2)$) which is a probability-like density distribution of the mean number of hadrons of type h produced by fragmentation of the parton a and carrying the fraction z of its momentum (or energy), such that the mean total number of hadrons produced by the parton a is obtained as

$$\langle N_a \rangle = \sum_h \int_0^1 D_{a \to h}(z, Q^2) \, \mathrm{d}z. \tag{1.20}$$

Factorization of non-perturbative fragmentation functions from perturbative processes introduces a dependence on the factorization scale Q^2.

One of the most widely used models for parton fragmentation is string hadronization, often associated with the Lund model [31, 32]. The model is based on the assumption that when a quark and an anti-quark with opposite colour charges move apart, the self-interacting colour field between them collapses into a narrow flux tube of constant energy density per unit length (string tension) $\kappa \approx 1\,\mathrm{GeV/fm}$ which corresponds to a linear confining potential between quarks. As the width of the string is negligible with respect to its length, the string is considered to be a one-dimensional, massless and relativistic object. If the (anti-)quarks at the end-points of the string are assumed massless, they oscillate outwards and inwards at the speed of light and exchange energy with the string. Hard gluons can be represented in the model by energy–momentum carrying kinks on the string. Additional intermediate quark–anti-quark pairs can be created from the field energy of the string when the string breaks up. The shower evolution

is terminated by formation of colourless string segments between neighbouring partons. In some schemes [33], the string fragments are considered as substrings called clusters which decay later into hadrons; other approaches [31, 32] consider the fragments to be actual hadrons [2].

1.3.4 Measurement of jet quenching in QGP

High-p_T partons produced in the initial stage of a nucleus–nucleus collision are expected to undergo multiple interactions inside the collision region prior to hadronization [14, Sec. 6.8]. Thanks to their early production in the initial hard-scattering processes, hard partons can be used in heavy-ion collisions as probes that interact with the later created QGP. The parton traversing the QGP loses energy mainly by medium-induced gluon radiation and partially also by collisional energy loss. This process is called "jet quenching" [14, Sec. 6.8]. In general, "jet quenching" refers to the modification of the evolution of an energetic parton induced by its interactions with colour charges in a medium [16].

If a fast parton traverses a significant distance through the dense matter formed in the collision, it may lose so much energy in the medium that it can no longer produce high-p_T hadrons. Partons with $p_T \lesssim 10\,\mathrm{GeV}/c$ are not able to reach the opposite edge of the medium volume and become part of the low-p_T background of soft particles. Jets from partons which lost too much energy cannot be identified as jets and become indistinguishable from the bulk of soft particles [3]. This makes jet finding a difficult task since a huge number of soft hadrons with $p_T < 2\,\mathrm{GeV}/c$ contributes to the background [3]. As a result, most of the observed jets come from a thin surface layer [3].

The interaction of a sufficiently energetic parton with constituents of the medium modifies the way the parton fragments and translates into a modification of properties of the subsequently produced jet. Modification of parton showers can result in the suppression of hadron spectra at high p_T and their enhancement at low p_T, the suppression of back-to-back azimuthal hadron correlations, the angular broadening of internal jet structure or di-jet acoplanarity [16].

Measurements of jet production in elementary collisions provide a reference for measurements in heavy-ion collisions and represent precise tests of pQCD verifying that the elementary processes are well understood.

Using knowledge of jet properties in the elementary collisions, one can determine the characteristics of the jet modification related to the presence of the QGP. That allows to determine properties of the QGP itself and compare the experimental results with predictions of various theoretical models. Measurements of jet quenching provide powerful tools for studying the properties of the hot and dense strongly interacting matter produced in heavy-ion collisions [16].

A standard tool for quantifying how the production of a probe object in heavy-ion collisions differs from its production in elementary collisions is the nuclear modification factor R_{AA}. This ratio is defined as the spectrum of the probe production in heavy-ion collisions normalized to a single binary nucleon–nucleon collision and divided by the reference spectrum measured in p–p collisions at the same centre-of-mass energy per nucleon pair [14, Sec. 6.8.3.2]:

$$R_{AA}(p_T, \eta, b) \stackrel{\text{def}}{=} \frac{1}{\langle N_{\text{coll}}(b) \rangle} \frac{\mathrm{d}^2 N_{AA}(p_T, \eta, b)/\mathrm{d}p_T\,\mathrm{d}\eta}{\mathrm{d}^2 N_{pp}(p_T, \eta)/\mathrm{d}p_T\,\mathrm{d}\eta}. \tag{1.21}$$

In a case where the medium created in heavy-ion collisions does not modify production of the probe, nuclei collisions are equivalent to a superposition of independent nucleon collisions and R_{AA} equals unity by construction. If R_{AA} is different from unity, it means that the production of the probe in heavy-ion collisions is affected by processes which are not present in the p–p collisions. The dependence of R_{AA} on the impact parameter b indicates that the modification of spectra is usually evaluated as a function of centrality classes. A similar observable for evaluating spectra modification is R_{CP} which is the ratio of normalized spectra in central and peripheral nucleus–nucleus collisions:

$$R_{\mathrm{CP}}\left(p_{\mathrm{T}}, \eta\right) \stackrel{\mathrm{def}}{=} \frac{\left[\left(\mathrm{d}^2 N_{\mathrm{AA}}\left(p_{\mathrm{T}}, \eta\right)/\mathrm{d}p_{\mathrm{T}}\,\mathrm{d}\eta\right)/\left\langle N_{\mathrm{coll}}\right\rangle\right]\big|_{\mathrm{central}}}{\left[\left(\mathrm{d}^2 N_{\mathrm{AA}}\left(p_{\mathrm{T}}, \eta\right)/\mathrm{d}p_{\mathrm{T}}\,\mathrm{d}\eta\right)/\left\langle N_{\mathrm{coll}}\right\rangle\right]\big|_{\mathrm{peripheral}}}. \qquad (1.22)$$

The first observation of jet quenching was achieved by experiments at RHIC. Namely, observation of a strong suppression of inclusive yields of high-p_{T} hadrons [34, 35], suppression of angular correlations of hadron pairs [36–39] and modification of jet production [40] provided convincing confirmation of modification of particle production in heavy-ion collisions by the medium. In Pb–Pb collisions at the LHC, jet quenching was experimentally observed first by the ATLAS experiment [41], followed soon after by the experiments ALICE [42] and CMS [43]. The impact of jet quenching is nicely illustrated in Fig. 1.4 which shows an event with a pair of jets measured by the ATLAS experiment, with indicated distribution of reconstructed energy. One jet is observed to have a narrow angular energy distribution whereas the energy of the corresponding recoil jet going in opposite direction is dispersed in azimuth over a wide range of angles. Several results of observation of jet quenching in spectra of hadrons measured in
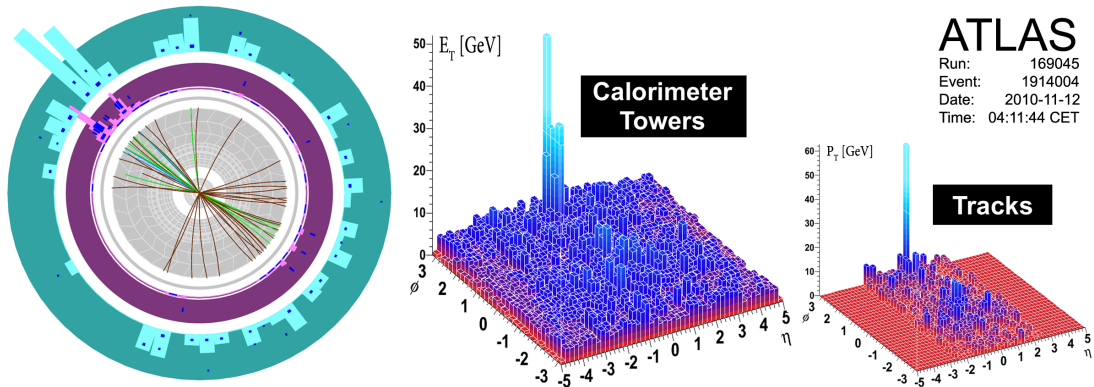

Figure 1.4: Event display of a highly asymmetric dijet event measured by ATLAS in a Pb–Pb collision at $\sqrt{s_{\mathrm{NN}}} = 2.76\,\mathrm{TeV}$. The recoil jet can be seen in the electromagnetic and hadronic calorimeters, dispersed widely over azimuth [41].

various experiments at the SPS, RHIC and the LHC are summarized in Fig. 1.5. The R_{AA} ratios of neutral pions and charged hadrons measured in central Pb–Pb and Au–Au collisions are compared with predictions of several models of parton energy loss. A comparison of measurements of spectra modification in Pb–Pb collisions expressed as the R_{CP} ratio acquired by the experiments at the LHC is shown for hadrons and reconstructed jets in Fig. 1.6. The results presented in both
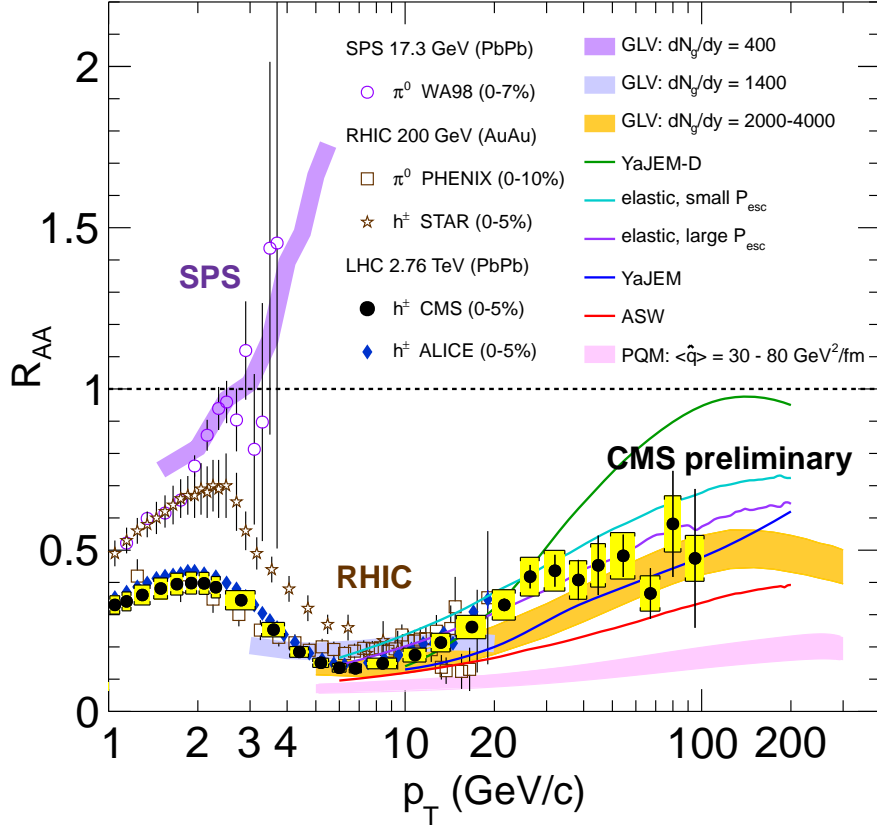
Figure 1.5: Measurements of the nuclear modification factor R_{AA} of neutral pions and charged hadrons in central heavy-ion collisions in experiments at the SPS, RHIC and the LHC [44].
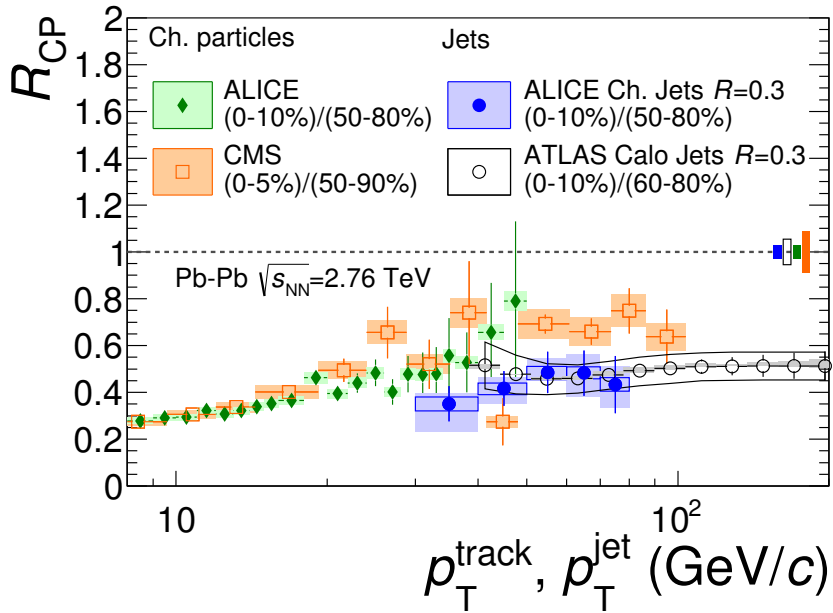

Figure 1.6: Comparison of R_{CP} of charged hadrons and jets measured in Pb–Pb collisions at $\sqrt{s_{NN}} = 2.76$ TeV by the experiments at the LHC [45].

figures show a clear suppression of yields of particles and jets in central heavy-ion collisions over a span of two orders of magnitude in transverse momentum.

1.3.5 Jet algorithms

A jet algorithm (or jet finder) is a selection method which is supposed to take a list of particle-like objects and group these into jets so that kinematic properties of the jets may be related to the corresponding properties of the energetic partons produced in the hard scattering process [46]. At the experimental level, the particle-like objects on the input of the algorithm are usually energy deposits in calorimeter towers and/or reconstructed momenta of detected hadrons. In perturbative QCD calculations, simulated partons are processed by the jet algorithm. The jet algorithm identifies sets of particles which are typically emitted close to each other in angle and marks them as belonging to the same jets. A rule called "recombination scheme" then determines the way momenta of particles in a jet are combined to get the momentum of the jet [46]. Angular size of the reconstructed jets is controlled by a resolution parameter R. The exact meaning of R depends on the algorithm.

The ideal jet algorithm should meet the following main criteria [46]:

1. Full specification: The jet selection algorithm, the jet kinematic variables and the corrections should be clearly and completely defined, including definitions of preclustering, merging and splitting algorithms, if necessary.

2. Theoretically good behaviour: The algorithm should be infrared and collinear safe with no ad hoc clustering parameters.

   - Infrared safety: Jet finding procedure should be insensitive to the presence of soft radiation between jets.

   - Collinear safety: Jet finding procedure should be insensitive to the splitting of jet transverse energy into multiple collinear particles.

   - Invariance under boosts: Jet finding procedure should be independent of boosts in the direction of collision axis.

3. Detector independence: The jet algorithm should not depend on the type, number, size or segmentation of detector cells.

4. Order independence: The algorithms should find the same jets at the parton, particle and detector levels.

Historically, the first jet algorithms were cone algorithms [47], based on clustering particles emitted within a cone of radius R in $\eta \times \phi$ space. Reconstruction of jets by these algorithms however encountered several technical and also theoretical difficulties and did not meet the requirements listed among the criteria above. As new and more convenient algorithms have been developed since, cone algorithms have been progressively replaced by sequential recombination algorithms which have simple definitions and are all infrared safe.

Algorithms belonging in the class of sequential recombination jet algorithms are defined by the following general scheme [48].

1. $\forall \, i, j$: calculate distance d_{ij} between particles i and j and distance $d_{i\mathrm{B}}$ between particle i and the beam (B):

$$d_{ij} = \min\left(k_{\mathrm{T},i}^{2p}, k_{\mathrm{T},j}^{2p}\right)\frac{\Delta_{ij}^2}{R^2}, \quad \Delta_{ij}^2 = (y_i - y_j)^2 + (\phi_i - \phi_j)^2, \quad (1.23)$$

$$d_{i\mathrm{B}} = k_{\mathrm{T},i}^{2p}, \quad (1.24)$$

where $k_{\mathrm{T},i}$, y_i, and ϕ_i are respectively the transverse momentum, rapidity and azimuth of particle i.

2. Find $d_{\min}$:

$$d_{\min} = \min\left(d_{ij}, d_{i\mathrm{B}}\right). \quad (1.25)$$

- If $\exists \, i, j : d_{\min} = d_{ij}$, merge particles i and j into a single particle and combine their momenta.

- If $\exists \, i : d_{\min} = d_{i\mathrm{B}}$, declare particle i to be a final jet and remove it from the list.

These steps are repeated until no particles are left.

This general scheme parametrizes the whole class of sequential recombination algorithms, where specific algorithms differ by value of the parameter p which sets the power of the transverse momentum taken in the distance calculation in Eq. (1.23). The special cases represented by the three most widely used algorithms from this class are:

$$p = \begin{cases} 1 & k_{\mathrm{t}}, \\ 0 & \text{Cambridge/Aachen}, \\ -1 & \text{anti-}k_{\mathrm{t}}. \end{cases} \quad (1.26)$$

The algorithm preferred by the LHC experiments for inclusive jet reconstruction is the anti-k_{t} algorithm. The characteristic property of the anti-k_{t} algorithm is that the distance d_{ij} between a hard and a soft particles is smaller than the distance between two soft particles separated by the same angle. Therefore soft particles are clustered with hard ones first and only afterwards are soft particles clustered among themselves. A hard particle surrounded by soft particles accumulates these within a circle of radius R, resulting in a perfectly conical jet. In case of two hard particles close to each other, corresponding jets are separated by a line of shape depending on transverse momenta of the hard particles. Shapes of the final jets are determined by the distribution of hard particles within the event and are not affected by soft particles. Hard jets are all circular with a radius R and only the softer jets have more complex shapes [48].

In case of the k_{t} algorithm [49], the clustering sequence starts with clustering soft particles which is more convenient for characterizing soft background in the events.

1.4 Hadronization mechanisms in QGP

Hadronization is the process of the formation of hadrons by colour confinement from quarks and gluons. Since the process is not fully understood in QCD, there

is no rigorous theoretical description of it, so hadronization must be modelled and parametrized using phenomenological models. According to the current level of understanding, hadronization is believed to be independent of processes with large momentum transfers and the process itself is expected to occur in the low-energy non-perturbative regime [2]. This justifies the approach of treating it separately from perturbative terms in QCD calculations using factorization theorems.

Experimental results provide a clear evidence for a difference between hadron production in heavy-ion collisions and in elementary collisions. That leads to considering scenarios with hadronization mechanisms modified in heavy-ion collisions by the presence of QGP or scenarios with some additional mechanisms of hadron production that are absent (or negligible) in elementary collisions and occur only (or predominantly) in the medium.

Only two hadronization mechanisms, relevant for the analysis presented in this thesis, are briefly introduced in this section.

1.4.1 Modified parton fragmentation

Although the final hadronization of the hard parton traversing the medium is always assumed to occur in the vacuum after the parton has escaped from the system, the fragmentation might be affected by the prior energy loss suffered by the parent parton [15, 16]. Medium-induced partonic energy loss through gluon radiation decreases the energy of the leading particle and produces extra particles from the fragmentation of the radiated gluons. Hence, one expects a decrease of the number of particles carrying a high fraction z of the jet energy and an increase of the number of particles with low z [14, Sec. 6.8]. This effect is illustrated in Fig. 1.7 which shows the expected modification of fragmentation functions for different particle species as obtained from calculations based on the MLLA formalism [50]. Since all models of parton energy loss in medium are based on the assumption of factorized QCD calculations, the entire effect of parton energy loss is concentrated on the calculation of the medium-modified parton fragmentation functions, which can be obtained by applying corrections on the vacuum fragmentation functions, typically by introducing modifications of splitting functions in the perturbative evolution equations [15], as for example in the higher-twist approach by Guo and Wang [27, 28]. Details of modifying fragmentation by taking into account parton interaction with the medium depend on the model but schematically correspond to the transition:

$$D^{\text{vacuum}}_{a \to h}(z, Q^2) \to D^{\text{medium}}_{a \to h}(z', Q^2, \hat{q}), \quad z' < z. \tag{1.27}$$

1.4.2 Parton recombination and coalescence

Another mechanism that might exist and be relevant in production of hadrons at intermediate p_{T} in heavy-ion collisions is parton recombination or coalescence. Thermal quarks appearing close to each other in a densely populated phase space cluster among themselves or with quarks produced in minijets and form mesons and baryons. Distributions of quarks and anti-quarks in phase space are expressed by phenomenological Wigner functions $w(r, p)$ and $\overline{w}(r, p)$ and the recombination is assumed to take place on a hyper-surface $\Sigma_{\text{f}} \ni r$ associated with expanding
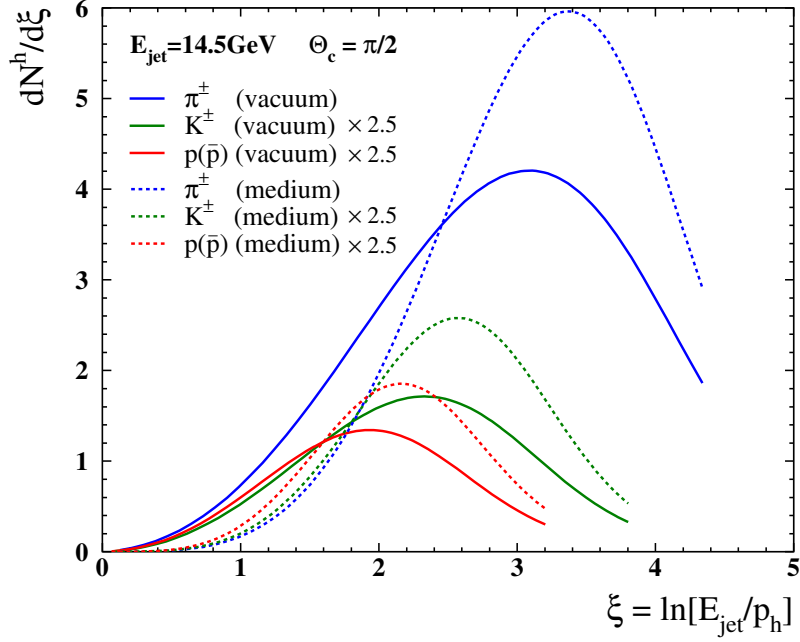
Figure 1.7: Comparison of the fragmentation in vacuum and the expected modification of the fragmentation functions for pions, kaons and protons in jets of energy 14.5 GeV obtained from calculations using the MLLA formalism [50].

system of quarks and anti-quarks. In a simplified version of the model, the production rates of the mesons (M) and baryons (B) are given as:

$$E\frac{\mathrm{d}^3 N_{\mathrm{M}}}{\mathrm{d}^3 p} \propto \int_{\Sigma_{\mathrm{f}}} p^\mu \, \mathrm{d}\Sigma_\mu \int_0^1 \mathrm{d}x \, w(r, xp_{\mathrm{T}})\overline{w}(r, (1-x)p_{\mathrm{T}}) \left|\phi_{\mathrm{M}}(x)\right|^2, \qquad (1.28)$$

$$E\frac{\mathrm{d}^3 N_{\mathrm{B}}}{\mathrm{d}^3 p} \propto \int_{\Sigma_{\mathrm{f}}} p^\mu \, \mathrm{d}\Sigma_\mu \int_0^1 \mathrm{d}x \int_0^{1-x} \mathrm{d}x'$$
$$\times \, w(r, xp_{\mathrm{T}})w(r, x'p_{\mathrm{T}})w(r, (1-x-x')p_{\mathrm{T}}) \left|\phi_{\mathrm{B}}(x, x')\right|^2, \qquad (1.29)$$

respectively, where x and x' are momentum fractions carried by the constituent quarks, ϕ_M and ϕ_B are the light-cone wave functions of the respective hadrons [7, 51].

The important feature of the parton recombination mechanism is that, in contrast to the parton fragmentation, recombination leads to production of hadrons with momenta larger than momenta of their parent partons, whereas parton fragmentation splits the momentum of the parent parton into smaller momenta of produced hadrons. Given the steeply falling p_{T} distribution of quarks, this opens a possibility for a p_{T} range where the parton recombination might be the dominant hadronization mechanism. In such a p_{T} region, production of a baryon at a given p_{T} from recombination of three soft quarks would be more probable than production of a meson at the same p_{T} from a pair of less soft quark and anti-quark. That would lead to an enhancement of the yield ratio of baryons to mesons [7]. The recombination scenario should also manifest itself in the amplitude of the elliptic azimuthal anisotropy which would scale with the number of constituent quarks [52, 53].

There exist several hadronization models involving parton recombination.

Fries et al. [51, 54] consider recombination of thermal quarks only, whereas Greco et al. [55–57] and Hwa with Yang [58–60] take into account clustering of thermal partons from QGP with shower partons from minijets created by hard partons.

1.5 Enhancement of the baryon-to-meson ratio

The ratio of baryon spectra to meson spectra measured for inclusive production of light-flavour particles at intermediate transverse momenta ($2\,\mathrm{GeV}/c \lesssim p_\mathrm{T} \lesssim 6\,\mathrm{GeV}/c$) in heavy-ion collisions is enhanced with respect to the ratio measured in p–p collisions. The effect was observed in the inclusive p/π and $\Lambda/\mathrm{K}_\mathrm{S}^0$ ratios first at RHIC [61–63] and was later measured also at the LHC by the ALICE experiment [64]. The ratio of the inclusive p_T spectrum of Λ baryons to the spectrum of K_S^0 mesons measured in Pb–Pb collisions by the ALICE experiment [64] is displayed in Fig. 1.8 for different centrality ranges and compared with the ratio in p–p collisions. The ratio in Pb–Pb collisions increases strongly with centrality
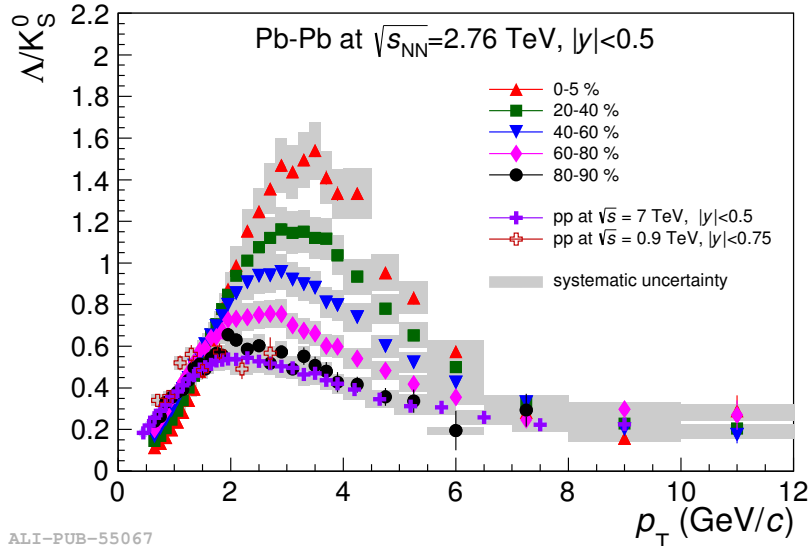
Figure 1.8: Inclusive $\Lambda/\mathrm{K}_\mathrm{S}^0$ ratio in Pb–Pb collisions at $\sqrt{s_\mathrm{NN}} = 2.76\,\mathrm{TeV}$ measured by ALICE as a function of centrality compared with the ratio in p–p collisions [64].

and, for the most central collisions, reaches a maximum three times higher than the ratio obtained for p–p collisions. A smaller but still significant enhancement is manifest in proton–lead (p–Pb) collisions as well [65]. The ratios measured in Pb–Pb and p–Pb collisions are displayed together in Fig. 1.9.

This phenomenon is not clearly understood yet and various mechanisms have been proposed to explain it. One of considered explanations is modification of jet fragmentation in medium. Some other proposals attribute the enhancement to various scenarios based on hadronization by parton recombination [58, 59, 66–68].

Fig. 1.10 shows the $\Lambda/\mathrm{K}_\mathrm{S}^0$ ratios measured at RHIC and the LHC compared with selected models. A hydrodynamical model describes the data well only for p_T up to about $2\,\mathrm{GeV}/c$, the recombination model reproduces the shape of the ratio but overestimates the values by about $15\,\%$. The best description of the
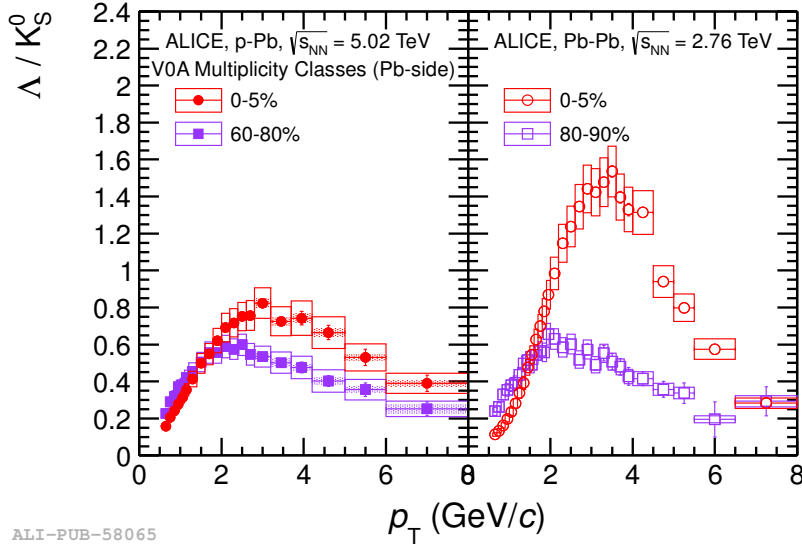
ALI-PUB-58065

Figure 1.9: Comparison of inclusive Λ/K_S^0 ratios measured by ALICE in p–Pb and Pb–Pb collisions [65].
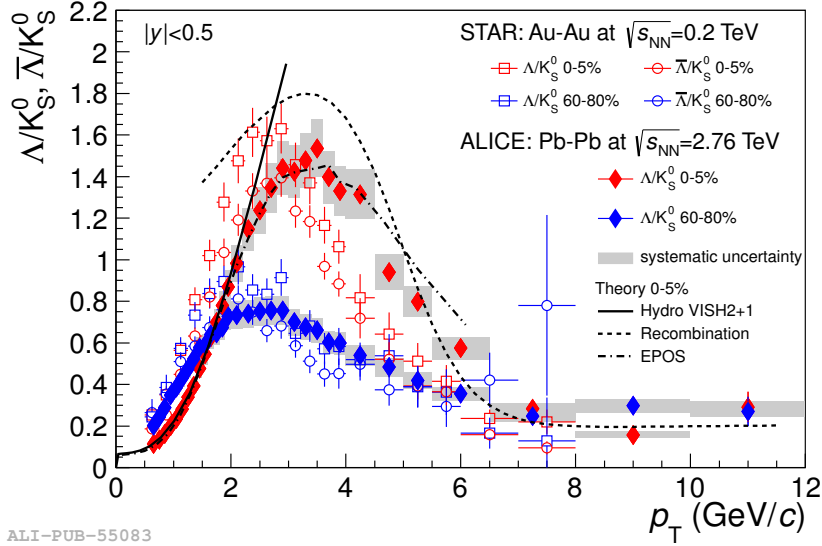
ALI-PUB-55083

Figure 1.10: Inclusive Λ/K_S^0 ratio in Pb–Pb collisions compared with Λ/K_S^0 and $\overline{\Lambda}/K_S^0$ ratios measured by STAR in Au–Au collisions [62, 63]. The solid, dashed and dot-dashed lines show the ratios from a hydrodynamical model, a recombination model and the EPOS model, respectively [64].

enhancement is achieved by the EPOS [68] model which takes into account the interaction between jets and the hydrodynamically expanding medium [64].

The origin of the enhancement of the baryon-to-meson ratio might be better unravelled by measuring production of hadrons from individual sources that contribute to the total bulk of particles. Since jets are assumed to be produced exclusively by fragmentation of partons created in hard scattering, measurements of spectra of identified particles produced in jets represent an important tool for understanding the interplay of various hadronization mechanisms that contribute to the particle production in the hot and dense medium created in ultra-relativistic heavy-ion collisions.

Recent results from analyses of jet-like correlations of particles with high-p_{T} trigger particles performed by the ALICE experiment at the LHC [69] and the STAR experiment at RHIC [70] indicate that the $\Lambda/\mathrm{K}_{\mathrm{S}}^{0}$ ratio of hadrons produced in hard processes is much smaller than the ratio measured for inclusive particles. Recent results from the analysis of particles in reconstructed charged jets in p–Pb collisions by ALICE show the same behaviour [71].

The goal of the presented analysis is to study the origin of the enhancement of the $\Lambda/\mathrm{K}_{\mathrm{S}}^{0}$ ratio by selecting hadrons produced in association with jets, measuring their spectra and determining the corresponding ratio. The results of this analysis aim to disentangle contributions of processes in bulk and potential contribution of modified jet fragmentation in medium.

2. ALICE

A Large Ion Collider Experiment (ALICE) is one of the main experiments at the Large Hadron Collider (LHC) at CERN near Geneva. The LHC is a particle accelerator placed in a circular underground tunnel with circumference of 27 km. The accelerator has been designed to accelerate protons up to an energy of 7 TeV and also lead nuclei up to an energy of 2.76 TeV per nucleon. Accelerated particles orbit in opposite directions in two separate beam pipes, enclosed in shared superconducting magnets, and collide at four crossing points where the detectors of the main experiments measure particles produced by the collisions.

ALICE is a general-purpose heavy-ion experiment designed to study strongly interacting matter and the quark–gluon plasma created in heavy-ion collisions [72]. The collaboration counts about 1852 members from 174 institutes in 41 countries [73].

2.1 Detectors

The detectors of ALICE provide tracking of charged particles in a wide range of transverse momentum (p_T) from 100 MeV/c to 100 GeV/c and allow to identify particles with momentum up to tens of GeV/c. Detection of short-lived particles (e.g. hyperons and D mesons) is achieved by reconstruction of secondary vertices from decays. The detectors were optimized for large charged-particle multiplicities of about $dN/d\eta = 4000$ at mid-rapidity and tested with simulations for up to twice that value [72]. Mid-rapidity detectors are placed in a magnetic field of 0.5 T provided by a solenoid magnet previously used in the L3 experiment. Tracking of charged particles in the central barrel is performed by the Inner Tracking System (ITS) and the Time-Projection Chamber (TPC) together with the Transition Radiation Detector (TRD) which improves the momentum resolution for particles with high p_T. The large dynamic range of momentum measurement is achieved by using detectors with very low material thickness and covering a large range of radius. The layout of ALICE detectors is displayed in Fig. 2.1.

The ALICE coordinate system is a right-handed orthogonal Cartesian system defined as follows. The origin is at the LHC Interaction Point 2 (IP). The x-axis is perpendicular to the mean beam direction, aligned with the local horizontal and pointing to the accelerator centre. The y axis is perpendicular to the x-axis and to the mean beam direction, pointing upward. The z-axis is parallel to the mean beam direction and is pointing in the direction opposite to the muon spectrometer (i.e. anticlockwise with respect to the LHC) [72, 75]. Given the symmetry of the ALICE apparatus, it is often convenient to use cylindrical coordinates where the z-axis coincides with the z-axis of the Cartesian system, ϕ is the azimuth angle and radius r is the distance from the z-axis.

2.1.1 Inner Tracking System (ITS)

The Inner Tracking System consists of 6 cylindrical layers of silicon detectors providing measurement of trajectories of charged particles emitted from the interaction diamond in the pseudorapidity range of $|\eta| < 0.9$. The main functions
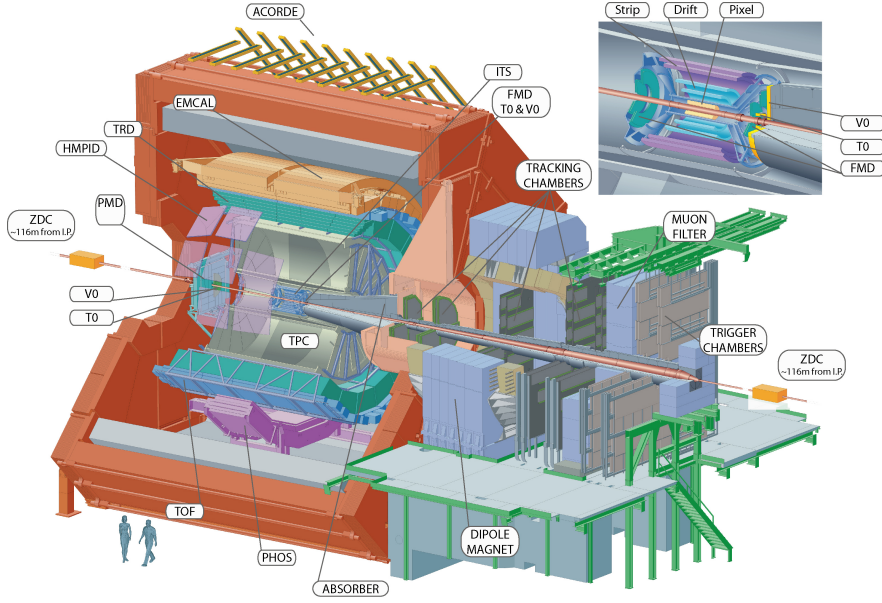
Figure 2.1: Layout of ALICE detectors [74].

of the ITS are to determine the position of the primary vertex with a resolution better than $100\,\mu$m, to reconstruct secondary vertices resulting from decays of hyperons and D mesons, to perform tracking and identification of particles with momentum lesser than $200\,$MeV$/c$, to improve the momentum resolution of particles reconstructed in the TPC and to reconstruct tracks passing through dead regions of the TPC. [76]. The schematic layout of the ITS layers is displayed in Fig. 2.2.
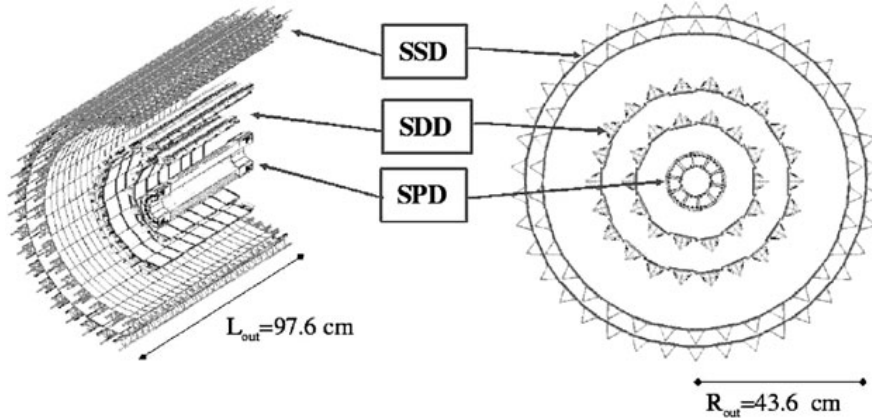
Figure 2.2: Layout of the ITS [77].

The two innermost layers of the ITS, located at radii $3.9\,$cm and $7.6\,$cm from the z axis, consist of the Silicon Pixel Detector (SPD) which is designed for registering as many as 50 charged particles per cm^2. The SPD plays a crucial role in the measurement of the position of the primary vertex and of the impact parameter of secondary tracks originating from weak and heavy-flavour decays. The pixels are reverse-biased silicon detector diodes arranged in a sensor matrix on each of 240 modules. Both layers of the SPD in total consist of 9.8×10^6 cells [76]. The spatial precision of the SPD reaches $12\,\mu$m in $r\phi$ and $100\,\mu$m in z.

Each pixel chip generates a digital pulse whenever a particle produces a signal above threshold in a pixel cell. The pulse is used to generate a prompt trigger signal with latency of about 800 ns [72].

The two middle layers of the ITS, located at radii 15.0 cm and 23.9 cm, are equipped with the Silicon Drift Detector (SDD). Each unit of the SDD detector has a sensitive area that consists of drift regions separated by a central cathode strip with a high-voltage applied to it. Cathode strips placed on both surfaces of each drift region create a fully depleted volume and generate a drift field with a typical value of drift speed of $8\,\mu m\,ns^{-1}$. The SDD consists of 260 modules and provides particle identification by measuring dE/dx in the non-relativistic region and an average spatial precision of $35\,\mu m$ in $r\phi$ and $25\,\mu m$ in z [72].

The two outer layers of the ITS, located at radii 38.0 cm and 43.0 cm, are equipped with the Silicon Strip Detector (SSD). The SSD layers are important for matching of tracks between the ITS and the TPC. Modules of the SSD are made of double-sided silicon micro-strip detectors and also contribute to the particle identification using dE/dx in the non-relativistic region. The SSD consists of 1698 modules and its spatial precision reaches $20\,\mu m$ in $r\phi$ and $830\,\mu m$ in z [72].

2.1.2 Time-Projection Chamber (TPC)

The Time-Projection Chamber is the main tracking device of the central barrel. The schematic layout of the TPC is displayed in Fig. 2.3. Its function is to measure
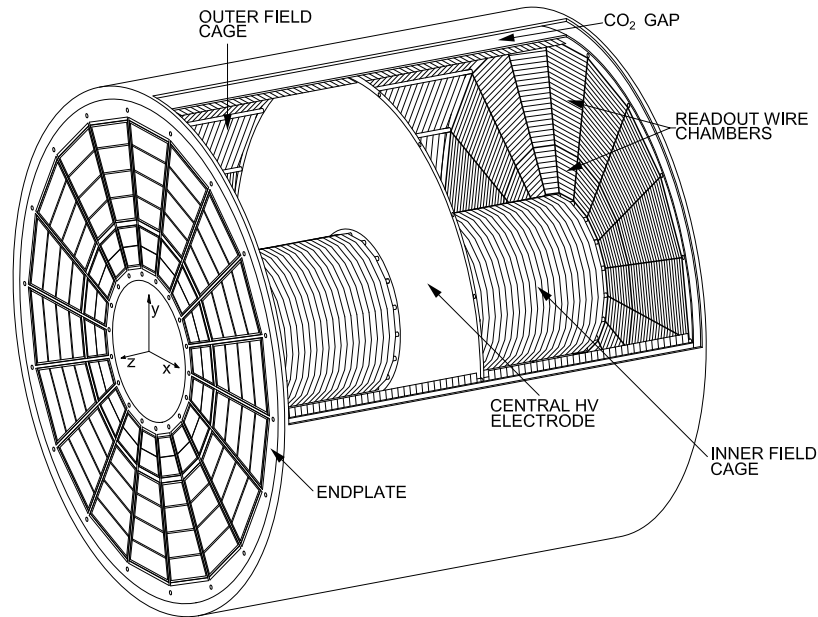
Figure 2.3: Layout of the TPC [78].

momentum of charged particles, to identify particles and to help determine the position of the primary vertex. It can measure tracks of particles in full azimuth range within the acceptance region $|\eta| < 0.9$ for particles that cross the full radial range of the TPC. Shorter tracks of particles leaving the TPC through the vertical end plates can be measured in a region $|\eta| < 1.5$ with a reduced momentum resolution. The TPC provides momentum measurement in the large

range of $100\,\mathrm{MeV}/c \leq p_\mathrm{T} \leq 100\,\mathrm{GeV}/c$ with a good momentum resolution. The active volume of the chamber covers radii from $85\,\mathrm{cm}$ to $250\,\mathrm{cm}$ and a length of $500\,\mathrm{cm}$ along the beam direction. The detector is made of a cylindrical field cage divided by a vertical central electrode and with multi-wire proportional chambers in 18 trapezoidal sectors at each end plate. During the period of the Run 1, the cage was filled with a mixture of neon, carbon dioxide and nitrogen [72]. The TPC provides a position resolution of about $1\,\mathrm{mm}$ both in $r\phi$ and z [77]. The $\mathrm{d}E/\mathrm{d}x$ measurement can be used for identifying individual particles at low momentum and for statistical separation of hadron species in the relativistic region up to a few tens of GeV/c with resolution of $6.9\,\%$ for events with the highest particle multiplicities [77]. The distribution of the $\mathrm{d}E/\mathrm{d}x$ signal measured by the TPC in Pb–Pb collisions is shown in Fig. 2.4 as a function of particle momentum [75]. The
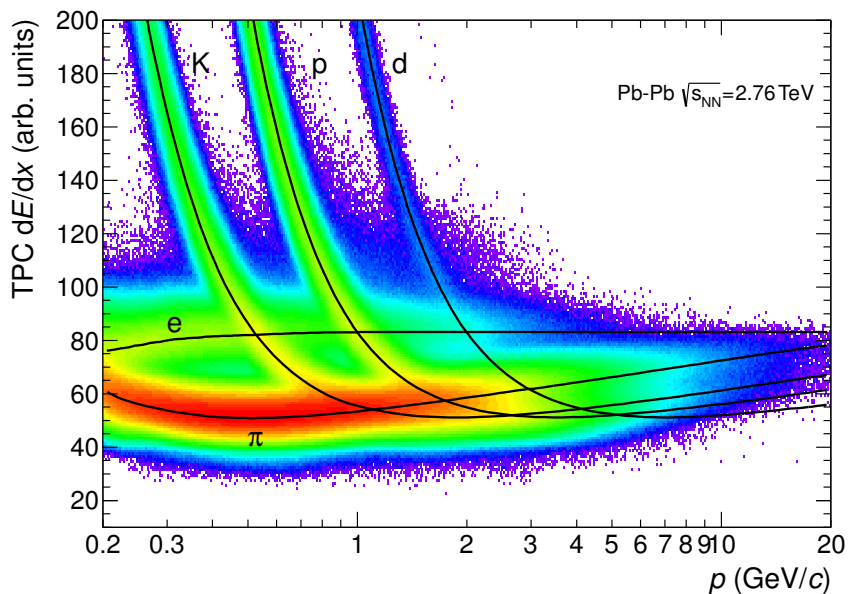
Figure 2.4: Distribution of energy loss ($\mathrm{d}E/\mathrm{d}x$) in the TPC as a function of particle momentum in Pb–Pb collisions. The lines show the parametrizations of the expected mean energy loss for different particle species [75].

momentum resolution of tracks with momentum between $100\,\mathrm{MeV}/c$ and $1\,\mathrm{GeV}/c$ reconstructed in the TPC is between $1\,\%$ and $2\,\%$. By combining measurements in the TPC with other detectors (ITS and TRD) tracks with p_T of $100\,\mathrm{GeV}/c$ can be measured with momentum resolution better than $10\,\%$ [77, Sec. 3.5.1.1] [78]. The resolution of measuring transverse momenta with the TPC in combination with the ITS in Pb–Pb collisions is shown in Fig. 2.5.

2.1.3 Transition Radiation Detector (TRD)

The Transition Radiation Detector was designed mainly to identify electrons with transverse momentum $p_\mathrm{T} > 1\,\mathrm{GeV}/c$ and to generate a fast trigger for charged particles with high momentum. It also contributes to the tracking of particles in the central barrel by improving the momentum resolution. It occupies a radial range of 290–$368\,\mathrm{cm}$ and covers the pseudorapidity range $|\eta| < 0.84$ in full azimuth acceptance. Its 540 modules are arranged in 18 super-modules in azimuth to
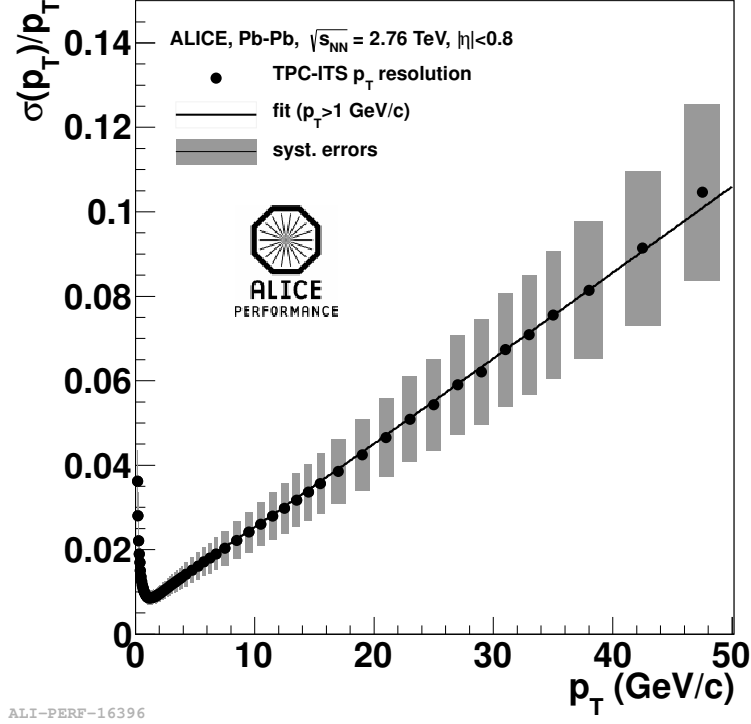
Figure 2.5: Transverse-momentum resolution of the TPC in combination with the ITS in Pb–Pb collisions [79].

match the segmentation of the TPC, 6 layers in radius and 5 stacks along z. Each module consists of a radiator and a multi-wire proportional chamber filled with a gas mixture of xenon and carbon dioxide. The space-point resolution of the TRD for tracks with $p_T = 1\,\text{GeV}/c$ is 400–600 μm in $r\phi$ and 2 mm in z [72].

2.1.4 Time-Of-Flight detector (TOF)

The Time-Of-Flight detector provides identification of charged particles in the intermediate momentum range in the pseudorapidity region $|\eta| < 0.9$ and full azimuth range. The identification reaches the best performance for pions and kaons with momentum below $2.5\,\text{GeV}/c$ and for protons with momentum up to $4\,\text{GeV}/c$. The distribution of velocity (β) measured by the TOF detector in Pb–Pb collisions is shown in Fig. 2.6 as a function of particle momentum in the TPC [75]. The detector occupies a radial range 370–399 cm and its segmentation in ϕ and along z matches that of the TRD. The detector uses 1638 strips based on the technology of the Multi-gap Resistive-Plate Chamber (MRPC) and subdivided into pads. The TOF detector provides time resolution better than 40 ps [72].

2.1.5 V0 detector

The V0 detector consists of two arrays of scintillator counters (V0A and V0C) placed on either side of the Interaction Point (IP) and covering pseudorapidity regions $2.8 < \eta < 5.1$ and $-3.7 < \eta < -1.7$. It provides a minimum bias trigger, a centrality trigger and separates beam–beam interactions from background events. Furthermore, it is also used to measure beam luminosity, azimuthal dis-
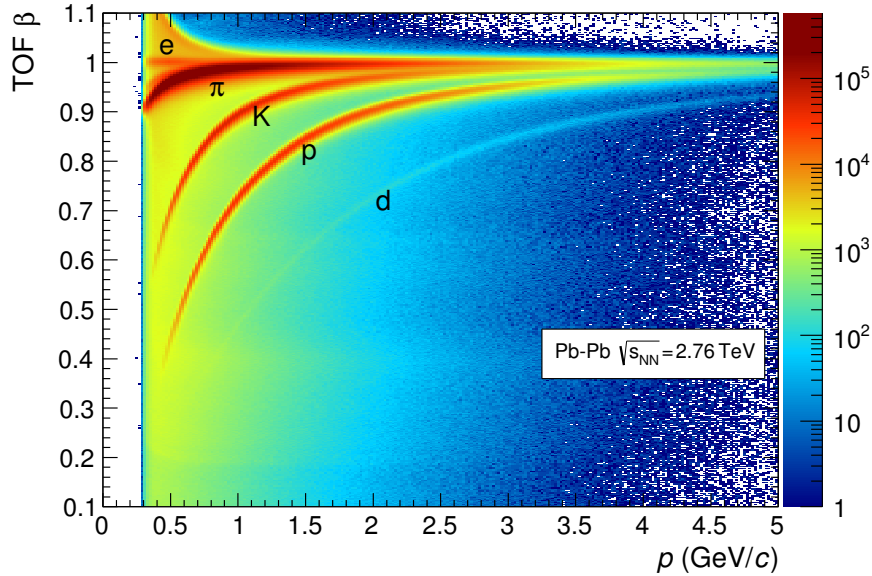
Figure 2.6: Distribution of velocity (β) measured by the TOF detector as a function of particle momentum in Pb–Pb collisions [75].

tributions of charged particles and to estimate centrality of Pb–Pb collisions based on the multiplicity of registered charged particles. Each array consists of 32 plastic scintillators arranged in 4 rings where each ring is divided in eight sections in azimuth [80].

2.1.6 ElectroMagnetic Calorimeter (EMCal)

The ElectroMagnetic Calorimeter is a layered lead-scintillator sampling calorimeter that covers $|\eta| \leq 0.7$ and $\Delta\phi = 107°$ at a radius of about $4.5\,\mathrm{m}$. It provides a fast trigger for hard jets, photons and electrons. The EMCal also enables full jet reconstruction by measuring the component of jet energy carried by neutral jet constituents. The detector is segmented into $12\,288$ towers arranged in modules and enables measurement of deposited energy with resolution better than $4\,\%$ for particles with momentum larger than $10\,\mathrm{GeV}/c$. The position resolution is of the order of millimetres [72, 81].

Another electromagnetic calorimeter called DCal has been recently installed in a position opposite to the EMCal in azimuth in order to extend the jet quenching measurements by providing a larger acceptance for back-to-back correlation measurements of jets, hadrons and photons. It uses the same technology as the EMCal [82].

2.1.7 Other detectors

The High-Momentum Particle Identification Detector (HMPID) enables identification of charged hadrons above $1\,\mathrm{GeV}/c$ up to $3\,\mathrm{GeV}/c$ for the separation of pions and kaons and up to $5\,\mathrm{GeV}/c$ for the separation of kaons and protons. It is based on proximity-focusing Ring Imaging Cherenkov (RICH) counters [72].

The PHOton Spectrometer (PHOS) is an electromagnetic spectrometer that identifies and measures low-momentum direct photons and neutral pions [72].

The ALICE COsmic Ray DEtector (ACORDE) is an array of plastic scintillator counters that contributes to the detection of energetic muons from cosmic rays [72].

The forward muon spectrometer enables measurement of spectra of vector-meson resonances by detecting muons in the pseudorapidity region $-4 < \eta < -2.5$ using a high-granularity tracking system of 10 detection planes [72].

The Zero-Degree Calorimeter (ZDC) is a set of hadronic calorimeters located at 116 m on either side of the IP. It measures the energy of non-interacting (spectator) nucleons and thus provides a centrality estimator. Signals from the ZDC are also used for triggering and for estimating the reaction plane of heavy-ion collisions. In addition, two small electromagnetic calorimeters (ZEM) are placed at about 7 m from the IP, on both sides of the LHC beam pipe. The ZEM calorimeters help to distinguish central events with low number of spectator nucleons from very peripheral events and also help to recognize events with background from electromagnetic processes [72].

The Photon Multiplicity Detector (PMD) is a preshower detector that measures the multiplicity and spatial distribution of photons on an event-by-event basis in the forward pseudorapidity region $2.3 \leq \eta \leq 3.7$ [72].

The Forward Multiplicity Detector (FMD) measures multiplicity of charged particles in the pseudorapidity range $-3.4 < \eta < -1.7$ and $1.7 < \eta < 5.0$ [72].

The T0 detector provides timing signals for the TOF detector and the TRD, it allows to measure the position of the primary vertex and provides several trigger signals. It consists of two arrays of Cherenkov counters covering the regions $-3.28 < \eta < -2.97$ and $4.61 < \eta < 4.92$ [72].

2.2 Primary-vertex reconstruction

The reconstruction of the primary vertex is performed using hit points reconstructed in the two layers of the SPD. Reconstructed points in the two layers that are close in ϕ and z are paired and used in a linear extrapolation to estimate the position of the primary vertex along the beam axis and in the transverse plane separately. The estimate of the vertex position along the beam axis is then corrected using the result obtained for the transverse plane. This estimate is used as a constraint in the first pass of the track reconstruction. The tracks reconstructed in the TPC and the ITS are then used for recalculating the position of the primary vertex which improves the precision of the measurement [72, Sec. 8.1.1]. The resulting resolution of the vertex position depends on the track multiplicity and is typically better than 10 μm in the z-coordinate and about 35 μm in the transverse plane for heavy-ion collisions [14, Sec. 5.1.1.3] and about 110 μm in the z-coordinate and 70 μm in the transverse coordinate for proton collisions [72, Sec. 8.1.1].

2.3 Track reconstruction in the central barrel

When a charged particle passes through a tracking detector it leaves a signal in the sensitive regions which allows to determine the position of the points in space where the particle crossed the detector. Reconstruction algorithms are designed

to recognize which space points belong to the same track and to reconstruct the momentum of the corresponding particle.

Tracking in the central barrel of ALICE starts with setting initial seed values for the track parameters using space points in the outermost pad rows of the TPC and a rough constraint on the position of the primary vertex. The tracking proceeds inwards by propagating tracks and combining compatible space points in the TPC using Kalman filtering, which is a method that allows to consider effects such as energy loss and multiple scattering in the material of detectors or to take into account dead zones between detectors when extrapolating tracks. The seeding and track propagating within the TPC is done once more without considering the primary vertex position in order to reconstruct tracks of secondary particles, that were not produced in the vicinity of the primary vertex. The tracks are then propagated to the outer layer of the ITS, starting with the tracks having the highest momentum. The propagation is done first with a strict primary-vertex constraint and then without it in order to consider candidates for secondary tracks reconstructed in the TPC. When propagating TPC tracks into the ITS layers, the ITS tracker attempts to prolong the TPC tracks as close as possible to the primary vertex. All space points compatible with the extrapolation of a given TPC track are considered and the resulting track candidates are compared at the end using their sums of the χ^2. Then, a special ITS stand-alone tracking procedure is applied in order to recover more tracks from the rest of the ITS clusters belonging to low-p_T particles with p_T down to about $80\,\mathrm{MeV}/c$ that cannot be efficiently reconstructed inside the TPC or to recover tracks that went through dead regions of the TPC. After this stage, Kalman filtering is applied for the second time but outwards from the point of closest approach to the collision point, through the ITS, and back to the outer wall of the TPC. Points with large deviation from the fit are removed during this pass. More space points are assigned to the tracks as the filtering proceeds into more distant detectors such as TRD, TOF, EMCal, HMPID and PHOS. Finally, Kalman filtering is applied once more for refitting all tracks from the outside inwards, starting from the outer radius of the TPC, in order to calculate track parameters at the point of the closest approach to the primary vertex [77, Sec. 4.1.3.1][72, Sec. 8.1.2][14, Sec. 5.1.2][75, Sec. 6.2].

2.4   Secondary-vertex reconstruction

The reconstruction of secondary vertices from photon conversions and decays of neutral strange particles (V^0s), namely decay channels $\mathrm{K}^0_\mathrm{S} \to \pi^+ + \pi^-$ and $\Lambda \to \mathrm{p} + \pi^-$, is performed using potential secondary tracks that are selected based on a large enough impact parameter with respect to the primary vertex ($> 0.5\,\mathrm{mm}$ in p–p and $> 1\,\mathrm{mm}$ in Pb–Pb collisions) [75, Sec. 6.4]. The principle of reconstruction of V^0 candidates is illustrated in Fig. 2.7. The distance of closest approach (DCA) of two tracks is calculated for each pair of the selected tracks with opposite charges. If this distance between both tracks is smaller than a defined value and the point of their closest approach lies closer to the primary vertex than the innermost measured points on both tracks, the pair is stored as a candidate for a V^0 particle with the position of the vertex lying on the line corresponding to the DCA and with a momentum calculated as the sum of momenta of the daughter tracks. In order to accept only candidates with momenta pointing from

the primary vertex, a cut is applied on the cosine of the pointing angle (CPA) between the V^0 momentum and the line connecting the V^0 vertex and the primary vertex [14, Sec. 5.1.7] [72, Sec. 8.1.3] [75, Sec. 6.4].
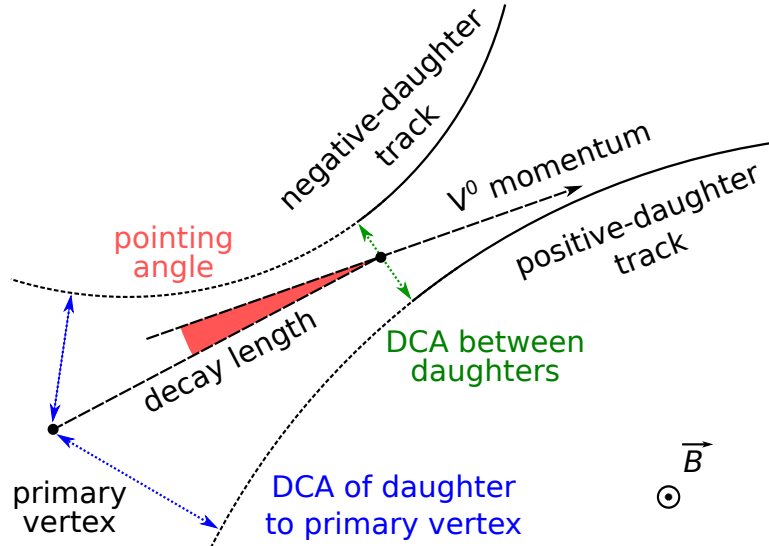

Figure 2.7: Principle of topological reconstruction of a V^0 decay.

Cascades $\Xi^- \to \Lambda + \pi^-$, $\Omega^- \to \Lambda + K^-$ (and their anti-particles) are reconstructed using Λ (and $\overline{\Lambda}$) candidates with large impact parameter with respect to the primary vertex and satisfying a loose cut on the CPA. Selected Λ candidates with acceptable invariant mass are combined with all possible secondary tracks (bachelor candidates) that have a large enough impact parameter with respect to the primary vertex in order to minimize contamination from primary particles. A pair of a V^0 candidate with a bachelor candidate is accepted as a candidate for a cascade particle if the DCA between the track of the bachelor track and the assumed trajectory of the V^0 candidate is small enough. Similarly to the case of V^0 candidates, only cascade candidates with momentum pointing from the primary vertex are accepted [14, Sec. 5.1.7].

Another procedure of searching for secondary vertices is used for the reconstruction of muonic decays of charged pions and kaons ($\pi^+ \to \mu^+ + \nu_\mu$, $K^+ \to \mu^+ + \nu_\mu$). Candidates for such decays are identified by recognizing their kink topology. Primary tracks that stop inside the volume of the TPC are combined with a secondary track of the same sign that is closely matched in space to the primary track. Momentum of the neutrino candidate is determined as the difference between momenta of the two charged particles. [72, Sec. 8.1.3] [75, Sec. 7.6].

2.5 Centrality determination

Collisions of nuclei can be characterized by centrality, which is a quantity related to the impact parameter of the collision that cannot be measured directly.

A Glauber model is a model describing geometry of a collision of nuclei and it is used for finding a correspondence between the impact parameter and centrality. An assumption on the relative contribution of sources producing particles is made

and the number of sources is considered to be determined by the number of participating nucleons and the number of binary nucleon–nucleon collisions. The number of produced particles is described for each source by a negative binomial distribution. Nuclear density of a lead nucleus is modelled by a Woods–Saxon distribution for a spherical nucleus with a radius of 6.62 fm and a skin depth of 0.546 fm.

The amplitude of the signals from the V0 scintillators is proportional to the multiplicity of charged particles produced in the collision. Parameters of the model are obtained from a fit to the distribution of measured amplitude in the V0 detector (see Fig. 2.8).
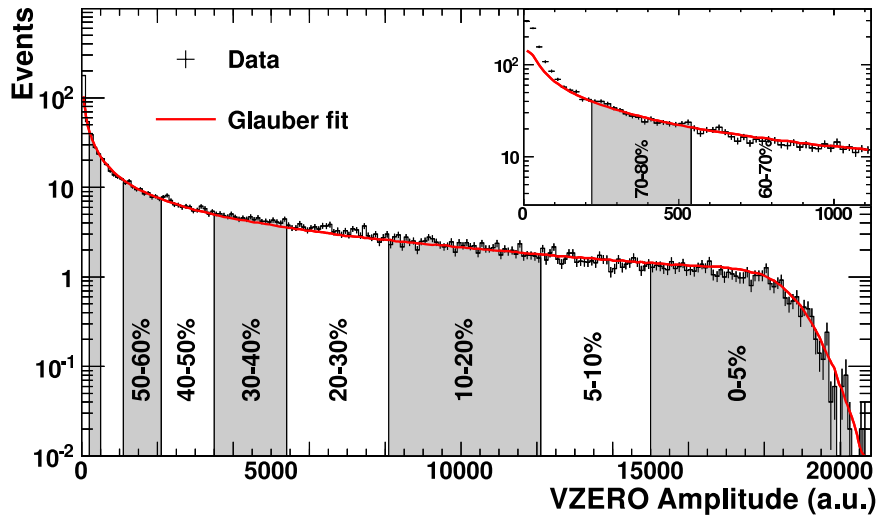
Figure 2.8: Centrality determination from the V0 amplitude. The solid curve corresponds to the fit of the distribution with a parametrization based on a Glauber model [83].

Centrality is expressed as percentage of the total hadronic cross section σ. The centrality percentile c of a nucleus–nucleus collision with impact parameter b is defined as [11] [75, Sec. 5.1]:

$$c(b) = \frac{\int_0^b \frac{\mathrm{d}\sigma}{\mathrm{d}b'} \mathrm{d}b'}{\int_0^\infty \frac{\mathrm{d}\sigma}{\mathrm{d}b''} \mathrm{d}b''}. \tag{2.1}$$

Experimentally, the centrality value for an event with a given measured amplitude V is obtained as the ratio of the integral of the distribution over the range of larger amplitudes to the total integral of the distribution [11] [83] [75, Sec. 5.1]:

$$c(V) = \frac{\int_V^\infty \frac{\mathrm{d}N}{\mathrm{d}V'} \mathrm{d}V'}{\int_0^\infty \frac{\mathrm{d}N}{\mathrm{d}V''} \mathrm{d}V''}. \tag{2.2}$$

In case of peripheral collisions, it is needed to reject events produced by electromagnetic interactions which represent the main physical background. This can be achieved by discriminating events based on the signal in the ZDC including the signal in the ZEM calorimeters [11].

3. Testing of ALPIDE chips

Each PhD student in the ALICE collaboration has a duty of providing help in some technical task concerning the experiment operations not related to his PhD topic. This chapter presents the main project within my service task and provides a summary of its results.

The ALICE experiment is preparing an upgrade of its apparatus that will take place during the second long shutdown of the LHC in the years 2019–2020 before the Run 3. The current ITS will be replaced with a new system having a different design and consisting of 7 layers of high-resolution silicon pixel detectors. [84] The layout of the new ITS is shown in Fig. 3.1. The innermost and the outermost layers are expected to be installed at radii of 22 mm and 430 mm, respectively. The square pixel cells are considered to have sides of 20–50 μm and thickness of each layer will be reduced to 50 μm. Such upgrade will improve the resolution of the measurement of the track impact parameter by a factor of three. The new ITS will extend the tracking range down to very low momenta and will achieve a momentum resolution of a few percent up to $p_T \approx 20\,\text{GeV}/c$. An increased read-out speed is also required in order to enable recording of Pb–Pb collisions at a rate of 50 kHz. [85]
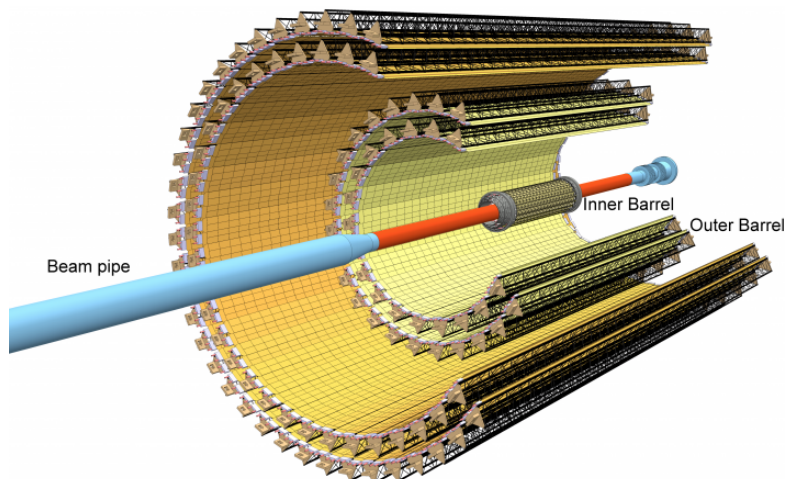
Figure 3.1: Layout of the new ITS detector [85].

The pALPIDEfs chip is one of several chips developed for research towards the design of the final ALPIDE chip which has been proposed for the ITS upgrade. The pALPIDEfs chip has been designed mainly to explore specific aspects related to integration of particular technologies.

The pALPIDEfs chip is a particle detector based on Monolithic Active Pixels Sensor (MAPS) technology implemented in a 180-nm CMOS technology for CMOS Imaging Sensors. Its sensitive area consists of square silicon pixels with sides of 28 μm arranged in 1024 columns and 512 rows, organized in 32 readout regions on an area measuring 15.3 mm by 30 mm. [86]

Each pixel provides a discriminated binary output. A trigger signal initiates collection of charge that was released in the pixel during the response interval. Output is written into an in-pixel storage cell. The pixels feature built-in circuit for test pulse injection triggered by an external signal. This allows to inject

a defined test charge in the input nodes for test purposes using voltage applied to a dedicated capacitor. A digital-only test pulse mode is also available, forcing the writing of a logic one in the in-pixel memory cell [86].

The task of the ALICE group at Řež was to determine irradiation resistance of the chip prototypes using a proton beam provided by the local cyclotron. My main contribution to this effort was to perform initial tests of not irradiated chips in order to determine the chip response as a function of several parameters. Software providing a set of several test procedures had been developed for this purpose. Using this program I could measure the response of individual pixels under different conditions specified by selected values of voltage and current parameters and their combinations which modified the behaviour of the chip. These signals are generated by a set of digital-to-analogue converters (DACs). Each pixel has a charge threshold which determines the range of detectable charge and allows to suppress noise. The threshold is defined by the interplay of three DAC signals: ITHR, VCASN and IDB. It can be increased by increasing ITHR or IDB or by decreasing VCASN.

Tests were performed on two prototypes of pALPIDEfs chips: version 2 and 3. The setup of the measurement is displayed on the photograph in Fig. 3.2. The chips had to be covered during the tests since the chip performance is sensitive to light. In the context of testing, the most obvious difference between versions 2 and 3 is in geometry where the pixel matrix is divided into 4 sectors on pALPIDEfs-2 and 8 sectors on pALPIDEfs-3. Individual sectors within each chip also differ in construction of the charge collection diodes. The prototype pALPIDEfs-3 has several additional DACs, among which VCASN2 which is related to VCASN.
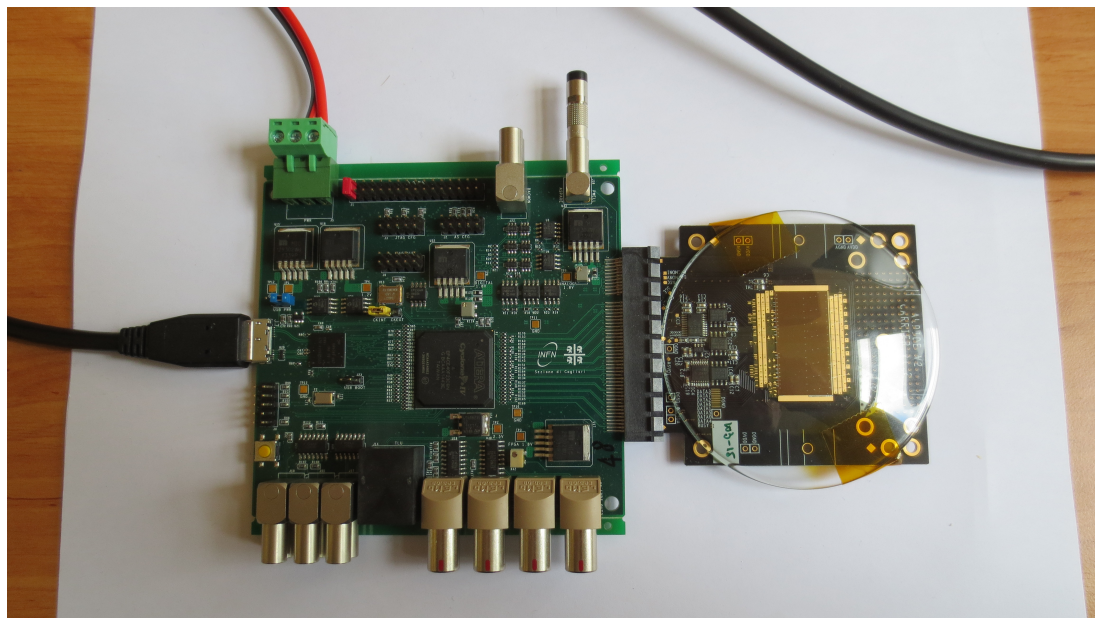
Figure 3.2: Setup for performing tests of the pALPIDEfs chips. The chip carrier on the right with the chip in the middle of it and covered by glass is connected to the operating electronics on the left. A USB port providing connectivity with a notebook is connected to the left side of the operating board. The power supply cable can be seen connected at the top.

I made use of an existing code for the analysis of the output of tests and then improved and extended it.

The following test procedures were used.

- `FIFO` is a basic test of the chip electronics. The output of the test provides information about currents and temperature.

- `SCANDACS` (DAC scan) is a measurement of the relation between the input charge and the output current or voltage of individual DACs. The dependence of the output on the charge is plotted for the ITHR parameter of pALPIDEfs-3 in Fig. 3.3. The dependence was fit with a lin-
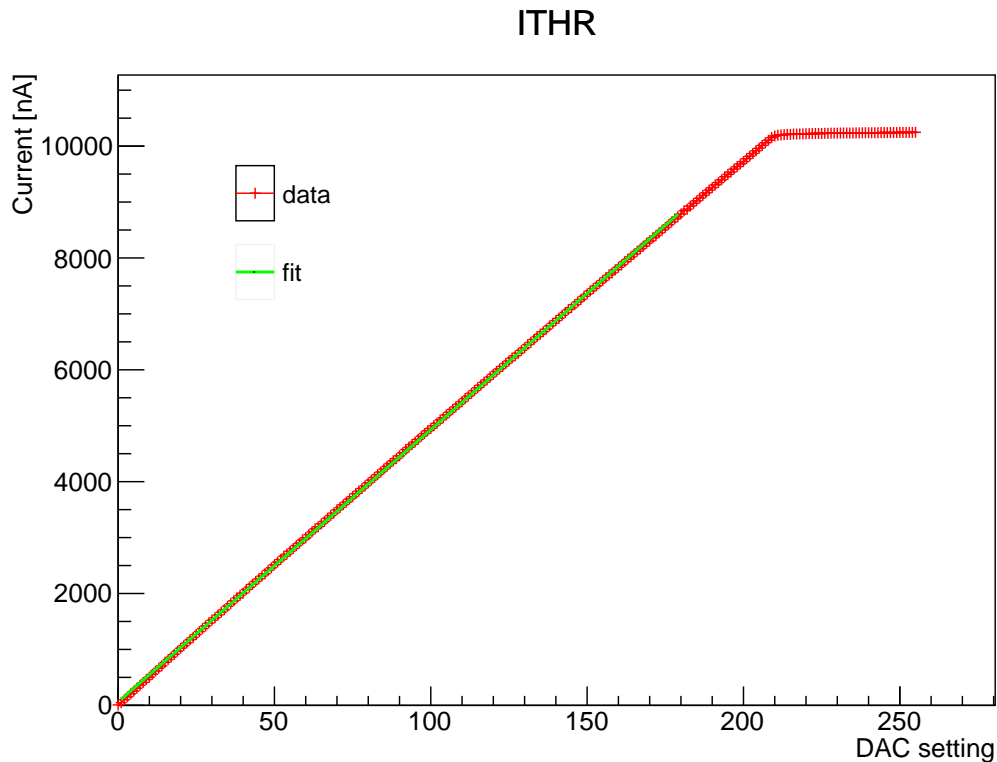
ITHR

Figure 3.3: Example of the DAC scan result for the parameter ITHR.

ear function in the range 0–180 DAC in order to determine corresponding slopes. Slopes of voltage and current DACs obtained for pALPIDEfs-2 are around $0.007\,\mathrm{V/DAC}$ and $42\,\mathrm{nA/DAC}$, respectively, which is compatible with values reported for other similar prototypes. Slopes of voltage DACs for pALPIDEfs-3 are in the range 47–$49\,\mathrm{V/DAC}$ which has been also confirmed as normal.

- `SCANDIGITAL` (digital scan) tests recording and readout of the signal stored in the chip memory. For each selected pixel, an artificial digital signal (pulse) is created after the discriminator. A logical one is written into the corresponding memory cell and it is tested whether the value can be read out. The number of generated pulses can be set by the user. In an ideal case, the number of registered hits is equal to the number of generated pulses.

  On the pALPIDEfs-2 chip, the digital scan revealed only 2 faulty pixels. In case of the pALPIDEfs-3 chip, one horizontal and one vertical structures

of faulty pixels were identified resulting in 601 pixels not responding and 6 pixels responding partially during the digital scan. The pattern can be seen on the hit map in Fig. 3.4.
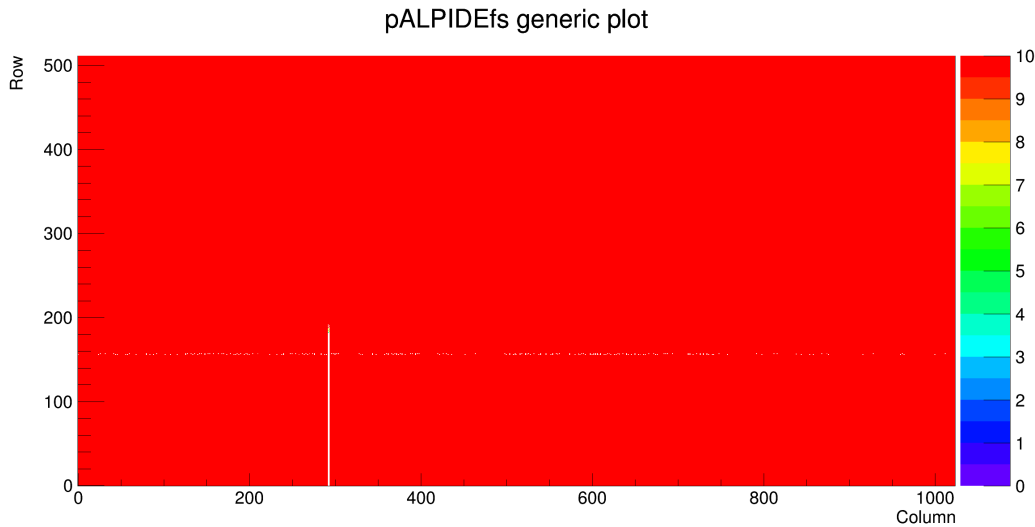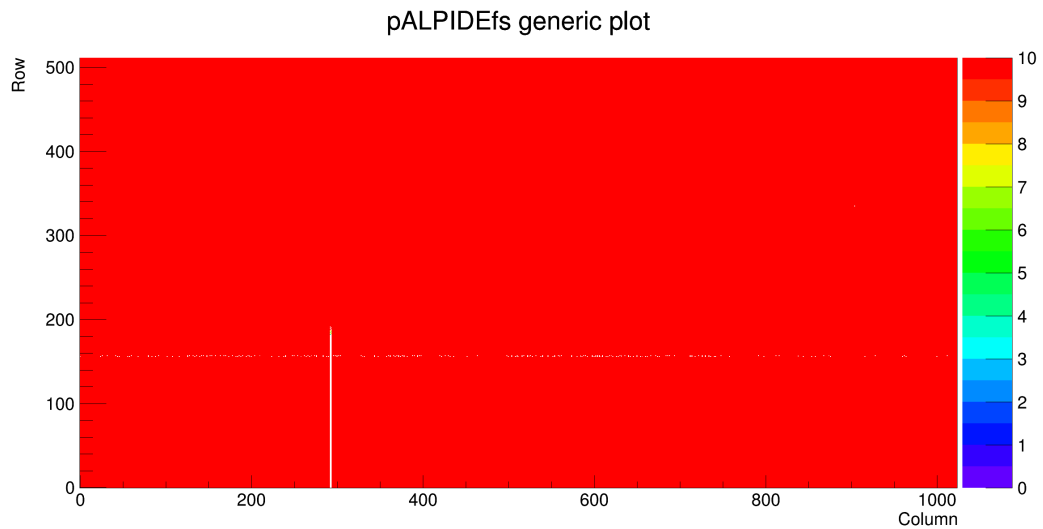

Figure 3.4: Output of a digital scan of the pALPIDEfs-3 chip, displayed on the hit map, where the z axis indicates the number of hits.

- **SCANANALOGUE** (analogue scan) tests recording and readout of the signal using also the preamplifier and the discriminator. An artificial signal is created by injecting a defined charge into the preamplifier. Typical charge value is $50\,\mathrm{DAC}$ where $1\,\mathrm{DAC} \approx 7e$. Maximal recommended reasonable charge value is about $170\,\mathrm{DAC}$. The number of generated pulses can be set by the user. In an ideal case, the number of registered hits is equal to the number of generated pulses.

  It had been reported that for the version 3 for some combinations of VCASN and VCASN2 significant fractions of pixels manifested a reduced response. Since this relation was not well known, only empirical recommendations were given on how to set one value relative to the other. I performed multiple analogue scans probing the response as a function of both parameters in a broad range of values around the default ones, leaving the remaining DACs at their default values. The number of bad pixels as a function of VCASN and VCASN2 is plotted in Fig. 3.5. Based on the results, I defined a safe region of combinations of VCASN and VCASN2. For all the later tests performed with the chip version 3, I used the relation VCASN2 $=$ VCASN $+ 10$ and as the default settings I used VCASN $= 55$. An example of a hit map from an analogue scan is displayed in Fig. 3.6.

  On the pALPIDEfs-2 chip, 4 pixels did not respond and 27 pixels did not reach the full number of hits in the analogue scan performed at the default settings. In case of the pALPIDEfs-3 chip, the basic analogue scan revealed one more dead pixel with respect to the result of the digital scan.

- **THRESHOLD** (threshold scan) tests how the efficiency of record and readout of the signal depends on the charge. The range of acceptable response as
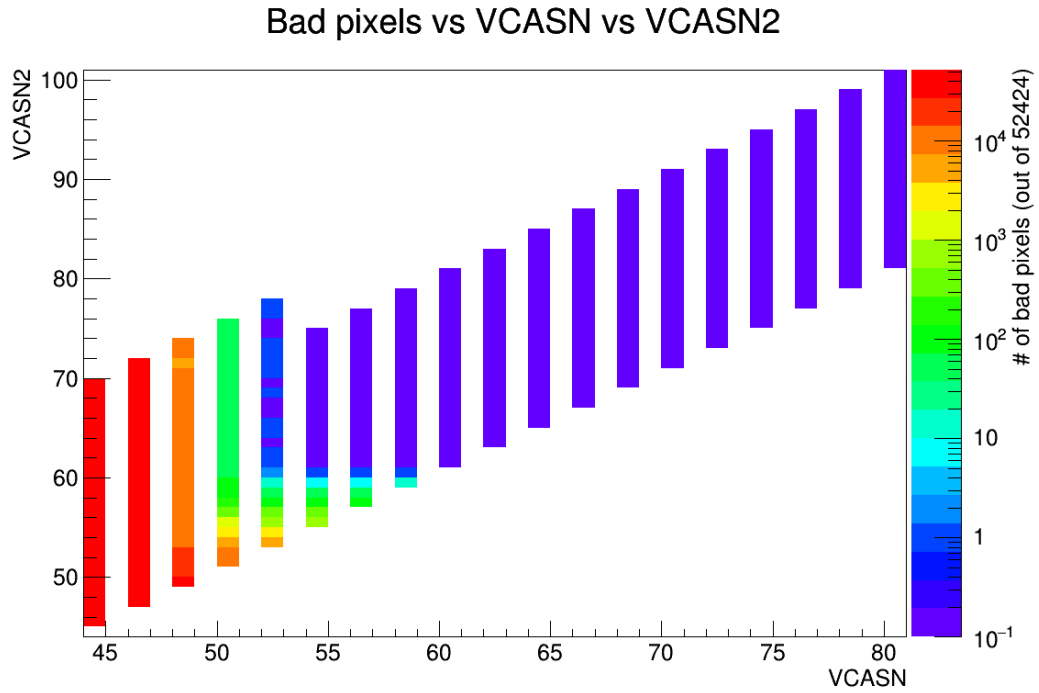
Figure 3.5: Results of the measurement of the number of bad pixels in the pALPIDEfs-3 chip as a function of the parameters VCASN and VCASN2. The scanned regions with no bad pixels have the value 0.1 assigned.

Figure 3.6: Output of an analogue scan of the pALPIDEfs-3 chip, displayed on the hit map, where the z axis indicates the number of hits.

a function of the injected charge is expressed by a threshold value for each pixel. The test performs an automatized analogue scan looping over values of charge within a selected range (typically 0–50 DAC) with step of 1 DAC. The number of generated pulses per pixel and per charge value is fixed to 50. A normal pixel does not register any pulses for small charge values (i.e. 0 hits are registered). The number increases with increasing charge and half of the number of pulses (25) are registered for a charge value corresponding to the threshold. For large charge values, the efficiency saturates and the pixel registers all 50 generated pulses. This dependence can be fitted using the error function. Its width (corresponding to the slope of reaching the full response) is sometimes denoted as noise or threshold width. Noisy pixels register fake pulses even for small charge values. The features mentioned above can be seen in Fig. 3.7 that shows the response of a noisy pixel plotted as a function of charge and fitted with the error function. Since one
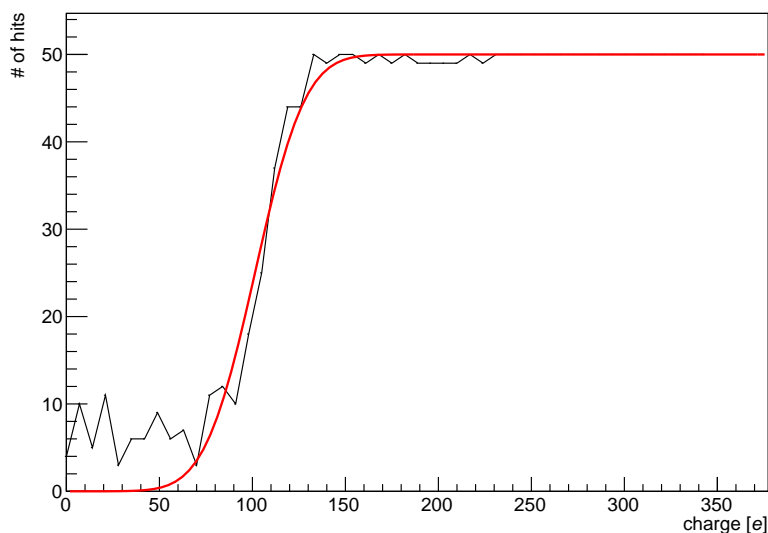
Figure 3.7: Estimation of threshold of a noisy pixel using a fit with the error function.

typical threshold scan performed on the full chip takes 8.5 h, the dependence of the thresholds on the DAC values has been scanned using only 10 % of pixels. The Fig. 3.8 shows the distribution of thresholds of pixels in individual sectors of the chip pALPIDEfs-2. No difference between the threshold distribution of even and odd rows of pixels has been observed, contrary to results of earlier tests on similar chip prototypes. Similar distributions are available for the threshold width. In both cases the mean values and the RMS values are extracted from the distributions and reported as a function of DAC values. Examples of results corresponding to the pALPIDEfs-3 chip are plotted in Figures 3.9, 3.10 as a function of VCASN and in Figures 3.11, 3.12 as a function of ITHR.

- NOISEOCC (noise occupancy scan) maps electronic noise. A defined number of random triggers are generated progressively. Only readout is performed and fake hits are registered. The list of pixels and corresponding hit rates
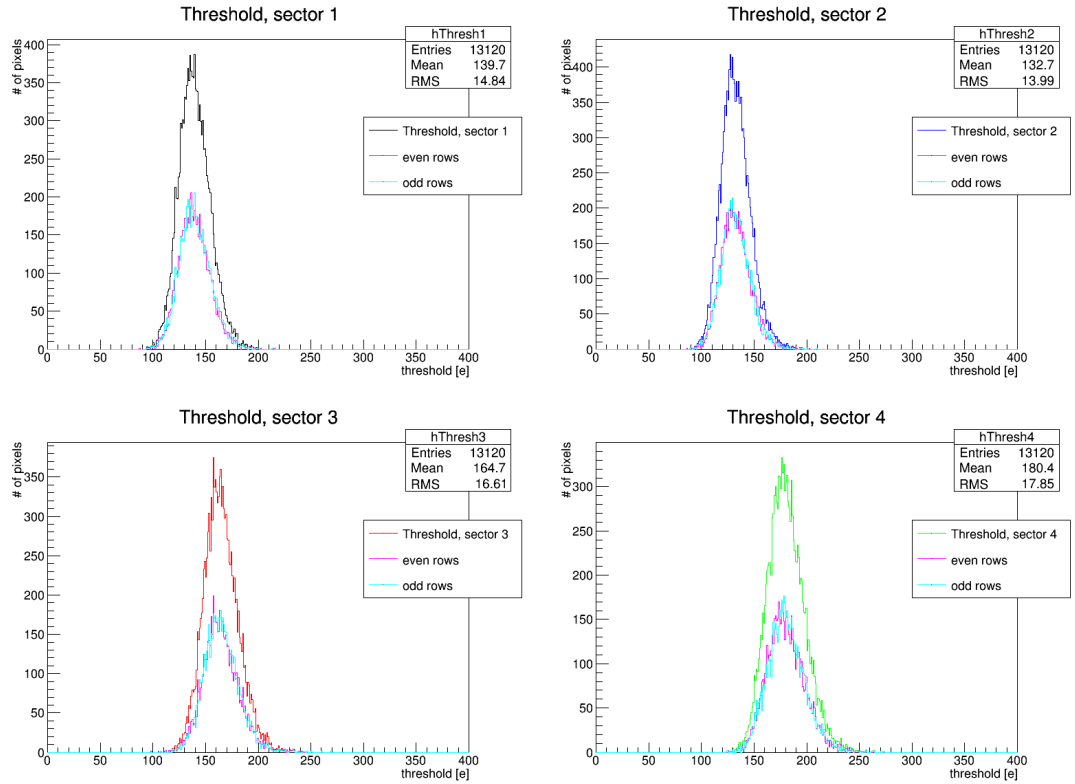
Figure 3.8: Threshold distribution in pixels in individual sectors of the pALPIDEfs-2 chip.
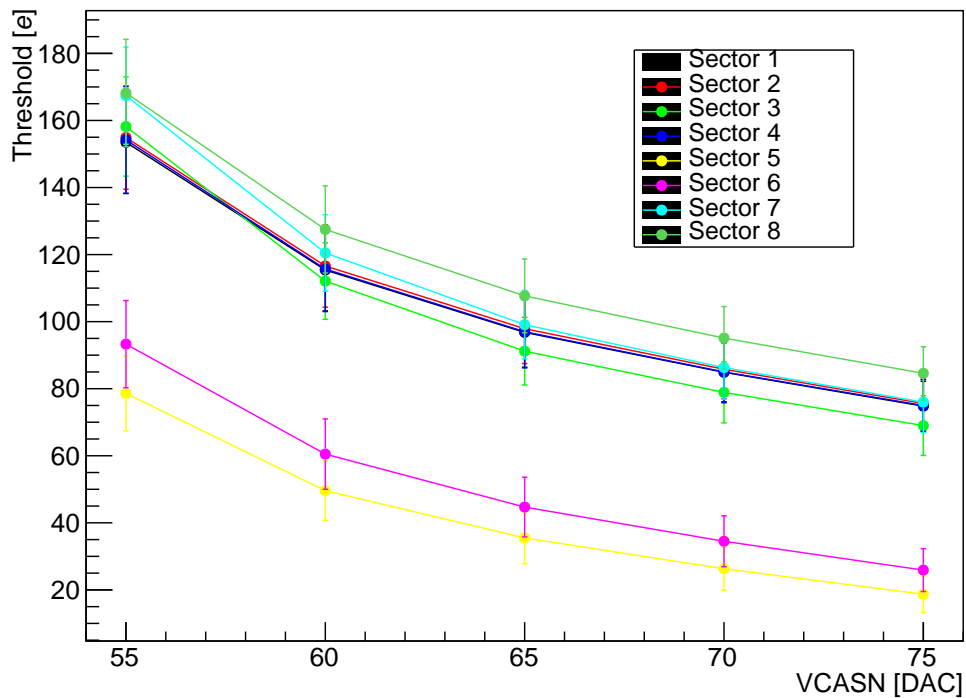
Figure 3.9: Mean threshold as a function of VCASN for ITHR = 60 for each of the 8 sectors of the pALPIDEfs-3 chip.
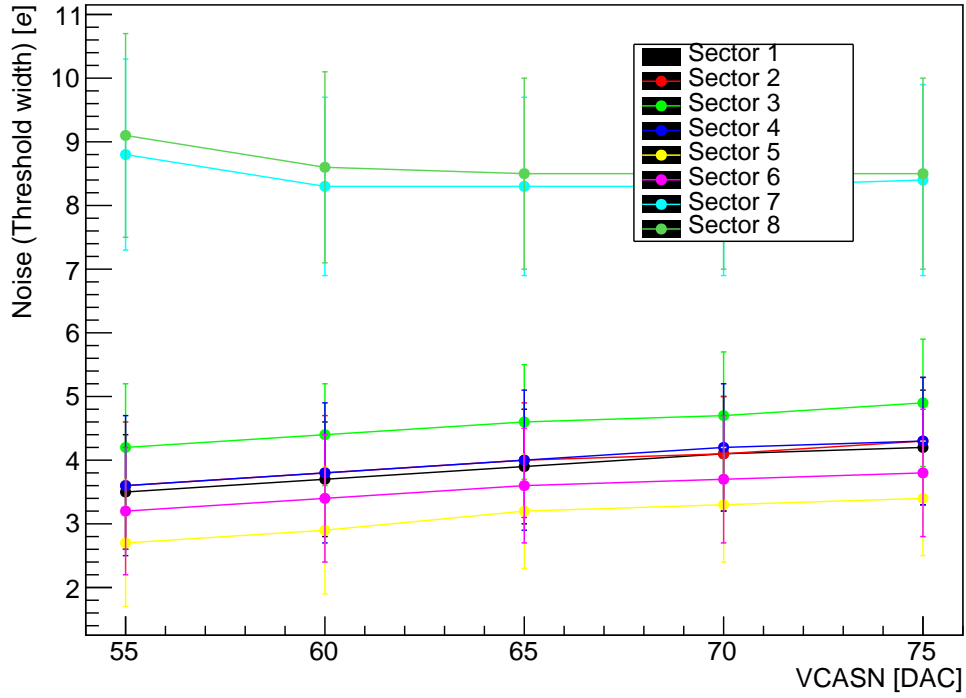
Figure 3.10: Mean threshold width as a function of VCASN for ITHR = 60 for each of the 8 sectors of the pALPIDEfs-3 chip.
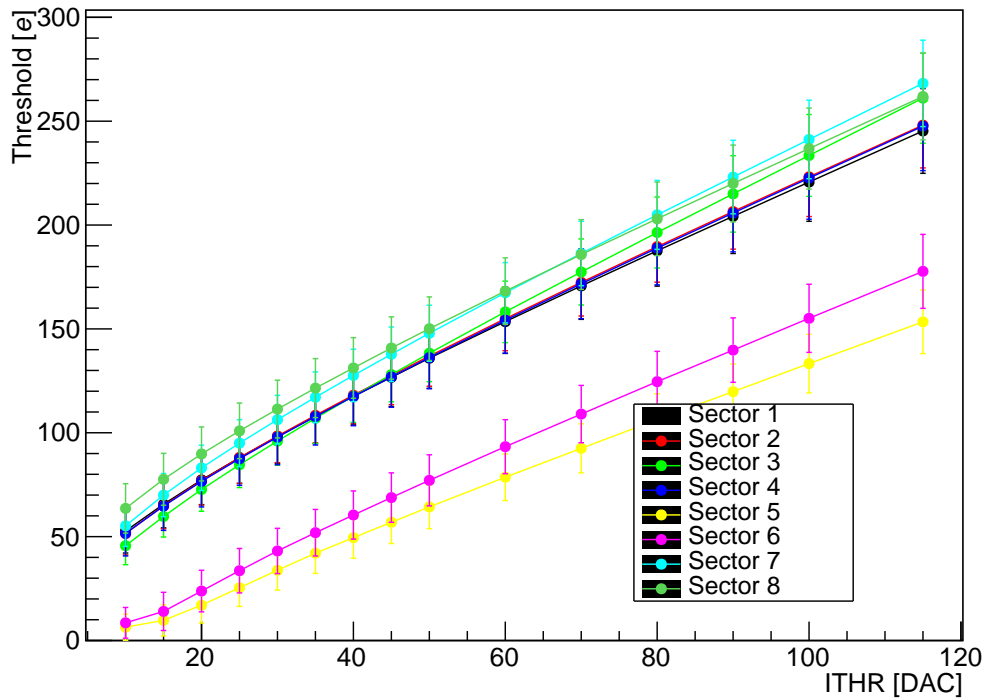

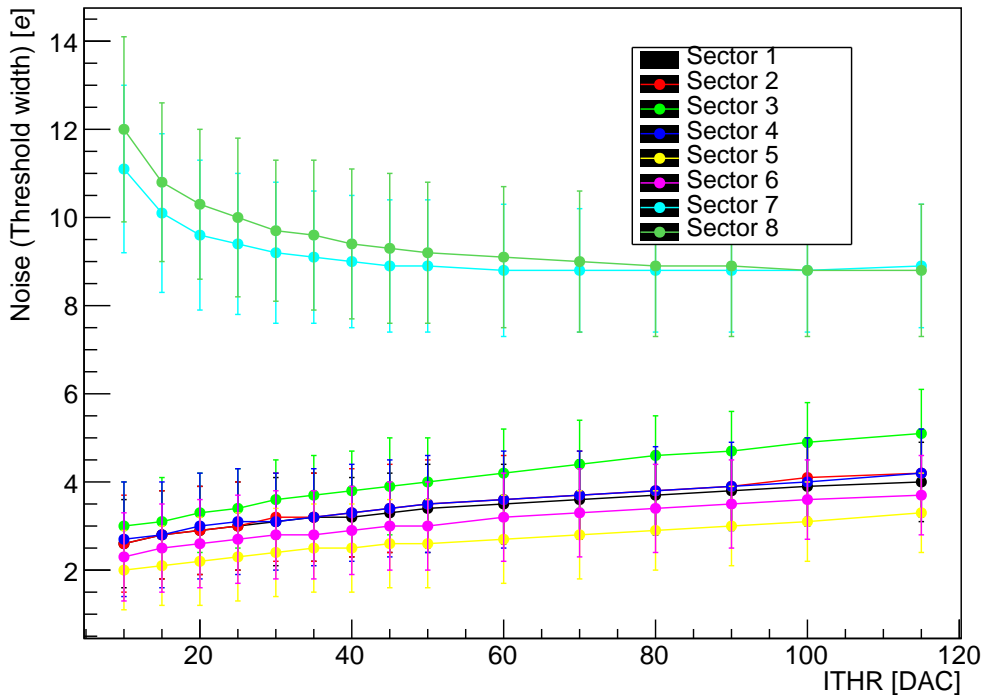Figure 3.11: Mean threshold as a function of ITHR for VCASN = 55 for each of the 8 sectors of the pALPIDEfs-3 chip.

Figure 3.12: Mean threshold width as a function of ITHR for VCASN = 55 for each of the 8 sectors of the pALPIDEfs-3 chip.

are analysed for each sector separately. The results of a scan of one million events, plotted for the entire pALPIDEfs-3 chip, are presented in Fig. 3.13 expressed as the number of fake hits per event as a function of VCASN and ITHR and in Fig. 3.14 as the absolute number of noisy pixels.

- SOURCE (source scan) is a mode for irradiation of the chip by ionizing radiation from a radioactive source. Working mode is the same as for the noise occupancy scan, only the time interval dedicated for taking one event is longer in order to increase the probability of the chip being hit by an ionizing particle. A hit map corresponding to a period of irradiating the chip with an ^{241}Am source ($E_\gamma = 59\,\mathrm{keV}$) is shown in Fig. 3.15.

The results were presented and discussed at two meetings of the working group WP5 [87, 88]. My results of the chip tests have contributed to the effort of characterization of different prototypes of the ALPIDE chips. They serve as input for the experts developing the final ALPIDE chips installed in the new ITS during the planned upgrade of the ALICE detectors.
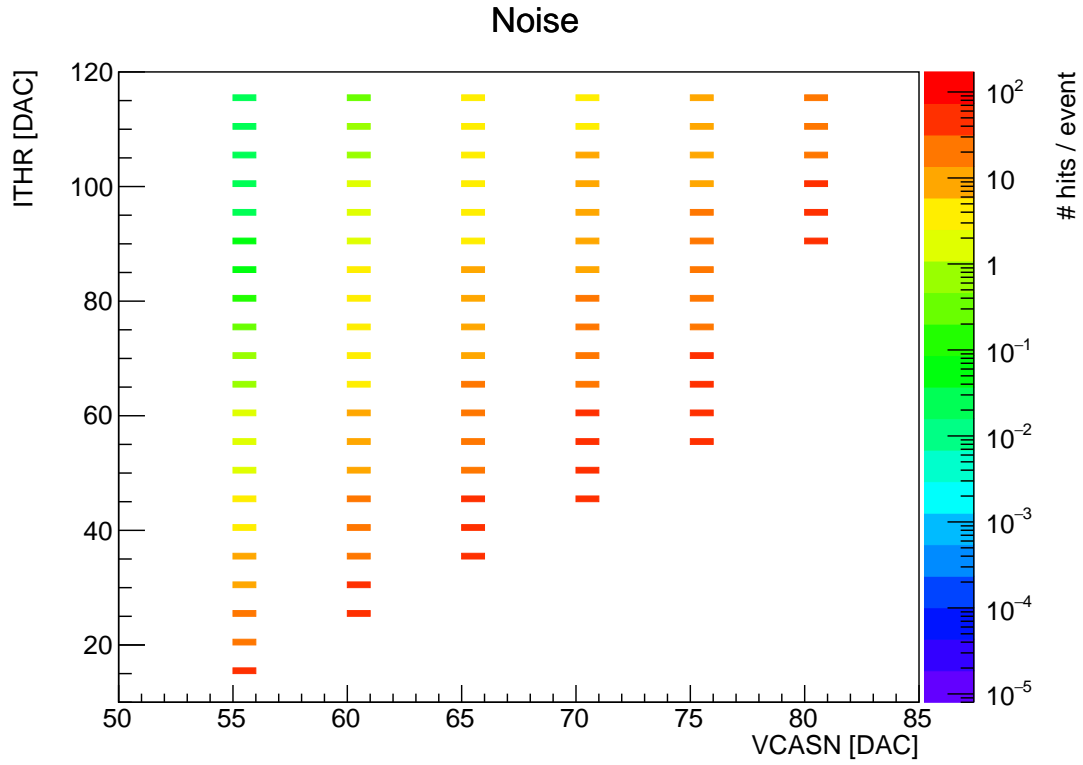
Figure 3.13: Results of the noise occupancy scan for the entire pALPIDEfs-3 chip, expressed as the number of fake hits per event.
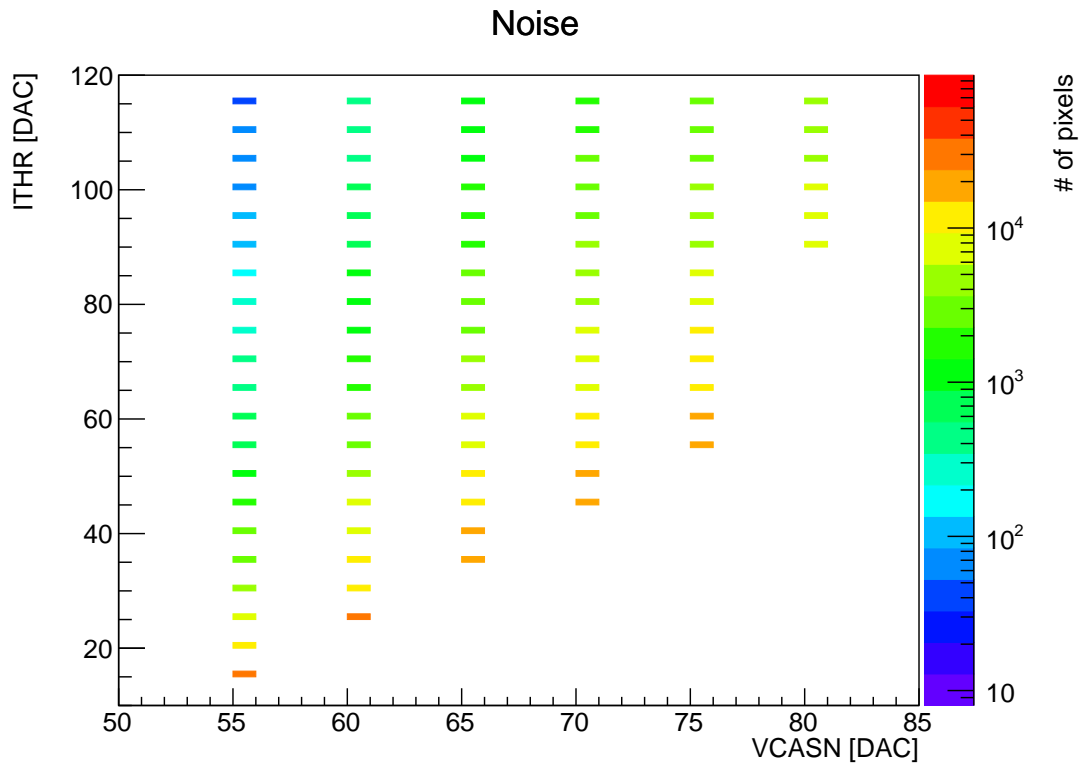
Figure 3.14: Results of the noise occupancy scan for the entire pALPIDEfs-3 chip, expressed as the number of noisy pixels.
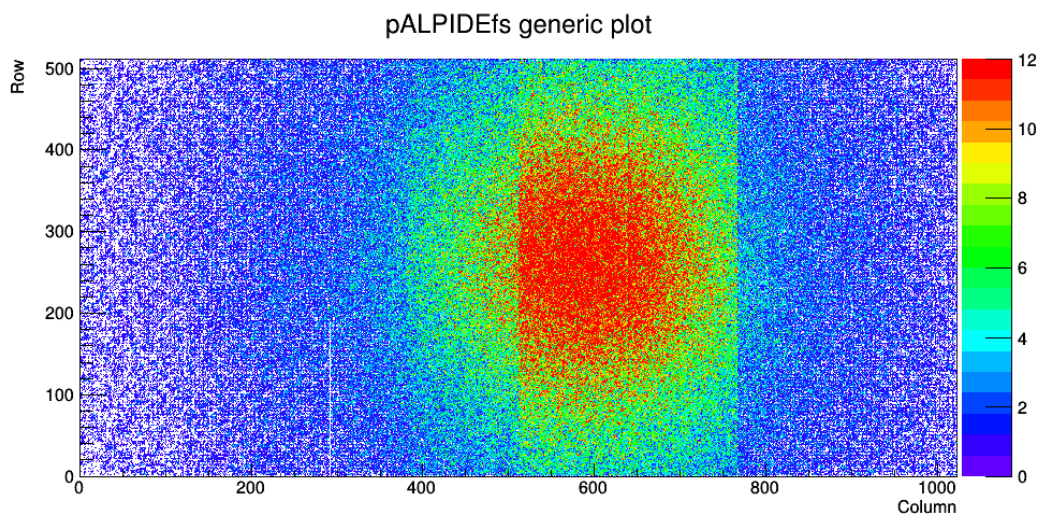
Figure 3.15: Distribution of the hits in pixels measured in the source scan while irradiating the chip with photons emitted from americium.

4. Analysis

The aim of the presented analysis is to measure spectra of Λ baryons and K_S^0 mesons produced in association with charged jets in central Pb–Pb collisions recorded with the ALICE experiment at the LHC in order to determine whether the enhancement of the baryon-to-meson ratio is present also in the subset of particles produced in hard processes.

Originally, there had been two independent analyses within the ALICE collaboration focused on the production of Λ and K_S^0 particles in jets in Pb–Pb collisions: one developed by myself and one developed by Alice Zimmermann, a PhD student at the University of Heidelberg in Germany. Later we compared both analyses, performed very detailed cross-checks, synchronized the methods and continued developing the analyses together while keeping both analysis codes separate.

4.1 Data sample and event selection

The analysis is performed on data recorded in 2011 with the ALICE apparatus at the LHC during the runs with Pb–Pb collisions at the centre-of-mass energy of $\sqrt{s_{NN}} = 2.76\,\mathrm{TeV}$. The data measured in 2010 were used only for the comparison of inclusive spectra with the published results [64, 89]. Tracking of charged particles in the central barrel is provided by the Inner Tracking System and the Time-Projection Chamber, both placed in a magnetic field of $0.5\,\mathrm{T}$. The centrality of collisions is estimated from the multiplicity of charged particles measured in the V0 detectors at forward pseudorapidities.

The run selection was driven by the quality requirements for the jet reconstruction, mainly related to the uniform distribution of reconstructed tracks within the TPC acceptance. The list of chosen runs consists of 62 "good runs" [90] satisfying criteria for the reconstruction of charged jets and selected based on the results of quality-assurance (QA) checks [91, 92] and quality flags in the Run Condition Table [93]. The list of analysed runs is presented in Tab. 4.1.

Table 4.1: List of analysed runs.

167902, 167903, 167915, 167920, 167987, 167988, 168066, 168068, 168069,
168076, 168104, 168107, 168108, 168115, 168212, 168310, 168311, 168322,
168325, 168341, 168342, 168361, 168362, 168458, 168460, 168461, 168464,
168467, 168511, 168512, 168777, 168826, 168984, 168988, 168992, 169035,
169091, 169094, 169138, 169143, 169144, 169145, 169148, 169156, 169160,
169167, 169238, 169411, 169415, 169417, 169835, 169837, 169838, 169846,
169855, 169858, 169859, 169923, 169956, 170027, 170036, 170081

The following data sets of measured and simulated data on the Grid [94] were used.

- real data: LHC11h_2, AOD145

- simulated data: LHC12a17d_fix, AOD149

Analysed events are selected based on criteria on centrality and quality of reconstruction of the primary vertex.

- Central events within the centrality range 0–10 % are selected by using events labelled by the centrality trigger (`AliVEvent::kCentral`) and the minimum bias trigger (`AliVEvent::kMB`). The centrality value is obtained from the centrality estimator "V0M" which combines measurements from both scintillator arrays of the V0 detector.

- In order to ensure use of well reconstructed and optimally located primary vertex, the following requirements are imposed.

  - The vertex must be reconstructed using a fit with more than two contributing tracks.
  - The vertex position along the beam axis and in the transverse plane must fit within the acceptable range $|z| < 10$ cm, $r < 1$ cm in order to ensure uniform performance of tracking within the acceptance of the mid-rapidity detectors.
  - The vertex must not be reconstructed using only tracks measured solely by the TPC.
  - The difference between the z-coordinate of the final primary vertex and the z-coordinate of the vertex reconstructed using the Silicon Pixel Detector (SPD) must not exceed a defined value $\Delta z_{\mathrm{SPD}} = |z_{\mathrm{vertex}}^{\mathrm{SPD}} - z_{\mathrm{vertex}}^{\mathrm{nominal}}| < 0.1$ cm.

The total sample of analysed central collisions consists of 7.3×10^6 selected events.

4.2   Analysis workflow and software

The analysis of neutral strange particles in charged jets consists of two main parts: reconstruction of neutral strange particles and reconstruction of charged jets. The diagram in Fig. 4.1 shows an overview of the main analysis steps which will be described in the following sections of this chapter.

The analysis has been carried out using several software tools. The main analysis environment used by members of the ALICE collaboration is built as an extension to ROOT [95] and consists of two distinct parts: AliRoot [96], which contains the basic code for simulation, reconstruction and analysis, and AliPhysics [97], which contains the code for individual users' analyses and related code. Implementation of jet reconstruction algorithms is provided by the FastJet package (version 3.0.6) [98]. Third-party extensions of FastJet can be used by loading the FastJet-contrib package [99]. The passage of particles through the material of the ALICE apparatus is simulated using GEANT3. For simulation of p–p collisions at $\sqrt{s} = 2.76$ TeV, the PYTHIA 8 [100, 101] event generator is used.

The code related to this analysis can be found in three analysis tasks. The task `AliAnalysisTaskV0sInJetsEmcal` [102] is my class written to work within the newer "EMCal framework" which has become the new standard code for
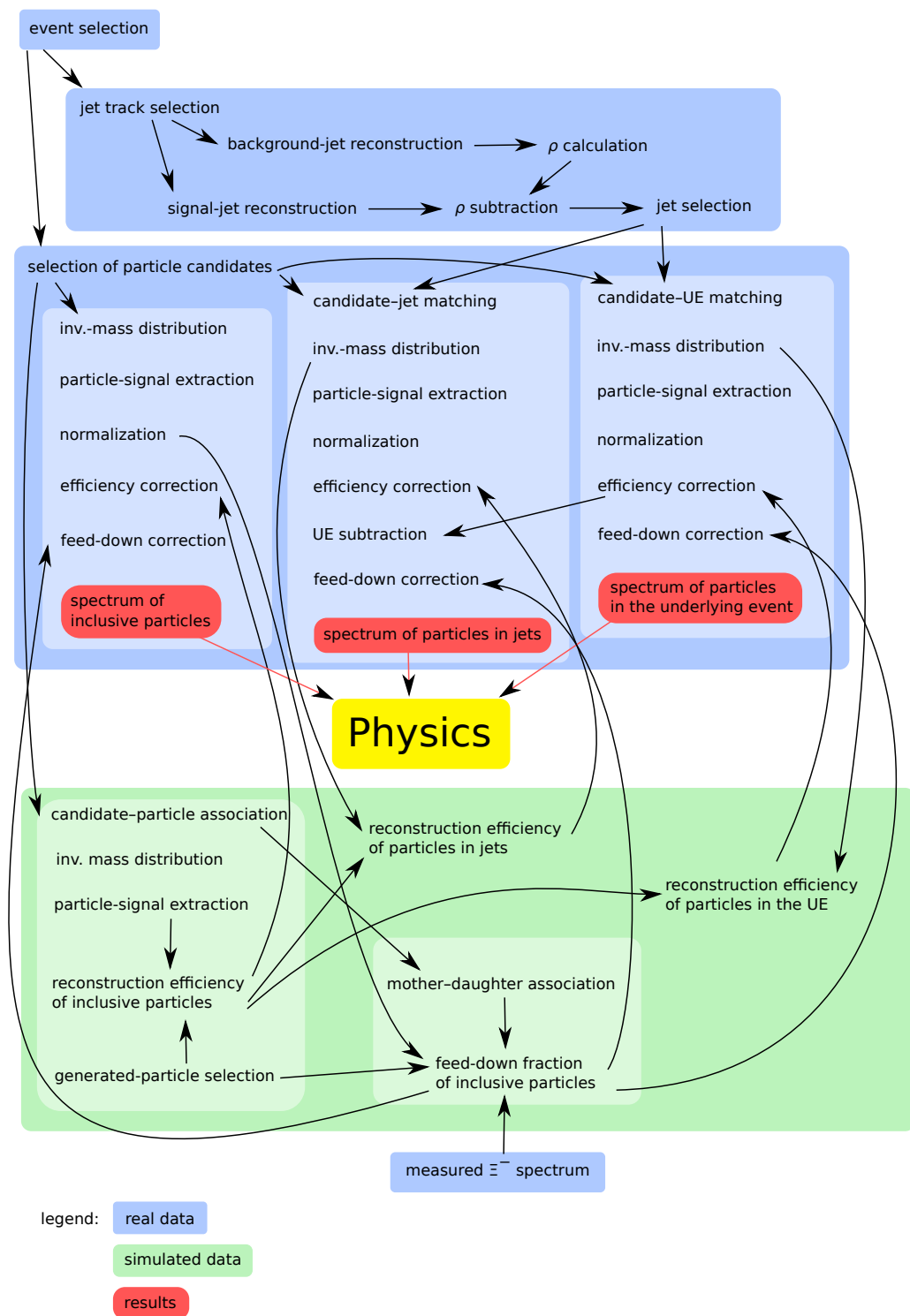
Figure 4.1: Analysis workflow.

jet reconstruction. This class replaced the now obsolete class `AliAnalysisTask-VOsInJets` [103], which was written for the older ALICE jet analysis framework (JETAN). The analysis task of Alice Zimmermann is contained in the class `Ali-AnalysisTaskJetChem` [104] which works within the JETAN framework.

4.3 Analysis of neutral strange particles

4.3.1 Particle reconstruction

K_S^0 meson and Λ $(\overline{\Lambda})$ baryon are neutral strange particles referred to as so called "V^0 particles", since they have no electric charge and decay by weak interaction into a pair of charged daughter particles which produces a characteristic signature of a V-shaped configuration of two tracks bent by a magnetic field. This decay topology is used for their reconstruction (as depicted in Fig. 4.2) from tracks of their charged daughter particles.
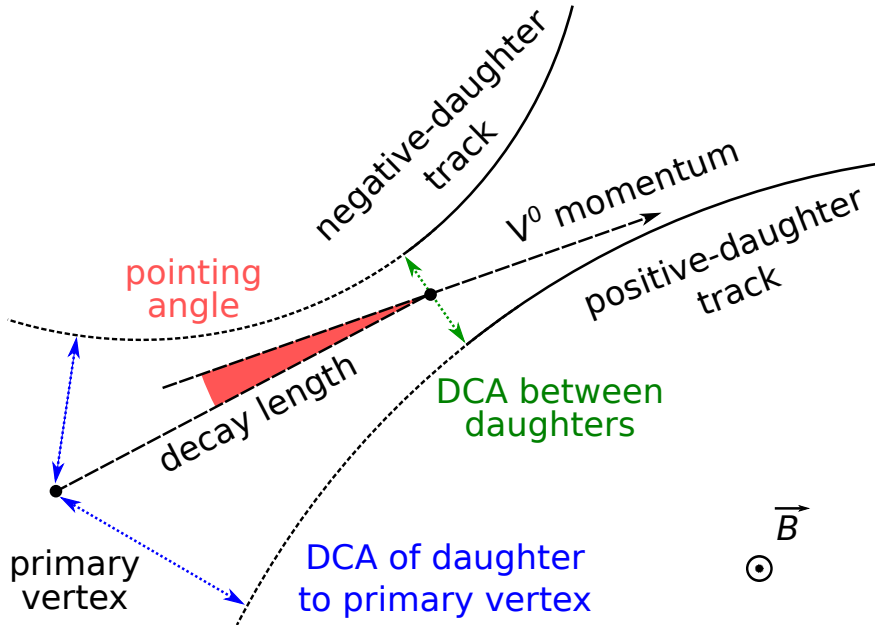
Figure 4.2: Topological properties of a V^0 decay.

The V^0 particles are reconstructed using their most frequent decay channels:

- $K_S^0 \rightarrow \pi^+ + \pi^-$ (branching ratio 69 %, $\tau \approx 9 \times 10^{-11}$ s),

- $\Lambda \rightarrow p + \pi^-$, $\quad \overline{\Lambda} \rightarrow \overline{p} + \pi^+$ (branching ratio 64 %, $\tau \approx 3 \times 10^{-10}$ s).

A list of candidates for V^0 particles, resulting from the global tracking and subsequent processing, is already present in the analysed data files. The list is further filtered at the analysis level in order to reduce the high contribution of fake candidates, coming from combinatorial background, without rejecting too large fraction of the signal, represented by well identified particles. The V^0 candidates are selected using topological and other cuts applied to properties of the secondary vertex and of the daughter tracks. Criteria used in this analysis are very similar to those used in the measurement of inclusive spectra [64].

A quality flag called "TPC refit", related to the stages of track reconstruction, is required for the daughter tracks. Daughter tracks reconstructed as belonging to kink vertices tracks are rejected. The distance of the closest approach (DCA) between extrapolated daughter tracks and the primary vertex must be greater than 0.1 cm in order to reject primary tracks. The DCA between daughter tracks must be less than one standard deviation of the tracking resolution in the TPC. Only daughter tracks reconstructed in the pseudorapidity window $|\eta| < 0.8$ are accepted. Particle identification of daughter particles using energy loss $\mathrm{d}E/\mathrm{d}x$ is not applied, since it does not have a significant effect for $p_\mathrm{T}^{\mathrm{V}^0} > 2\,\mathrm{GeV}/c$.

There are two kinds of V^0 candidates available in the data, produced by two different algorithms. "On-the-fly" candidates are found during the global tracking procedure. A different procedure is used for finding V^0 candidates later ("offline"), in the subsequent processing of recorded data. In this analysis, only the offline-reconstructed candidates are used. A candidate is accepted only if cosine of the pointing angle is larger than 0.998 to select preferentially primary V^0 particles and to reduce contribution of V^0 particles produced by decays. Range of acceptable distance of the decay vertex from the z-axis is restricted to the interval 5–100 cm. The V^0 candidates are required to lie in the pseudorapidity range $|\eta_{\mathrm{V}^0}| < 0.7$. A cut is applied to the "transverse proper lifetime" t^*, calculated for a given assumption of the candidate being a V^0 particle as $ct^* = \frac{mc^2 r}{p_\mathrm{T} c}$, where m is the rest mass of the assumed V^0 particle and r is the projection of the decay length into the transverse plane. The transverse proper lifetime must be less than five times the mean lifetime expressed as $c\tau$ which is taken to be 2.6844 cm and 7.89 cm for K_S^0 and Λ ($\overline{\Lambda}$), respectively [1]. A cut in the Armenteros–Podolanski diagram [105] is used to suppress the contamination of the K_S^0 candidates with Λ and $\overline{\Lambda}$ particles.

The complete summary of criteria used for selection of V^0 candidates is presented in Tab. 4.2.

Table 4.2: Summary of V^0 selection cuts.

Cut variable	Value
Daughter tracks	
TPC refit	`true`
type of production vertex	not `kKink`
DCA to the primary vertex	$\geq 0.1\,\mathrm{cm}$
DCA between daughters	$\leq 1\sigma_{\mathrm{TPC}}$
$|\eta|$	≤ 0.8
V^0 candidate	
reconstruction method	offline
cosine of the pointing angle (CPA)	≥ 0.998
radius of the decay vertex	5–100 cm
$|\eta|$	≤ 0.7
transverse proper lifetime	$\leq 5\tau$
Armenteros–Podolanski cut (K_S^0)	$p_\mathrm{T}^{\mathrm{Arm.}} \geq 0.2|\alpha^{\mathrm{Arm.}}|$

Unless specified otherwise, $\overline{\Lambda}$ particles are treated in the analysis independently and in the same way as Λ particles. Spectra of Λ baryons and $\overline{\Lambda}$ baryons are eventually combined into the baryon-to-meson ratio as $(\Lambda + \overline{\Lambda})/2\mathrm{K}_\mathrm{S}^0$.

4.3.2 Signal extraction

Selected candidates, satisfying criteria for a given particle species (K_S^0, Λ or $\overline{\Lambda}$), are used by filling values of their various properties into multi-dimensional histograms. The key quantity for determining the amount of well identified particles among the selected candidates is invariant mass, calculated from momenta of daughter tracks, where mass values are assigned to daughter tracks according to their charges, the assumption about identity of the V^0 candidate and its decay channel. The resulting invariant-mass distribution consists of a peak, containing signal from true V^0 particles, sitting on a pedestal of continuous mainly combinatorial background. The combinatorial background is fitted with a parametrized curve in regions outside the peak ("side bands") and signal is obtained by subtracting the corresponding background contribution from the sum of entries in the signal region. Examples of the signal extraction are presented in Fig. 4.3 for K_S^0 and Λ particles associated with jets in three $p_T^{V^0}$ bins. Black regions indicate the side bands and the blue regions are the signal regions.

The signal extraction from the invariant-mass distribution is performed in the following steps.

- First, I fix the maximum range of invariant mass m_{inv} which cannot be exceeded in any calculation:

$$K_S^0 : \quad m_{inv}/(\text{GeV}/c^2) \in [0.38, 0.65], \tag{4.1}$$

$$\Lambda : \quad m_{inv}/(\text{GeV}/c^2) \in [1.1, 1.155]. \tag{4.2}$$

  This is useful especially for side bands of Λ candidates if their position depends on $p_T^{V^0}$, since they might start to overlap at high $p_T^{V^0}$ with the steep edge at low m_{inv} or with the region of curvature at $m_{inv} \approx 1.16\,\text{GeV}/c^2$ which distorts the fit.

- Second, I determine the signal region and the side band regions, which can be done in several ways.

  In this analysis, I use manually fixed ranges. It provides independent tuning of all 3 regions and a good shape description of the side bands. The disadvantage of this approach is that the side bands may be far away from the K_S^0 peak in the case of low $p_T^{V^0} \approx 2\,\text{GeV}/c$.

  - signal regions:

$$K_S^0 : \quad m_{inv}/(\text{GeV}/c^2) \in [0.43, 0.57], \tag{4.3}$$

$$\Lambda : \quad m_{inv}/(\text{GeV}/c^2) \in [1.105, 1.13]. \tag{4.4}$$

  - side band regions:

$$K_S^0 : \quad m_{inv}/(\text{GeV}/c^2) \in [0.38, 0.65] \setminus [0.43, 0.57], \tag{4.5}$$

$$\Lambda : \quad m_{inv}/(\text{GeV}/c^2) \in [1.1, 1.155] \setminus [1.105, 1.13]. \tag{4.6}$$

  The ranges are chosen carefully to maximize the fraction of yield extracted in the signal region in real and simulated data and to be wide enough for stable fitting of the side bands.
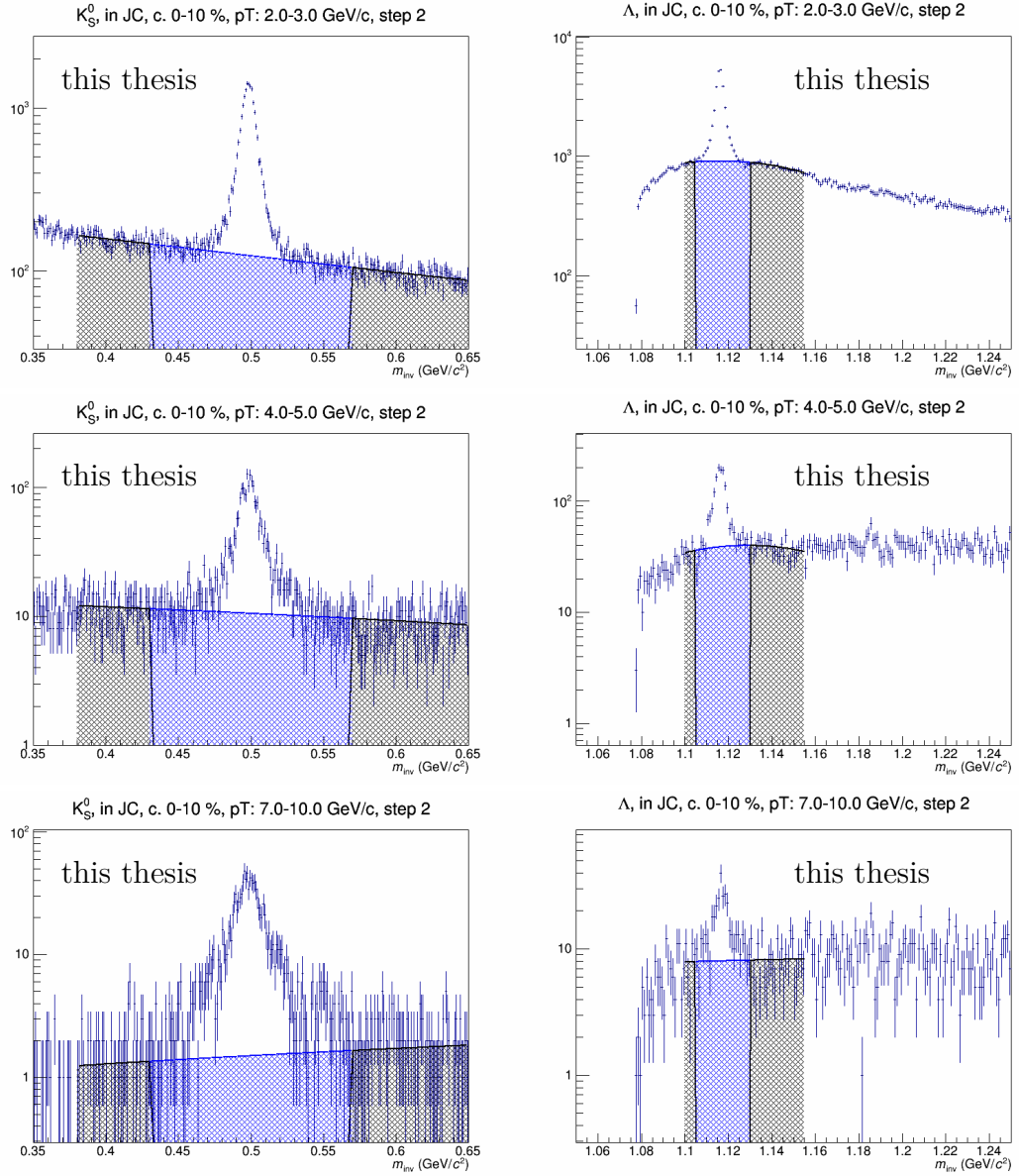
Figure 4.3: Examples of signal extraction for K^0_S and Λ found in jet cones (JC) in three $p^{V^0}_T$ bins in central (0–10 %) Pb–Pb collisions at $\sqrt{s_{NN}} = 2.76\,\mathrm{TeV}$ from year 2011.

Another option is to define regions in terms of the mass peak centre μ and the peak width σ which are obtained by fitting the peak together with the background with a sum of the Gaussian and a polynomial. The boundaries of regions are then expressed in multiples of the peak width as $\mu \pm n\sigma$. This method enables to keep the side bands closer to the peak for any $p_{\mathrm{T}}^{\mathrm{V}^0}$ but is very sensitive to statistical fluctuations, shape of the signal peak and overlap of side bands with tails of the non-Gaussian peak. Since there were always some $p_{\mathrm{T}}^{\mathrm{V}^0}$ bins where this method failed to fit the side bands, it was not used at all in this analysis.

- Next step is to fit the side bands with a polynomial.

  The default (and maximum) degree of polynomial is 2 for $\mathrm{K}_{\mathrm{S}}^0$ and 3 for Λ. If the mean number of entries per bin in either side band is less than 20, the degree is decreased to 1 (linear). If the mean number of entries per bin in either side band is less than 1, the degree is decreased to 0 (constant). The fit is performed using the built-in function `TH1::Fit` in ROOT via the likelihood method within the defined range (fit option "SLRI"). Successful convergence and quality of the fit are verified using the following conditions:

    - fit result is valid (`TFitResultPtr::IsValid = kTRUE`),
    - fit converged (`TFitResultPtr::Status = 0` or `4000`),
    - covariance matrix is accurate (`TFitResultPtr::CovMatrixStatus = 3`).

  If the fit fails, another attempt is made with a lower degree of polynomial.

- The final stage is the extraction of the signal by subtraction of the background.

  Raw signal (noted "signal + bg") is added up over bins within the signal region ("sig. region"). Result of the fit of the side bands ("fit bg") is integrated in the signal region. The integral is divided by the bin width of the invariant-mass histogram and subtracted from the raw signal:

$$\sum_{\text{sig. region}} \text{signal} = \left(\sum_{\text{sig. region}} (\text{signal} + \text{bg}) \right) - \left(\int_{\text{sig. region}} (\text{fit bg}) \right) \Big/ (\text{bin width}). \tag{4.7}$$

  Uncertainty of the raw signal ($\text{err}_{(\text{signal}+\text{bg})}$) is estimated as the square root of the total number of entries.

  Uncertainty of the integral ($\text{err}_{(\text{fit bg})}$) is obtained using the covariance matrix.

  The final uncertainty of the signal extraction ($\text{err}_{\text{signal}}$) is determined by combining quadratically both uncertainties:

$$\text{err}_{\text{signal}}^2 = \text{err}_{(\text{signal}+\text{bg})}^2 + [\text{err}_{(\text{fit bg})}/(\text{bin width})]^2. \tag{4.8}$$

In simulated data, the signal is extracted from the invariant-mass distribution of associated particles by simply adding up entries within the signal region; i.e. no background needs to be subtracted nor estimated.

4.4 Analysis of charged jets

4.4.1 Jet reconstruction and definition

The jet reconstruction is performed using the anti-k_t jet algorithm, that belongs to the class of sequential recombination jet algorithms and is implemented in the FastJet [98] package. Tracks of detected charged primary particles serve as input for the jet algorithm which clusters them into "charged jets". The tracks used for the jet reconstruction had to fulfil criteria of the "hybrid track" selection [106], that are commonly used in the ALICE jet analyses.

The jet reconstruction is performed by the AliPhysics analysis task `AliEmcal-JetTask` [107] which makes part of the EMCal framework.

Track selection

Since some parts of the SPD were switched off during several run periods, regions of decreased efficiency in the acceptance appear in the track distributions as a function of azimuth. An approach using "hybrid tracks" has been adopted to take this inefficiency into account. Tracks that are missing space points (hits) in the SPD layers are extrapolated inwards by constraining them to originate in the primary vertex which improves their momentum resolution. These tracks are added to the ordinary well reconstructed "global" tracks. The resulting sample (called "hybrid tracks") contains primary tracks with acceptable momentum resolution and with uniform distribution in $\eta \times \phi$ within the TPC acceptance [106].

Only tracks of primary charged particles with p_T greater than $150\,\mathrm{MeV}/c$ are accepted for the jet reconstruction and the pseudorapidity is restricted to the range $|\eta_\mathrm{track}| < 0.9$ where the full width of the TPC is available for the track reconstruction.

Jet definition

Calling an object a "jet" requires selection of a jet definition. This consists in choosing a jet algorithm, its parameters and a recombination scheme [98].

The following settings are used for the jet finding in this analysis.

- jet algorithm: anti-k_t (for signal jet), k_t (for background estimation)

- parameters:

  - resolution parameters: $R = 0.2, 0.3$

  - algorithmic strategy for clustering: automatic selection

- recombination scheme: p_T-weighted recombination scheme assuming massless particles ($E = |\boldsymbol{p}|$)

In order to estimate the p_T-density of background particles, it is needed to determine areas of reconstructed jets (A_jet). Two main definitions of jet areas can be used in FastJet: active and passive areas. Active areas are chosen here as being convenient for estimating the susceptibility of jets to contamination from an underlying event with uniform, diffuse distribution in the event. Active jet

areas are calculated by FastJet by covering the acceptance with extremely soft particles ("ghosts") and counting how many are clustered inside a given jet [108].

The following settings are used for specifying the jet-area definition:

- type: active area,

- ghost area: 0.005.

4.4.2 Background estimation and subtraction

The jet algorithm cannot distinguish jet fragments from particles produced in the underlying event. Therefore a basic correction of the reconstructed jet momentum is applied by subtracting the estimated fraction coming from the background processes. The mean density ρ of background contributing to the reconstructed jet momenta is estimated in each event from clusters reconstructed with the k_{t} algorithm, which starts the clustering with low-p_{T} tracks and is therefore suitable for determining the level of soft background present in a given event [109]. In each analysed event, k_{t} clusters are reconstructed from the hybrid tracks and two clusters with the highest p_{T} values are removed from the list in order to reduce the influence of true jets on the background estimation [109, 110]. The remaining clusters are sorted by the $p_{\mathrm{T}}^{\mathrm{jet}}/A_{\mathrm{jet}}$ ratio and the median value is taken for the ρ estimation [111]:

$$\rho = \mathrm{median}\left\{\frac{p_{\mathrm{T}}^{\mathrm{jet}}}{A_{\mathrm{jet}}}\right\}. \tag{4.9}$$

The calculation of the background density ρ is performed by a dedicated task `AliAnalysisTaskRho` in the EMCal framework.

For each signal jet in each event, the reconstructed jet momentum is corrected by subtracting the background contribution corresponding to the average background density ρ and the area of a given jet.

There are two ways of addressing the background subtraction: scalar and 4-vector subtraction [111]. In this analysis, the average background is subtracted using the scalar method, where the p_{T} component of jet momentum is corrected as:

$$p_{\mathrm{T,jet}}^{\mathrm{corrected}} = p_{\mathrm{T,jet}}^{\mathrm{measured}} - \rho A_{\mathrm{jet}} \tag{4.10}$$

while keeping the original jet direction, which is the standard approach to the subtraction of the underlying event in ALICE. Jets having negative p_{T} after the background subtraction are discarded.

An alternative method is using a 4-vector subtraction which allows for changing the orientation of the jet axis:

$$\boldsymbol{P}_{\mathrm{jet}}^{\mathrm{corrected}} = \boldsymbol{P}_{\mathrm{jet}}^{\mathrm{measured}} - \rho \boldsymbol{A}_{\mathrm{jet}}, \tag{4.11}$$

where $\boldsymbol{P}$ are 4-momenta and $\boldsymbol{A}_{\mathrm{jet}}$ is a 4-vector of jet area. This method is assumed to be convenient in cases when using large jet radii, for which the contamination from the background can generate a significant invariant mass [111].

4.4.3   Jet selection

Further constraints are imposed on the signal jets before they are used in association with V^0 particles.

A parameter D is used in the V^0–jet matching procedure as the maximum distance in $\eta \times \phi$ space between the jet axis and the momentum vector of a V^0 particle. Therefore, an acceptance cut on the jet pseudorapidity is applied in order to make sure that the jet cones of radius D cover the acceptance region of V^0 particles but do not jut out from it:

$$|\eta_{\text{jet,ch}}| < |\eta_{V^0}|^{\max} - D. \tag{4.12}$$

Additional cuts are used to suppress the contribution of purely combinatorial jets and hence to increase the probability of selecting a hard-scattering process. This includes imposing thresholds on jet p_T ($p_T^{\text{jet,ch}}$), on p_T of the leading constituent of the jet ($p_T^{\text{leading track}}$) and on jet area ($A_{\text{jet,ch}}$):

- p_T of the jet: $p_T^{\text{jet,ch}} > 5\,\text{GeV}/c$,

- p_T of the leading track in jet: $p_T^{\text{leading track}} > 5\,\text{GeV}/c$,

- jet area: $A_{\text{jet,ch}} > 0.6\pi R^2$.

Plots in Fig. 4.4 show the transverse-momentum spectrum of selected jets reconstructed with $R = 0.2$, distribution of the number of jets per event, pseudorapidity distribution and azimuth distribution of jets. The same distributions are plotted for $R = 0.3$ in Fig. 4.5. The dip in the η distribution is caused by the central membrane in the TPC at $\eta = 0$ which reduces the efficiency of reconstruction of tracks at mid-rapidity which is then propagated to the jet reconstruction.

4.5   Association of strange particles with jets

The association of particles with jets is done on a geometrical basis. For each selected V^0 candidate the angular distance d between its momentum vector and the axis of each selected jet in the event is calculated as following:

$$d = \sqrt{(\phi_{V^0} - \phi_{\text{jet}})^2 + (\eta_{V^0} - \eta_{\text{jet}})^2}. \tag{4.13}$$

If the distance between the V^0 candidate and the jet is smaller than the matching distance D, the candidate is considered to be inside the jet cone:

$$d < D. \tag{4.14}$$

Resulting sample of particles (hadrons, h) in the jet cones (JC) consists of particles produced in several processes:

- $N_h^{\text{UE,true prim.}}$: thermal production from background (primary particles from the underlying event),

- $N_h^{\text{UE,decay}}$: decays of (primary) background particles,
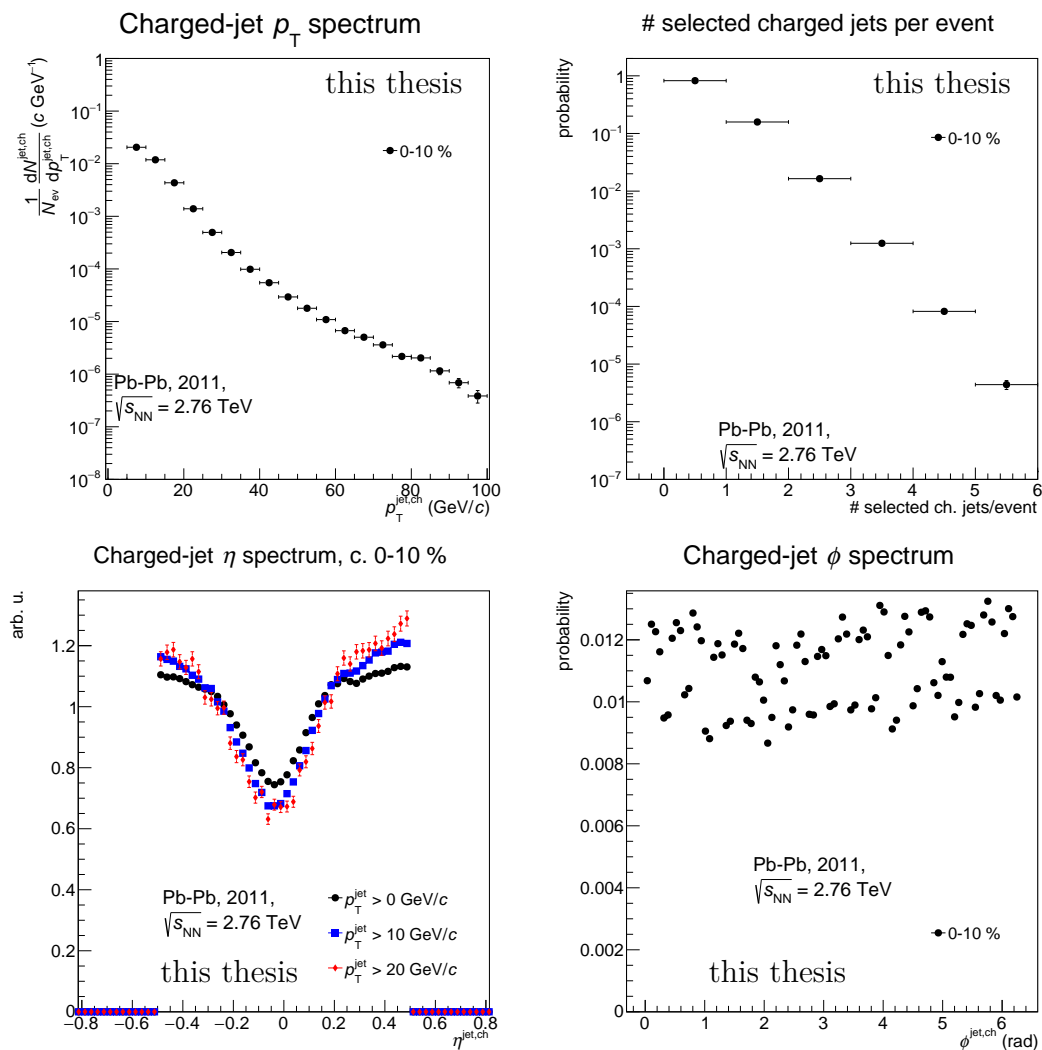
Figure 4.4: Spectrum of p_{T} (top left) of selected jets, distribution of the number of selected jets per event (top right) and distribution of η (bottom left) and ϕ (bottom right) of selected jets reconstructed with $R = 0.2$ in central (0–10 %) Pb–Pb collisions at $\sqrt{s_{\mathrm{NN}}} = 2.76\,\mathrm{TeV}$ from year 2011.
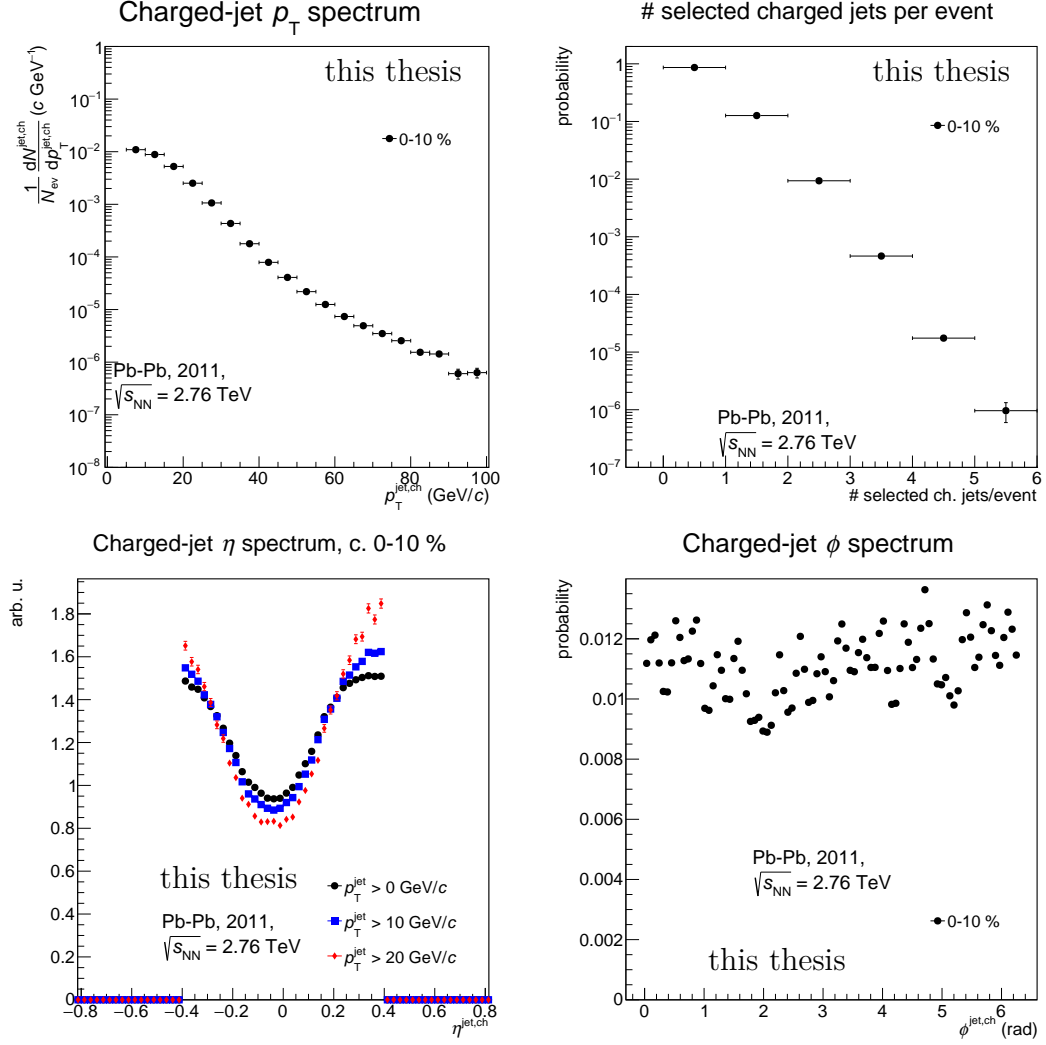
Figure 4.5: Spectrum of p_T (top left) of selected jets, distribution of the number of selected jets per event (top right) and distribution of η (bottom left) and ϕ (bottom right) of selected jets reconstructed with $R = 0.3$ in central (0–10 %) Pb–Pb collisions at $\sqrt{s_{NN}} = 2.76\,\mathrm{TeV}$ from year 2011.

- $\Xi^{0,-} \to \Lambda + \pi^{0,-}$ (weak decay, $\tau \approx 2 \times 10^{-10}\,\mathrm{s}$), considered in the corrections as the "feed-down" fraction f^{FD}

- $\Omega^- \to \Lambda + \mathrm{K}^-$ (weak decay, $\tau \approx 8 \times 10^{-11}\,\mathrm{s}$), assumed to be negligible

- $\Sigma^0 \to \Lambda + \gamma$ (electromagnetic decay, $\tau \approx 7 \times 10^{-20}\,\mathrm{s}$), considered to be primary

- $\Sigma^{*+,*0,*-} \to \Lambda + \pi^{+,0,-}$ (strong decay, $\tau \approx 2 \times 10^{-23}\,\mathrm{s}$), considered to be primary

- $\varphi(1020) \to \mathrm{K}_{\mathrm{S}}^0 + \mathrm{K}_{\mathrm{L}}^0$ (strong decay, $\tau \approx 2 \times 10^{-22}\,\mathrm{s}$), considered to be primary

- $N_{\mathrm{h}}^{\mathrm{jet,FF}}$: hadronization involving jet fragmentation,

- $N_{\mathrm{h}}^{\mathrm{jet,decay}}$: decays of jet constituents, not measured, estimated as the feed-down fraction in jets $f^{\mathrm{FD,jet}}$.

The raw yield of V^0 particles found in jet cones ($N_{\mathrm{h}}^{\mathrm{JC}}$) is the sum of all contributions, decreased by the efficiency of reconstructing V^0s in jet cones ($\epsilon_{\mathrm{h}}^{\mathrm{JC}}$):

$$N_{\mathrm{h}}^{\mathrm{JC}} = \epsilon_{\mathrm{h}}^{\mathrm{JC}}(N_{\mathrm{h}}^{\mathrm{jet,FF}} + N_{\mathrm{h}}^{\mathrm{jet,decay}} + N_{\mathrm{h}}^{\mathrm{UE,true\ prim.}} + N_{\mathrm{h}}^{\mathrm{UE,decay}}). \tag{4.15}$$

Products of strong and electromagnetic decays (Σ, φ) are included in the definition of primary particles:

$$N_{\Lambda}^{\mathrm{UE,prim.}} = N_{\Lambda}^{\mathrm{UE,true\ prim.}} + N_{\Lambda}^{\mathrm{UE,\Sigma \to \Lambda}}, \qquad N_{\mathrm{K}_{\mathrm{S}}^0}^{\mathrm{UE,prim.}} = N_{\mathrm{K}_{\mathrm{S}}^0}^{\mathrm{UE,true\ prim.}} + N_{\mathrm{K}_{\mathrm{S}}^0}^{\mathrm{UE,\varphi \to \mathrm{K}_{\mathrm{S}}^0}}. \tag{4.16}$$

Yield of Λ coming from decays of jet constituents ($N_{\Lambda}^{\mathrm{jet,decay}}$) is considered to consist only of the contribution of Ξ decays:

$$N_{\Lambda}^{\mathrm{jet,decay}} = N_{\Lambda}^{\mathrm{jet,\Xi \to \Lambda}} + N_{\Lambda}^{\mathrm{jet,\Omega \to \Lambda}} \approx N_{\Lambda}^{\mathrm{jet,\Xi \to \Lambda}}. \tag{4.17}$$

Yield of Λ coming from decays of background particles ($N_{\Lambda}^{\mathrm{UE,decay}}$) is considered to consist only of the contribution of Ξ decays:

$$N_{\Lambda}^{\mathrm{UE,decay}} = N_{\Lambda}^{\mathrm{UE,\Xi \to \Lambda}} + N_{\Lambda}^{\mathrm{UE,\Omega \to \Lambda}} \approx N_{\Lambda}^{\mathrm{UE,\Xi \to \Lambda}}. \tag{4.18}$$

Finally, the yield of V^0s from the underlying event is considered to consist of the following components:

$$N_{\mathrm{K}_{\mathrm{S}}^0}^{\mathrm{UE}} = N_{\mathrm{K}_{\mathrm{S}}^0}^{\mathrm{UE,prim.}}, \qquad N_{\Lambda}^{\mathrm{UE}} = N_{\Lambda}^{\mathrm{UE,prim.}} + N_{\Lambda}^{\mathrm{UE,\Xi \to \Lambda}}. \tag{4.19}$$

A hard scattering process is selected by imposing a cut on the minimum reconstructed $p_{\mathrm{T}}^{\mathrm{jet,ch}}$ in order to maximize statistics. Spectra of strange particles in charged jets are studied for two thresholds of jet momentum: $p_{\mathrm{T}}^{\mathrm{jet,ch}} > 10\,\mathrm{GeV}/c$ and $p_{\mathrm{T}}^{\mathrm{jet,ch}} > 20\,\mathrm{GeV}/c$. Uncorrected (raw) spectra of V^0 particles in jet cones are shown for $R = D = 0.2$ in Fig. 4.6 and for $R = D = 0.3$ in Fig. 4.7.
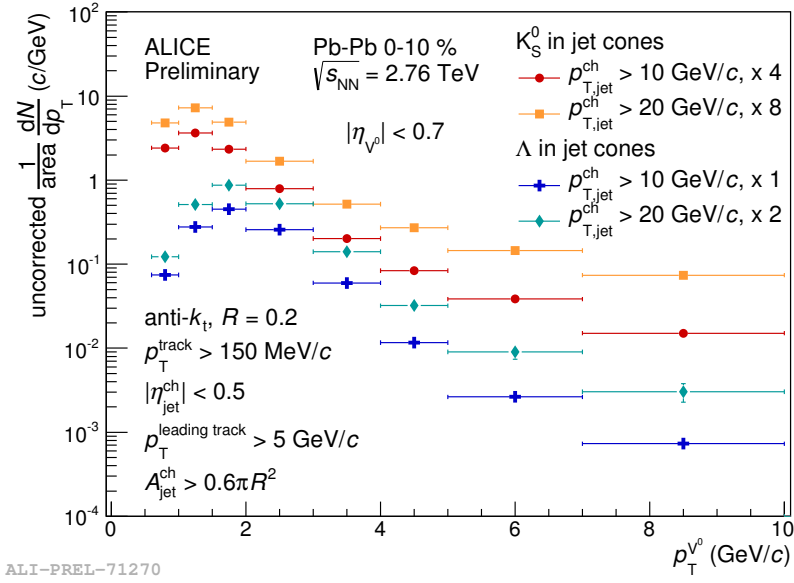
Figure 4.6: Spectra of V^0 particles in jet cones for $R = D = 0.2$ in central (0–10 %) Pb–Pb collisions at $\sqrt{s_{\mathrm{NN}}} = 2.76$ TeV from year 2011.
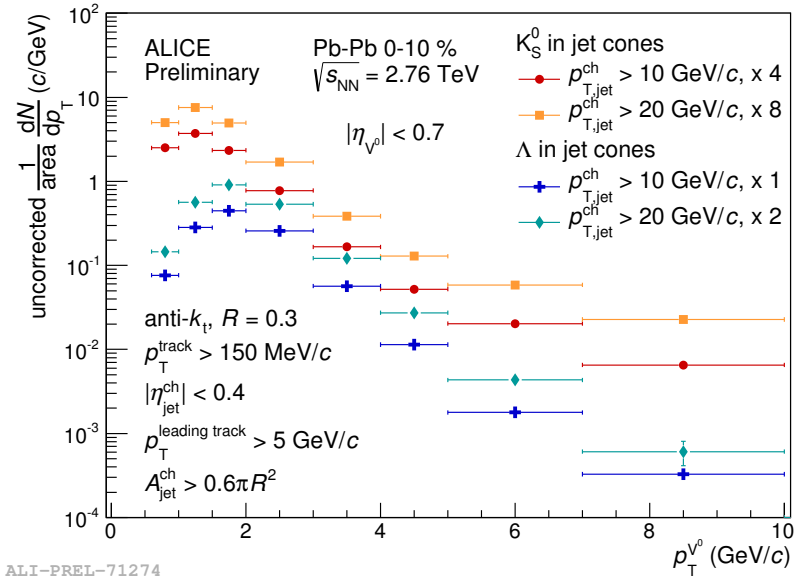
Figure 4.7: Spectra of V^0 particles in jet cones for $R = D = 0.3$ in central (0–10 %) Pb–Pb collisions at $\sqrt{s_{\mathrm{NN}}} = 2.76$ TeV from year 2011.

4.6 Corrections

V^0 particles collected within jet cones originate not only from jet fragmentation but also from the underlying event. Yield of V^0s in jet cones coming from the underlying event (N_h^{UE}) is estimated separately outside jet cones with several methods in event regions where only a production from background processes is expected ($N_h'^{UE}$) (see Sec. 4.6.2).

Yields in jet cones and in UE are first normalized and corrected with their respective efficiencies (see Sec. 4.6.1). The spectrum of V^0s in UE is then subtracted from the spectrum of V^0s in jet cones. For Λ particles, the resulting spectrum is assumed to be the sum of the spectrum of particles from jet fragmentation and the spectrum of particles from decays of jet constituents:

$$N_h^{jet} = N_h^{jet,FF} + N_h^{jet,decay}. \tag{4.20}$$

The relative contribution of particles from decays is estimated by the "feed-down" fraction $f_h^{FD,jet}$ and subtracted (see Sec. 4.6.3):

$$f_h^{FD,jet} \overset{\text{def}}{=} \frac{N_h^{jet,decay}}{N_h^{jet}}. \tag{4.21}$$

All these steps are summarized in the complete formula for obtaining corrected spectra of strange particles associated with jet production:

$$N_h^{jet,FF,norm.} = \left(\frac{N_h^{JC}}{\mathcal{N}_h^{JC,norm.} \epsilon_h^{JC}} - \frac{N_h'^{UE}}{\mathcal{N}_h^{UE,norm.} \epsilon_h^{UE}} \right) \left(1 - f_h^{FD,jet} \right), \tag{4.22}$$

where $\mathcal{N}$ are normalization factors.

Spectra are obtained as functions of particle transverse momentum $p_T^{V^0}$, jet transverse momentum $p_T^{jet,ch}$, jet resolution parameter R, matching distance D and centrality.

Yields are normalized so that the final spectrum represents the yield per unit of acceptance in $\eta \times \phi$ space, i.e. in case of spectra in jet cones, the normalization factor is the total area of all jet cones: $\mathcal{N}_h^{JC,norm.} = N_{jet} \pi D^2$. The normalization of the spectra of V^0s in UE depends on a given method (see Sec. 4.6.2).

4.6.1 Reconstruction efficiency of V^0 particles

The spectra of V^0 particles are corrected for the reconstruction efficiency obtained with Pb–Pb events generated in a Monte Carlo (MC) simulation, taking into account all conditions that affected the real data. The MC generated events undergo a full detector simulation under realistic conditions and are reconstructed with the same procedure that is used for the real data. The particle reconstruction efficiency takes into account the limited detector acceptance and the branching ratio for the particle decay channels, that are used for the V^0 reconstruction. Reconstruction efficiency is defined as the ratio of the number of particles that were successfully reconstructed in the region of interest ("associated particles") to the number of particles generated in the region of interest ("generated particles").

Dependences of the efficiency on transverse momentum ($p_{\mathrm{T,gen.}}^{\mathrm{h}}$), pseudorapidity ($\eta_{\mathrm{gen.}}^{\mathrm{h}}$) and centrality (c.) are considered.

$$\epsilon_{\mathrm{h}}(p_{\mathrm{T,gen.}}^{\mathrm{h}}, \eta_{\mathrm{gen.}}^{\mathrm{h}}, \mathrm{c.}) = \frac{N_{\mathrm{h}}^{\mathrm{associated}}(\ldots)}{N_{\mathrm{h}}^{\mathrm{generated}}(\ldots)} \tag{4.23}$$

A reconstructed V^0 particle is considered to be associated if it fulfils the following criteria.

- The V^0 candidate and its daughter tracks passed all selection criteria (at the reconstructed level).

- The MC daughter particles have the same MC mother particle.

- The MC particles (mother and daughters) have correct identities (checked using their PDG code).

- The MC mother particle is primary-like, (i.e. the (3D) distance between the production point of the MC mother particle and the primary vertex is less than $0.01\,\mathrm{cm}$).

- The MC particle was produced in the region of interest, (i.e. $|\eta_{\mathrm{gen.}}^{\mathrm{h}}| < |\eta_{\mathrm{V}^0}|^{\mathrm{max}}$).

- The MC particle contributes to the signal, (i.e. its reconstructed invariant mass falls within the region of signal extraction).

An MC particle is considered to be a generated V^0 particle if it fulfils the following criteria.

- The MC particle has a correct identity (checked using their PDG code).

- The MC particle is primary-like.

- The MC particle was produced in the region of interest, (i.e. $|\eta_{\mathrm{gen.}}^{\mathrm{h}}| < |\eta_{\mathrm{V}^0}|^{\mathrm{max}}$).

The reconstruction efficiency of inclusive particles as a function of $p_{\mathrm{T}}^{\mathrm{V}^0}$ is plotted for both particle species in Fig. 4.8.

The reconstruction efficiency has a strong dependence on pseudorapidity at low $p_{\mathrm{T}}^{\mathrm{V}^0}$, which is more pronounced for kaons, and becomes more uniform at larger $p_{\mathrm{T}}^{\mathrm{V}^0}$, as can be seen in Fig. 4.9.

Correction of efficiency calculation

When estimating the reconstruction efficiency for particles in jets, a question arises whether the efficiency of reconstructing a V^0 particle inside a jet cone is different from the efficiency estimated for inclusive particles, for example because of larger track density in jet cones. In order to verify that, jets were reconstructed from tracks in the simulated data and the reconstruction efficiency was evaluated for particles inside the jet cones. Efficiency of particles in jet cones is compared with the inclusive efficiency as a function of $p_{\mathrm{T}}^{\mathrm{V}^0}$ and η_{V^0} in Fig. 4.10. Based on the ratio, it was concluded that the reconstruction efficiency of V^0 particles in
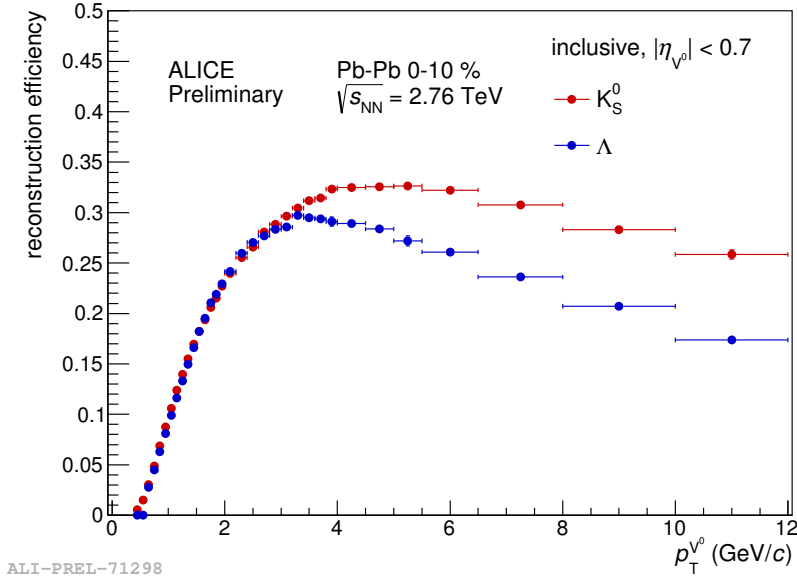
Figure 4.8: Reconstruction efficiency of inclusive K_S^0 and Λ in central (0–10 %) Pb–Pb collisions at $\sqrt{s_{NN}} = 2.76$ TeV from year 2011.
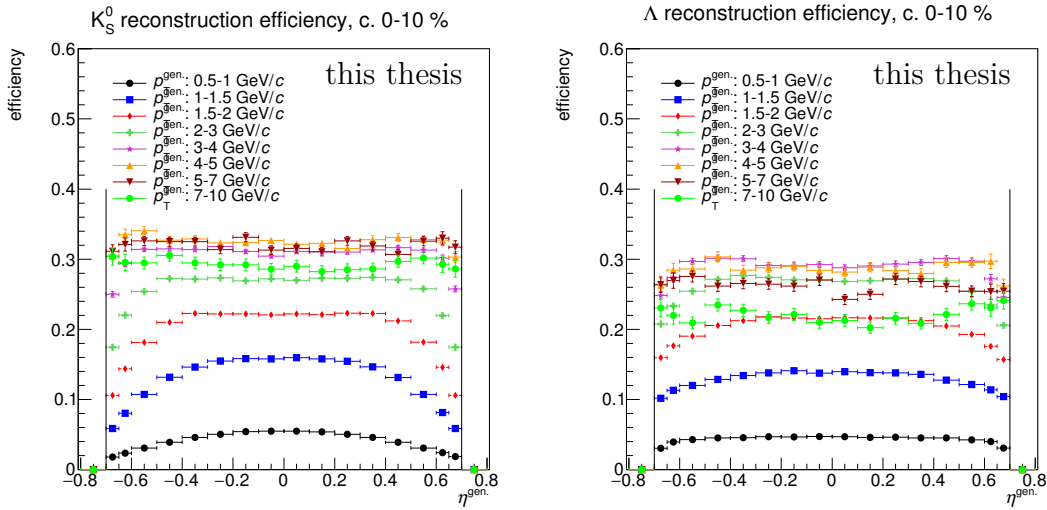
Figure 4.9: Reconstruction efficiency of inclusive K_S^0 and Λ as a function of $p_T^{V^0}$ and η_{V^0} in central (0–10 %) Pb–Pb collisions at $\sqrt{s_{NN}} = 2.76$ TeV from year 2011.
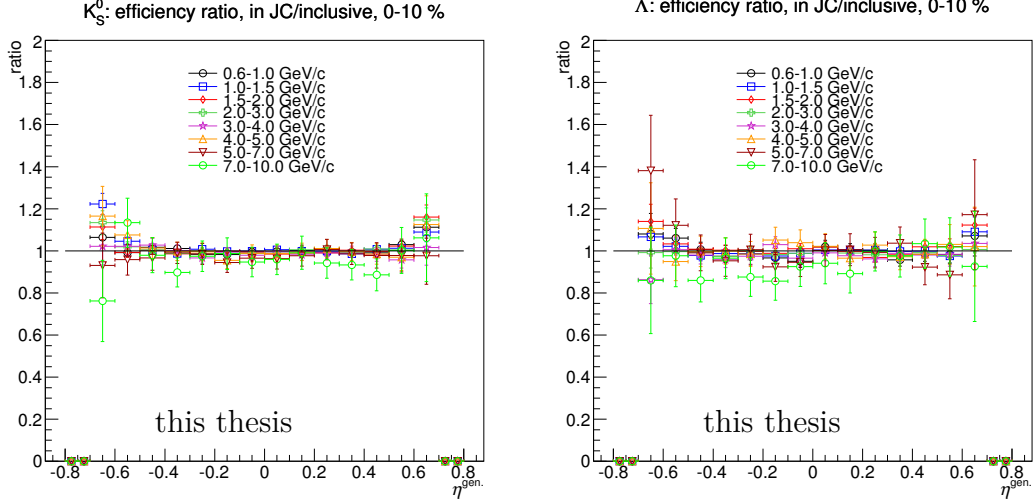
Figure 4.10: Ratio of the reconstruction efficiency of K_S^0 and Λ in jet cones to the inclusive efficiency as a function of $p_T^{V^0}$ and η_{V^0} in central (0–10 %) Pb–Pb collisions at $\sqrt{s_{NN}} = 2.76 \, \text{TeV}$ from year 2011.

jet cones is within statistical uncertainties of the simulation consistent with the efficiency obtained for inclusive particles.

Since statistics available for V^0 particles in jet cones in real data was not sufficient to preform full two-dimensional signal extraction in $p_T^{V^0}$–η_{V^0} bins, the efficiency correction had to be applied only as a function of $p_T^{V^0}$. However, the η_{V^0} distributions of inclusive associated V^0 particles (in individual $p_T^{V^0}$ bins) in MC have shapes different from the corresponding η_{V^0} distributions of V^0 particles in real jet cones (and in UE). This is a consequence of selecting particles under the constraint imposed by the η distribution of jets. Shape of the resulting η_{V^0} distribution particles in jet cones is then given by the convolution of the distribution of inclusive V^0 particles and the distribution of selected jets, where the distance D also enters the convolution. Therefore, when calculating the efficiency of V^0s in JC as a function of $p_T^{V^0}$ only, yields of simulated V^0s in individual η_{V^0} bins should then contribute to the averaged efficiency with relative weights determined by the shape of the η_{V^0} distribution of particles in real data.

Here is the summary of the facts that had to be taken into account:

- The reconstruction efficiency of V^0s depends on $p_T^{V^0}$ and η_{V^0}.

- The local efficiency (in $p_T^{V^0}$–η_{V^0} bins) of V^0s in JC and UE is the same as the efficiency of inclusive V^0s.

- Shapes of $p_T^{V^0}$–η_{V^0} distributions of associated V^0s in MC are different from shapes of raw distributions of V^0s measured in JC and UE.

- Due to low statistics available for V^0s in JC and UE in real data and for inclusive V^0s in MC, the efficiency correction cannot be applied in $p_T^{V^0}$–η_{V^0} bins.

Therefore rescaling of MC yields is needed. The rescaling procedure consists of the following steps.

- Get the uncorrected distribution of V^0s measured in JC or UE $m(\eta_{V^0}, p_T^{V^0})$.

  Assume that the signal purity of inclusive V^0s ($P_{\text{inclusive}}(p_T^{V^0}, \eta_{V^0})$) is the same as for V^0s in JC and UE and use it to extract signal m from the candidate distribution m_{raw}:

  $$m(p_T^{V^0}, \eta_{V^0}) = m_{\text{raw}}(p_T^{V^0}, \eta_{V^0})|_{\text{peak region}} \cdot P_{\text{inclusive}}(p_T^{V^0}, \eta_{V^0})|_{\text{peak region}}. \quad (4.24)$$

- Declare the measured distribution to be identical to that of associated V^0s:

  $$a(\eta_{V^0}, p_T^{V^0}) \equiv m(\eta_{V^0}, p_T^{V^0}). \quad (4.25)$$

  Do not propagate the statistical uncertainty of the measured yield:

  $$\sigma_a \equiv 0. \quad (4.26)$$

- Take the distribution of the efficiency of inclusive V^0s: $\epsilon(\eta_{V^0}, p_T^{V^0})$.

- Calculate the yield of generated V^0s in JC or UE using the efficiency of inclusive V^0s:

  $$g(\eta_{V^0}, p_T^{V^0}) = a(\eta_{V^0}, p_T^{V^0})/\epsilon(\eta_{V^0}, p_T^{V^0}). \quad (4.27)$$

The resulting distributions of associated and generated particles have the following properties.

- Local efficiency of V^0s in JC or UE is the same as for inclusive V^0s.

- Shape of associated V^0s in η_{V^0} is the same as for V^0s measured in JC or UE.

- Yields can be summed up over η_{V^0} bins in the efficiency calculation.

  The rescaled efficiency ϵ_{rs} can be obtained as:

  $$\epsilon_{\text{rs}}(p_T^{V^0}) = \frac{a(p_T^{V^0})}{g(p_T^{V^0})} = \frac{\sum_i a(\eta_{V^0 i}, p_T^{V^0})}{\sum_j g(\eta_{V^0 j}, p_T^{V^0})} = \frac{\sum_i m(\eta_{V^0 i}, p_T^{V^0})}{\sum_j m(\eta_{V^0 j}, p_T^{V^0})/\epsilon(\eta_{V^0 j}, p_T^{V^0})}. \quad (4.28)$$

- The efficiency correction can then be applied as a function of $p_T^{V^0}$ to get corrected spectra t of V^0s in JC and UE:

  $$t(p_T^{V^0}) = m(p_T^{V^0})/\epsilon_{\text{rs}}(p_T^{V^0}). \quad (4.29)$$

4.6.2 Subtraction of particles in the underlying event

Multiple methods are used to estimate the p_T spectra of particles in the underlying event (N_h^{UE}). V^0 particles are collected in regions where the jet production should have negligible effect and all V^0 particles are expected to be produced by background processes.

The following overview specifies for each method which sample of events is used, in which regions of the event are the particles collected and how is calculated the corresponding normalization factor.

- no-jet events (NJ)

    - in events where no jet was selected
    - in the entire $\eta_{V^0} \times \phi_{V^0}$ acceptance
    - $\mathcal{N}_h^{\text{NJ,norm.}} = N_{\text{no-jet event}} \times 2\pi \times 2|\eta_{V^0}|^{\max}$

- outside cones (OC)

    - in events with selected jet(s)
    - in area which remains after excluding a cone of radius $2D$ around each selected jet from the acceptance
    - $\mathcal{N}_h^{\text{OC,norm.}} = N_{\text{jet event}} \times 4\pi|\eta_{V^0}|^{\max} - \sum_{\text{jet}} \left(4\pi D^2 - (\text{area over } |\eta_{V^0}|^{\max})\right)$

- perpendicular cones (PC)

    - in events with selected jet(s)
    - in 2 cones of radius D for each selected jet
    - $\eta_{\text{PC}} = \eta_{\text{jet}}, \qquad \phi_{\text{PC}} = \phi_{\text{jet}} \pm \pi/2, \qquad p_{\text{T}}^{\text{PC}} = p_{\text{T}}^{\text{jet}}$
    - $\mathcal{N}_h^{\text{PC,norm.}} = N_{\text{cone}}^{\text{PC}} \pi D^2$

- random cones (RC)

    - in events with selected jet(s)
    - in 1 cone (or none) of radius D in each event with selected jet(s)
    - uniform random ϕ_{RC} and η_{RC}: $\phi_{\text{RC}} \in [0, 2\pi], \qquad |\eta_{\text{RC}}| < |\eta_{\text{jet}}|^{\max}$
    - cone does not overlap with any selected jet
    - $\mathcal{N}_h^{\text{RC,norm.}} = N_{\text{cone}}^{\text{RC}} \pi D^2$

- median-cluster cones (MCC)

    - in events with selected jet(s)
    - in 1 cone (or none) of radius D in each event with selected jet(s)
    - $|\eta_{\text{MCC}}| < |\eta_{\text{jet}}|^{\max}$
    - median cluster in the list of k_{t} jets sorted by $p_{\text{T}}^{\text{jet}}/A_{\text{jet}}$ and with the two first clusters excluded (see ρ calculation in Sec. 4.4.2)
    - $\mathcal{N}_h^{\text{MCC,norm.}} = N_{\text{cone}}^{\text{MCC}} \pi D^2$

The spectra of V^0s in NJ are used as the default method since they represent more than $80\,\%$ of accepted events (see Fig. 4.4) and thus provide the largest statistics for the UE estimation.

Uncorrected spectra obtained with different methods are compared in Fig. 4.11 for K_S^0 and in Fig. 4.12 for Λ. Agreement between different methods is better than $10\,\%$ in the $p_{\text{T}}^{V^0}$ interval 2–4 GeV/c for both particle species and remains approximately the same after applying the efficiency correction. Differences between methods are considered for the systematic uncertainty of the estimation of spectra of V^0 particles in the UE.
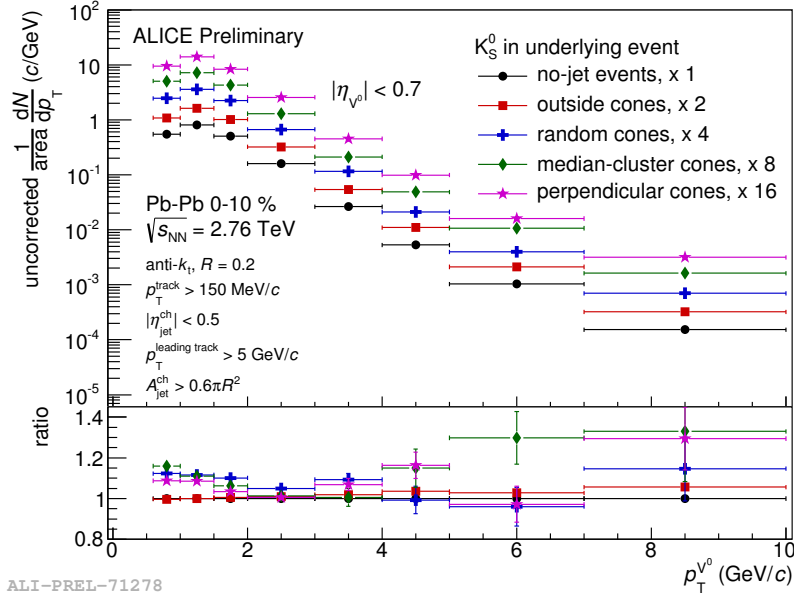
Figure 4.11: Uncorrected spectra of K_S^0 in the underlying event for jets with resolution $R = 0.2$ in central (0–10 %) Pb–Pb collisions at $\sqrt{s_{NN}} = 2.76$ TeV from year 2011.
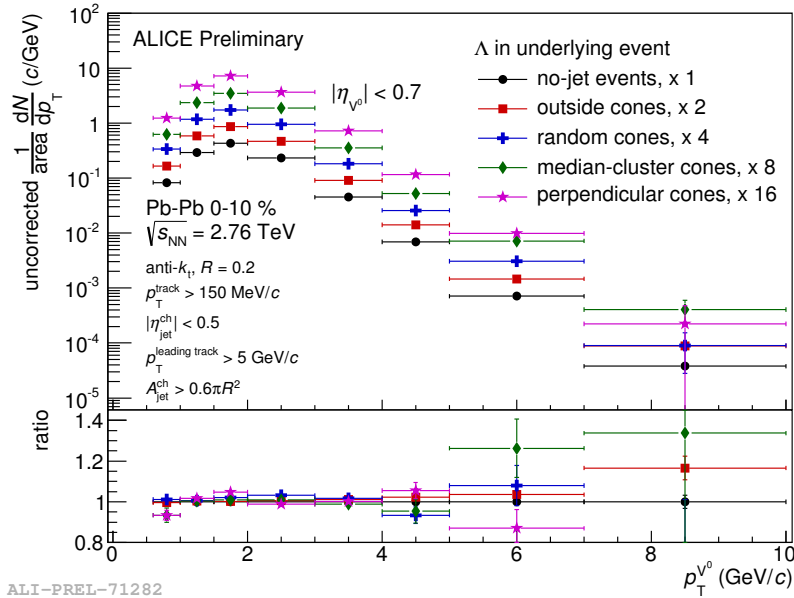
Figure 4.12: Uncorrected spectra of Λ in the underlying event for jets with resolution $R = 0.2$ in central (0–10 %) Pb–Pb collisions at $\sqrt{s_{NN}} = 2.76$ TeV from year 2011.

70

4.6.3 Subtraction of decay products ("feed-down")

Inclusive particles

Estimation method by the authors of the published paper [64, 89] on inclusive analysis of K_S^0 and Λ is used for determining the feed-down fraction of inclusive particles.

$$N_{\Xi^{0,-}\to\Lambda}^{\text{real,inclusive,raw}}(p_T^\Lambda, \text{c.}) = \sum_{p_T^\Xi} N_{\Xi^{0,-}\to\Lambda}^{\text{MC,inclusive}}(p_T^\Lambda, p_T^\Xi, \text{c.}) \frac{N_{\Xi^-}^{\text{real,inclusive}}(p_T^\Xi, \text{c.})}{N_{\Xi^-}^{\text{MC,inclusive}}(p_T^\Xi, \text{c.})}, \quad (4.30)$$

where $N_{\Xi^-}^{\text{real,inclusive}}$ is the measured (real) spectrum of inclusive Ξ^- in $|y| < 0.5$, normalized per number of real events [112, 113], $N_{\Xi^-}^{\text{MC,inclusive}}$ is the spectrum of inclusive Ξ^- in $|y| < 0.5$ generated in the MC production (used for the feed-down estimation), normalized per number of MC events, $N_{\Xi^{0,-}\to\Lambda}^{\text{MC,inclusive}}$ is the distribution of p_T of reconstructed inclusive Λ particles and of p_T of their $\Xi^{0,-}$ mother particles, normalized per number of MC events, $N_{\Xi^{0,-}\to\Lambda}^{\text{real,inclusive,raw}}$ is the uncorrected spectrum of inclusive Λ from decays of $\Xi^{0,-}$, normalized per number of real events, corresponding to the data where $N_{\Xi^-}^{\text{real,inclusive}}$ was measured.

The feed-down fraction is given by the ratio:

$$f_\Lambda^{\text{FD,inclusive}}(p_T^\Lambda, \text{c.}) = \frac{N_{\Xi^{0,-}\to\Lambda}^{\text{real,inclusive,raw}}(p_T^\Lambda, \text{c.})}{N_\Lambda^{\text{real,inclusive,raw}}(p_T^\Lambda, \text{c.})}, \quad (4.31)$$

where $N_\Lambda^{\text{real,inclusive,raw}}$ is the uncorrected measured spectrum of inclusive Λ particles, normalized per number of real events.

Since spectra of Ξ have been measured only for $p_T^\Xi < 8\,\text{GeV}/c$, the feed-down fraction is assumed to be constant for $p_T^\Lambda > 7\,\text{GeV}/c$.

Particles in the underlying event

The feed-down fraction of particles in the underlying event may be estimated as being the same as for the inclusive particles since particles produced in jets represent just a small fraction of the total sample of inclusive particles. This estimation is needed only for reporting fully corrected spectra of V^0s in the underlying event. When used for correction of the spectra of V^0s in jet cones, the spectra of V^0s in UE are supposed to contain the contribution from decays which is subtracted as well.

Particles in jets

The spectra of particles in jet cones after the subtraction of the underlying event still contain a contamination from decays of jet constituents. The corresponding fraction is subtracted by applying a correction for feed-down from decays of Ξ^0 and Ξ^- baryons ($\Xi^{0,-}$) in jets into Λ baryons in jets.

In order to evaluate which fraction of measured Λ particles in jets is originating from decays of Ξ particles in jets, one would need measured p_T spectra of these mother particles. Since no such measurement is available for particles in jets, the feed-down correction factors have to be estimated using several assumptions.

The following two estimation scenarios are considered:

1. Feed-down fraction is the same as for inclusive particles.

2. Feed-down fraction is the same as for particles in jets in p–p collisions.

In case of considering the feed-down of inclusive particles, the feed-down fraction as defined above can be directly used in the Eq. (4.22) even though it is applied on spectrum after efficiency correction since (under the assumption of this scenario) it holds:

$$f_\Lambda^{\mathrm{FD,jet}} = \frac{N_{\Xi^{0,-}\to\Lambda}^{\mathrm{real,jet}}}{N_\Lambda^{\mathrm{real,jet}}} = \frac{N_{\Xi^{0,-}\to\Lambda}^{\mathrm{real,jet,raw}}}{N_\Lambda^{\mathrm{real,jet,raw}}} = \frac{N_{\Xi^{0,-}\to\Lambda}^{\mathrm{real,inclusive,raw}}}{N_\Lambda^{\mathrm{real,inclusive,raw}}} = f_\Lambda^{\mathrm{FD,inclusive}}. \qquad (4.32)$$

The second scenario is used for estimating the related systematic uncertainty. The feed-down of Λ particles in jets in Pb–Pb collisions may be underestimated with the feed-down obtained in PYTHIA jets. I use spectra of hyperons in jets in simulated p–p collisions at $\sqrt{s} = 2.76\,\mathrm{TeV}$ generated by PYTHIA 8, tune 4C [100, 101]. Charged jets were reconstructed using resolution $R = 0.2, 0.3$ and the same selection settings as described in Sec. 4.4. Generated Λ particles were associated with jets using $D = R$ and the feed-down fraction was calculated for Λ and $\overline{\Lambda}$ together according to the definition in Eq. (4.21). The resulting fraction as a function of $p_{\mathrm{T}}^{\mathrm{V0}}$ was then fitted with a constant in the range $p_{\mathrm{T}}^{\mathrm{V0}}/(\mathrm{GeV}/c) \in [2, 12]$, giving the resulting feed-down fraction in PYTHIA jets:

$$f_\Lambda^{\mathrm{FD,jet}} = 0.142. \qquad (4.33)$$

Results of both estimation methods are compared in Fig. 4.13. The feed-down fraction of inclusive is significantly higher than the PYTHIA result only for $p_{\mathrm{T}}^{\mathrm{V0}} < 4\,\mathrm{GeV}/c$. The fraction obtained for PYTHIA jets does not seem to depend neither on $p_{\mathrm{T}}^{\mathrm{V0}}$ nor on the jet resolution R.

Fig. 4.14 shows the result of the feed-down fraction in PYTHIA jets obtained with larger statistics, compared with the ratio of simulated inclusive particles and particles outside jet cones. Depending on the range of $p_{\mathrm{T}}^{\mathrm{hard}}$, the feed-down fraction estimated with the constant fit takes values between 0.1442 and 0.1458.

The feed-down fraction calculated for inclusive particles is used for the final results. The systematic uncertainty is estimated with considering the fraction obtained with PYTHIA simulation.

4.6.4   Correction of jet momenta

The reconstructed transverse momentum of a (measured) jet is affected by several effects. First effect is the detector response, given by the efficiency of the single-track reconstruction and by the momentum resolution. Second source is the contamination by particles from the underlying event.

The latter is partially removed by the subtraction of the average background density on an event-by-event basis. However, the background density in a given event is not isotropic. Furthermore, the calculation of the jet area, and consequently the calculation of ρ as well, suffers from numerical fluctuations. Both are usually accumulated in a δp_{T} distribution [109] which describes the smearing of jet momenta and is used for the unfolding of jet spectra. In order to apply an unfolding procedure sufficient statistics is required.
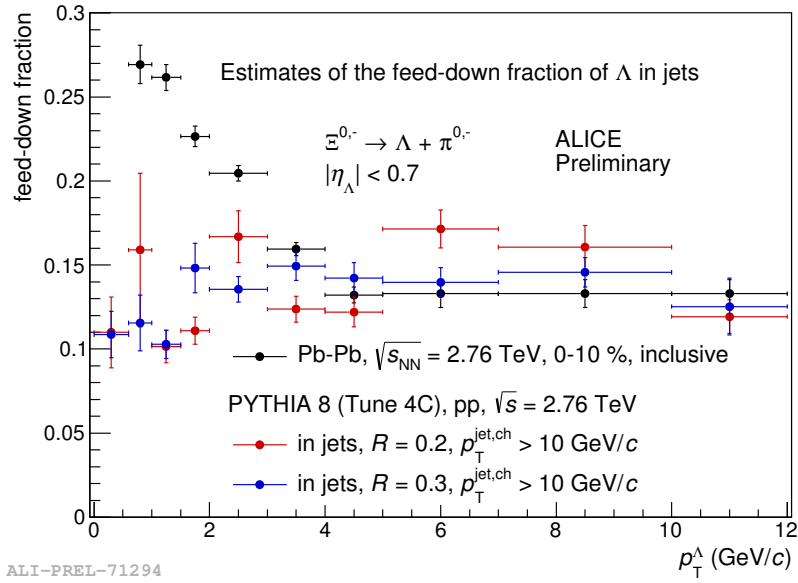
Figure 4.13: Feed-down fraction estimated for Λ in jets using inclusive particles in central (0–10 %) Pb–Pb collisions at $\sqrt{s_{NN}} = 2.76$ TeV from year 2011 and particles in simulated p–p collisions in jets for $R = 0.2, 0.3$.
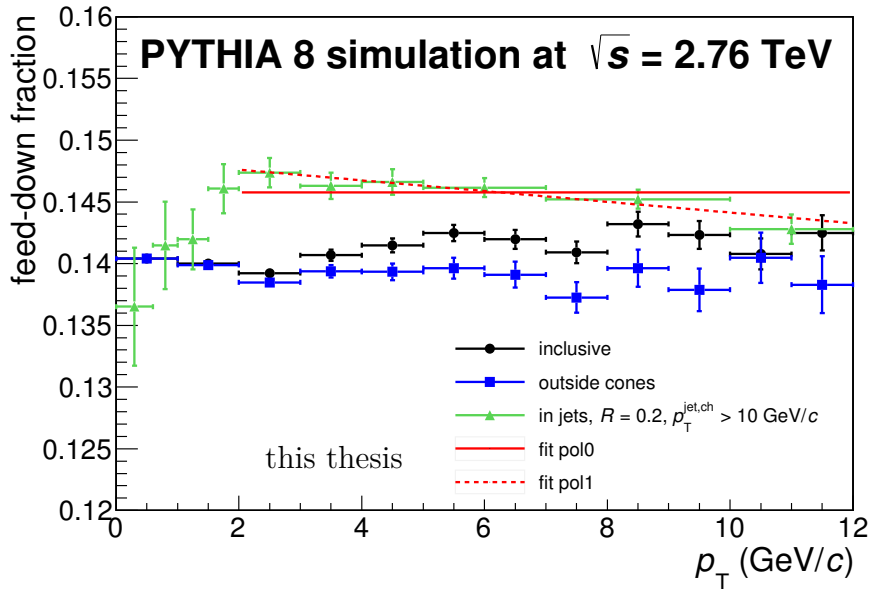
Figure 4.14: Feed-down fraction of Λ in jets in events generated by PYTHIA 8, compared with the fraction of inclusive particles and particles outside jet cones.

For this analysis, the measured subjects are particles associated with jets, i.e. pairs of objects. This gives rise to an entanglement between the measured $p_T^{\text{jet,ch}}$ and the $p_T^{V^0}$ of particles associated with jets. In order to correct such distribution for the aforementioned effects a full two-dimensional unfolding would be appropriate if the accumulated statistics was sufficient.

Correction for the detector response might be applied using a bin-by-bin correction (BBB) where the bins of spectra of V^0 particles in JC are scaled by correction factors compensating for the shift of momenta of the associated jets. The bin-by-bin correction factors (BBB-CF), obtained from K_S^0 candidates in simulated data for p–p collisions at $\sqrt{s} = 2.76\,\text{TeV}$, are defined as:

$$\text{BBB-CF}(p_T^{V^0}, p_T^{\text{jet}}) = \frac{N_{K_S^0}^{\text{JC,gen.}}\left(p_T^{V^0}, p_T^{\text{jet,particle level}}\right)}{N_{K_S^0}^{\text{JC,ass.}}\left(p_T^{V^0}, p_T^{\text{jet,detector level}}\right)}. \tag{4.34}$$

No δp_T smearing is considered in this BBB-CF study. The correction factors resulting from the PYTHIA study, performed by Alice Zimmermann, are presented for K_S^0 and both $p_T^{\text{jet,ch}}$ thresholds in Fig. 4.15. The BBB-CF behave as the inverse of the V^0 reconstruction efficiency $\epsilon(p_T^{V^0})$ at $p_T^{V^0} < 10\,\text{GeV}/c$ and they drop further at higher $p_T^{V^0}$ to correct for the decreasing p_T^{jet} resolution. Therefore, in the context of this analysis, it is sufficient to only correct for the reconstruction efficiency as applying the bin-by-bin correction is not necessary.
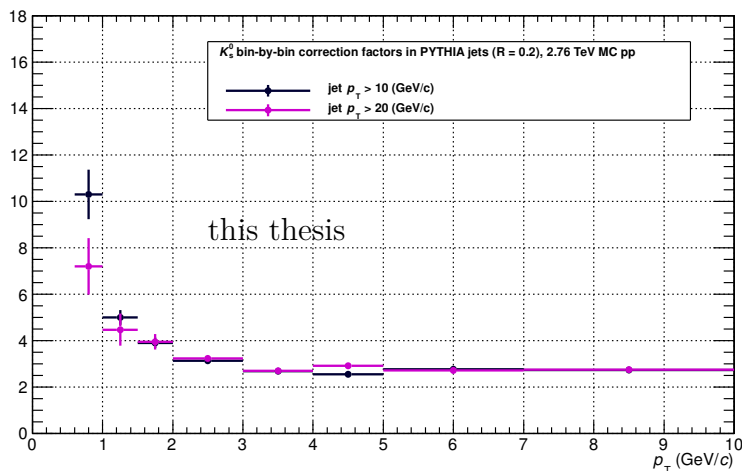
Figure 4.15: Bin-by-bin correction factors derived from PYTHIA jets to study the detector response. (Analysis performed by Alice Zimmermann.)

4.6.5 Correction for fluctuations of the underlying event

In order to estimate the impact of the background fluctuations on the baryon-to-meson ratio in jets in Pb–Pb collisions, the following study involving embedding of simulated jets into real events has been carried out by Alice Zimmermann.

For each selected event in real data, a random event that contains at least one jet that passes the selection criteria of the analysis is picked up from the sample of simulated p–p events generated by PYTHIA 8. The whole PYTHIA

event, including all tracks, is merged with the real data. Jet reconstruction is then performed again using the merged events as input. Jets reconstructed in merged events and generated PYTHIA jets are matched by requiring the distance between them in $\eta \times \phi$ space to be less than $0.75R$ and the p_T carried by generated particles contained in both jets to be at least half of the total p_T of the PYTHIA jet. The spectrum of V^0 particles in the UE in merged events is obtained using only cones of jets matched with PYTHIA jets and only V^0s from real data. The resulting spectrum of V^0s in the UE is divided by the spectrum used for the UE subtraction in the analysis (i.e. V^0s in no-jet events). The ratio of spectra gives the correction factor to be applied to the UE subtraction. The two spectra and their ratio can be seen in Fig. 4.16. Because of large statistical uncertainties, only the first p_T bin (2–$3\,\mathrm{GeV}/c$) is considered and the same correction factor is used for the other p_T bins. The corrected spectrum of V^0s in the UE is then subtracted from the spectrum of particles in jet cones. The effect of applying the correction factor on the spectra after the UE subtraction is plotted in Fig. 4.17.

Several variations are evaluated in order to estimate the systematic uncertainty related to the correction factor. A possible p_T dependence of the correction factor is taken into account by fitting the ratio of spectra with a linear function. Since the spectra of V^0 particles in cones of PYTHIA jets might contain a small contamination from actual jets, the embedding is repeated using only no-jet events. In order to consider the distribution of jets with respect to the event plane, the jet embedding is modified using the measured azimuthal anisotropy (v_2) of jets.

4.6.6 Contamination of jet constituents

This analysis is focused on measurement of spectra of neutral particles produced in association with charged jets. That means that the neutral particles are excluded from the jet definition and thus do not contribute to the jet momentum. However, some of the charged daughter particles of studied V^0s may still fall within the selection of primary tracks used for jet reconstruction.

Contamination of jet tracks with secondary tracks from V^0 decays biases the jet reconstruction in several ways. Daughter tracks in jets increase the reconstructed jet momentum and the harder ones can change jet orientation or even initiate reconstruction of more jets. This can play an important role in case of secondary protons from decays of high-p_T Λ baryons. Such proton daughter takes about $80\,\%$ of momentum of the mother Λ particle and, when considered to be a primary proton, can induce reconstruction of an additional signal jet and become its leading particle. This leads to an artificial overestimation of the yields of Λ particles in jets. Pions from K^0_S decays do not represent such an issue because they tend to share momentum of the mother particle more symmetrically and are therefore usually softer than the protons from Λ decays. This effect is known to cause a significant bias in the analysis of the baryon-to-meson ratio in p–p collisions where it causes an undesirable enhancement of the Λ/K^0_S ratio in jets at larger $p_T^{V^0}$ and daughter tracks of V^0 candidates have to be removed from hybrid tracks prior to the jet reconstruction in order to get rid of the effect.

In central Pb–Pb collisions, the criteria used for selection of primary tracks are more strict than in p–p collisions and the position of the primary vertex is
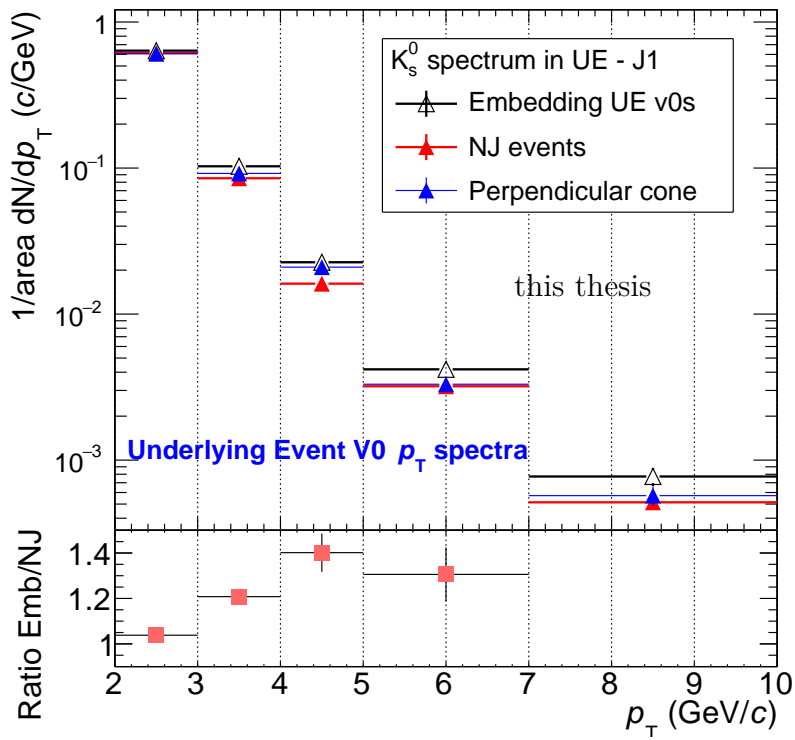
Figure 4.16: Comparison of the spectrum of K_S^0 in the cones of embedded jets to the spectrum of K_S^0 in no-jet events in central (0–10 %) Pb–Pb collisions at $\sqrt{s_{NN}} = 2.76$ TeV from year 2011. (Analysis performed by Alice Zimmermann.)
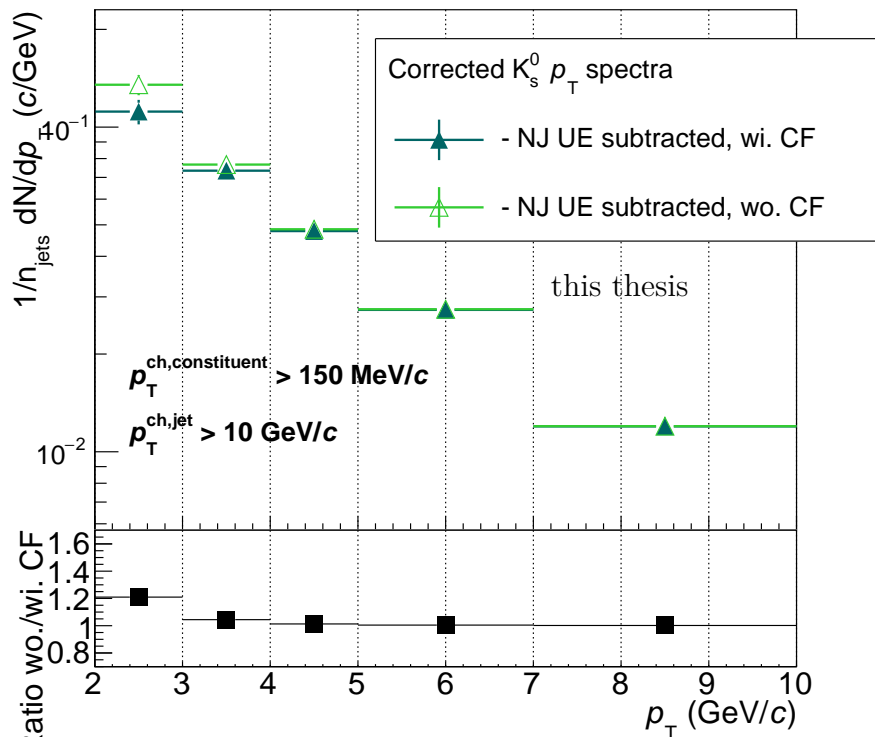
Figure 4.17: Comparison of the spectrum of K_S^0 after the UE subtraction with and without using the correction factor in central (0–10 %) Pb–Pb collisions at $\sqrt{s_{NN}} = 2.76$ TeV from year 2011. (Analysis performed by Alice Zimmermann.)

known with a much better precision. The contamination level should therefore be much lower. This effect is not expected to affect significantly the analysed jets and was therefore neglected in the preliminary results.

4.7 Systematic uncertainties

In order to estimate how much the final results depend on the choice of a particular analysis method and the choice of specific parameter values, the analysis was performed with several sets of settings and an uncertainty has been assigned to each source based on the deviations from the nominal results.

4.7.1 Sources of systematic uncertainties

The following analysis parts and effects are considered to be sources of systematic uncertainties:

- reconstruction efficiency of V^0s (selection cuts applied on V^0 candidates, Sec. 4.3.1),

- signal extraction (Sec. 4.3.2),

- subtraction of spectra of V^0s in UE (Sec. 4.6.2),

- subtraction of feed-down in jets (Sec. 4.6.3),

- estimation of material budget,

- subtraction of the average background density ρ (Sec. 4.4.2),

- fluctuations of the average background density ρ (Sec. 4.6.4),

- detector response (Sec. 4.6.4).

4.7.2 Estimation methods

Since the spectra of V^0 particles in jets suffer from relatively large statistical uncertainties, there was no unambiguous way of distinguishing statistical fluctuations (related purely to modifications of the data sample) and systematic deviations when qualifying the differences between results obtained with different methods or settings. In order to minimize the contribution of statistical fluctuations, several measures were taken.

The analysis is performed on the Grid. The code is sent to the servers, where the data files are stored, and executed locally. Outputs are collected and merged for further processing by the user. There is always an unpredictable fraction of the data files which are not analysed because of technical issues. So running the analysis repeatedly on the Grid never gives identical results. In order to reduce impact of these fluctuations, all variations in data were performed on the same data sample. This was achieved by running all the analysis instances (with different settings) in series, so that every data file was analysed either with all the variations or with none.

Most of the considered sources of uncertainties are not correlated to the value of jet momentum and should consequently give very similar relative uncertainties for both jet p_{T} thresholds. Relative systematic uncertainties estimated for $p_{\mathrm{T}}^{\text{jet,ch}} > 10\,\mathrm{GeV}/c$ are therefore used also for spectra with $p_{\mathrm{T}}^{\text{jet,ch}} > 20\,\mathrm{GeV}/c$, which have larger statistical uncertainties.

I also faced some conceptual problems related to the common ways of estimating systematic uncertainties. The usual ways involve either root mean square (RMS) or the Barlow criterion [114]. Both approaches however introduce some important shortcomings. I had to consider the following remarks.

- Only differences that can be distinguished from statistical uncertainties should be considered as systematic deviations.

- The contribution of a difference to the systematic uncertainty should have a smooth dependence on the size of the difference and on its statistical uncertainty.

- RMS is a smooth function of the differences but does not consider statistical uncertainties.

- The Barlow criterion takes into account statistical uncertainties but is not smooth and is usable only for subsets.

To make the estimation of systematic uncertainties more robust, I proposed an approach of weighted RMS (wRMS):

- The dissimilarity d of two numbers a and b that were measured with statistical uncertainties σ_a and σ_b is defined as:

$$d = \frac{a - b}{\sqrt{(\sigma_a^2 + \sigma_b^2)/k}}, \quad k = \begin{cases} 1 & \text{if } a,\ b \text{ come from independent samples,} \\ 2 & \text{if } a,\ b \text{ come from very similar samples.} \end{cases}$$

(4.35)

  The higher the dissimilarity is, the less compatible the numbers a and b are within statistical uncertainties. The factor k is introduced to take into account the fact that the statistical uncertainty of a difference of two numbers which were obtained using very similar data samples is smaller than the uncertainty of a difference of two numbers obtained independently.

- The dissimilarity value can be interpreted by transforming it into a weight w taking values between 0 and 1. The weight should quantify the measure of $a - b$ not being compatible with statistical fluctuations. Small weights (close to 0) would indicate that the difference is small with respect to statistical uncertainties and large weights (close to 1) would indicate that the difference is statistically significant. I assume that the probability of d being a statistical fluctuation can be expressed as $\mathrm{e}^{-d^2/2}$ (following the normal distribution) so I introduce the weight as the complement:

$$w = 1 - \mathrm{e}^{-d^2/2}.$$

(4.36)

- When estimating systematic uncertainties, a and b become the nominal result (obtained with the default settings) and a result obtained with a variation:

$$a - b \to \Delta_i = y_{\text{var},i} - y_{\text{default}}. \quad (4.37)$$

Each deviation Δ_i contributes to the mean square by its square weighted with the factor w_i so that the weighted RMS is defined as:

$$\text{wRMS} \overset{\text{def}}{=} \sqrt{\frac{1}{N_{\text{var}}} \sum_{i=1}^{N_{\text{var}}} \Delta_i^2 w_i}. \quad (4.38)$$

Reconstruction efficiency

Uncertainty of the reconstruction efficiency is estimated by varying values of the selection cuts in real and simulated data. Choice of variations was driven by an approach reflecting the way the uncertainties were estimated in the inclusive analysis [64, 89] and in the correlation analysis [69]. The variation values are chosen so that the uncorrected yield of inclusive V^0 particles integrated in the range $p_{\text{T}}^{V^0}/(\text{GeV}/c) \in [2, 10]$ decreases by approximately $10\,\%$. Since the feed-down fraction is directly related to the selection of primary V^0 particles, it was evaluated again for the variation of CPA. The variation values are listed in Tab. 4.3.

Table 4.3: Variations of V^0 selection cuts

variable	default	variation K_S^0	variation Λ
CPA	≥ 0.998	≥ 0.9996	≥ 0.9994
DCA between daughters	≤ 1	≤ 0.45	≤ 0.45
DCA of daughters to PV	≥ 0.1	≥ 0.2	≥ 0.2
$R^{\max}$ of the decay vertex	100	40	40
$R^{\min}$ of the decay vertex	5	7.3	7.3
transverse proper lifetime	≤ 5	≤ 2.8	≤ 2.8

Relative differences of the Λ/K_S^0 ratio ($\overline{\Lambda}$ included) resulting from modifying the selection cuts are displayed in Fig. 4.18 together with statistical uncertainties of the ratio $y_{\text{var}}/y_{\text{default}}$. The final relative uncertainty of the efficiency is evaluated as symmetric wRMS($k = 2$) of all cut variations and is displayed in the figure as boxes with black borders.

Signal extraction

Uncertainty of the signal extraction is estimated by varying the boundaries of the signal region and the side-band region.

I varied only the range of the signal region (and the inner side band edges accordingly). Changing the degree of the polynomial did not seem appropriate to me since every change resulted in a worse fit than with the default settings.

Variations of the invariant-mass intervals of the signal region are specified in the list below.

1. K_S^0 signal: $m_{\text{inv}}/(\text{GeV}/c^2) \in [0.43, 0.57] \to [0.45, 0.55]$,

2. Λ signal: $m_{\text{inv}}/(\text{GeV}/c^2) \in [1.105, 1.130] \to [1.110, 1.125]$,
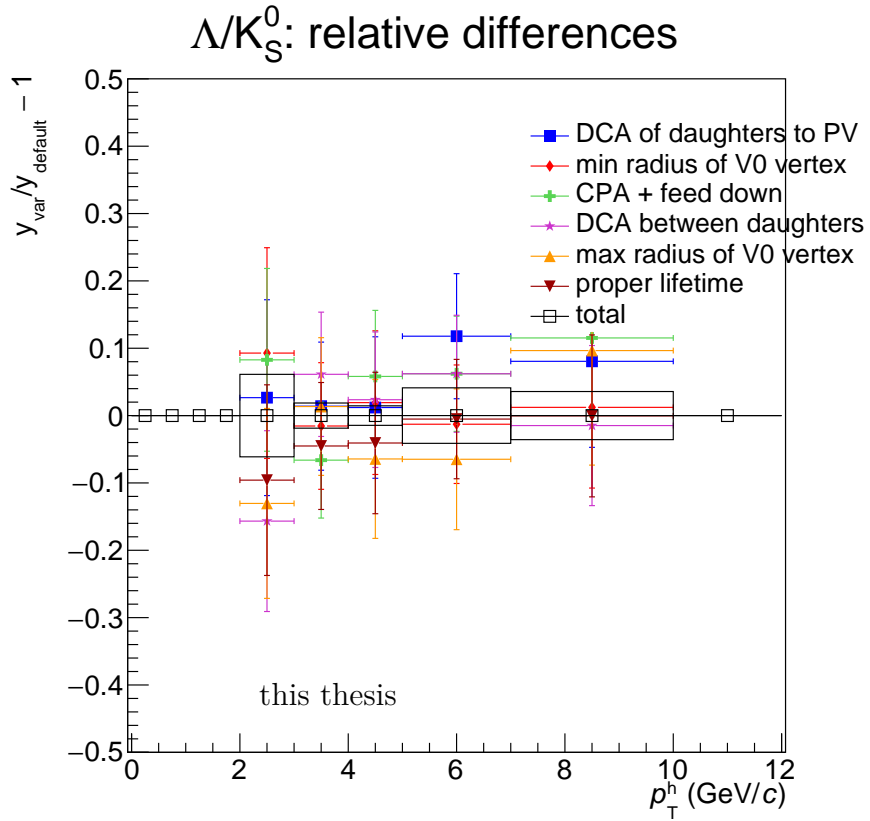
Figure 4.18: Deviations of the $(\Lambda + \overline{\Lambda})/2\mathrm{K}^0_\mathrm{S}$ ratio in jets ($R = 0.2$, $p_\mathrm{T}^\mathrm{jet,ch} > 10\,\mathrm{GeV}/c$) in central (0–10 %) Pb–Pb collisions at $\sqrt{s_\mathrm{NN}} = 2.76\,\mathrm{TeV}$ from year 2011 resulting from modifying the selection cuts of V^0 candidates.

3. variation 1 and variation 2 together.

Such variations provide 3 different results for the Λ/K_S^0 ratio which deviate by 4% at most at low $p_T^{V^0}$ (as calculated with the wRMS($k = 2$) method) and slightly less at higher $p_T^{V^0}$. The deviations and the calculated systematic uncertainty are displayed in Fig. 4.19. The uncertainty propagated to the final results was evaluated as 4% and considered as symmetric and constant.
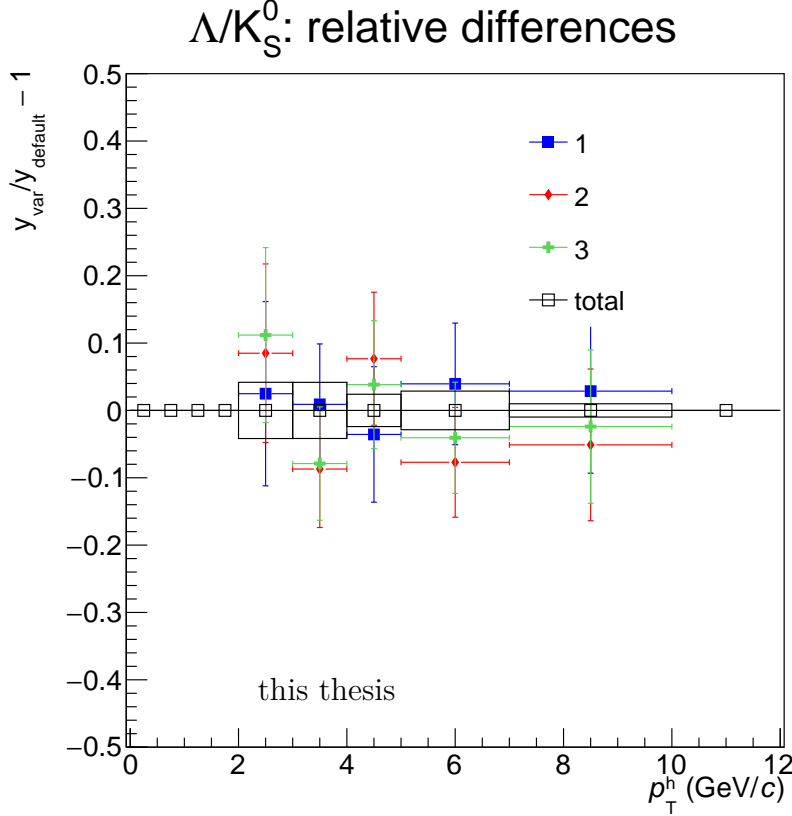
Figure 4.19: Deviations of the $(\Lambda + \overline{\Lambda})/2K_S^0$ ratio in jets ($R = 0.2$, $p_T^{\text{jet,ch}} > 10\,\text{GeV}/c$) in central (0–10 %) Pb–Pb collisions at $\sqrt{s_{\text{NN}}} = 2.76\,\text{TeV}$ from year 2011 resulting from changing boundaries of the signal extraction regions.

Subtraction of the underlying event

Uncertainty of the subtraction of spectra of V^0s in the underlying event is estimated by comparing other methods (OC, PC, RC, MCC; see Sec. 4.6.2) with the default one (NJ). The final uncertainty is taken as symmetric wRMS($k = 1$). The deviations and the assigned systematic uncertainty are displayed in Fig. 4.20

At low $p_T^{V^0}$, V^0 particles are produced mainly by background processes so the spectra of particles in jets are very sensitive to the differences between methods of estimating the underlying event spectra, whereas production of V^0 particles at higher $p_T^{V^0}$ is not so much contaminated by soft processes anymore so the accuracy of estimating the contribution of the underlying event is less relevant.
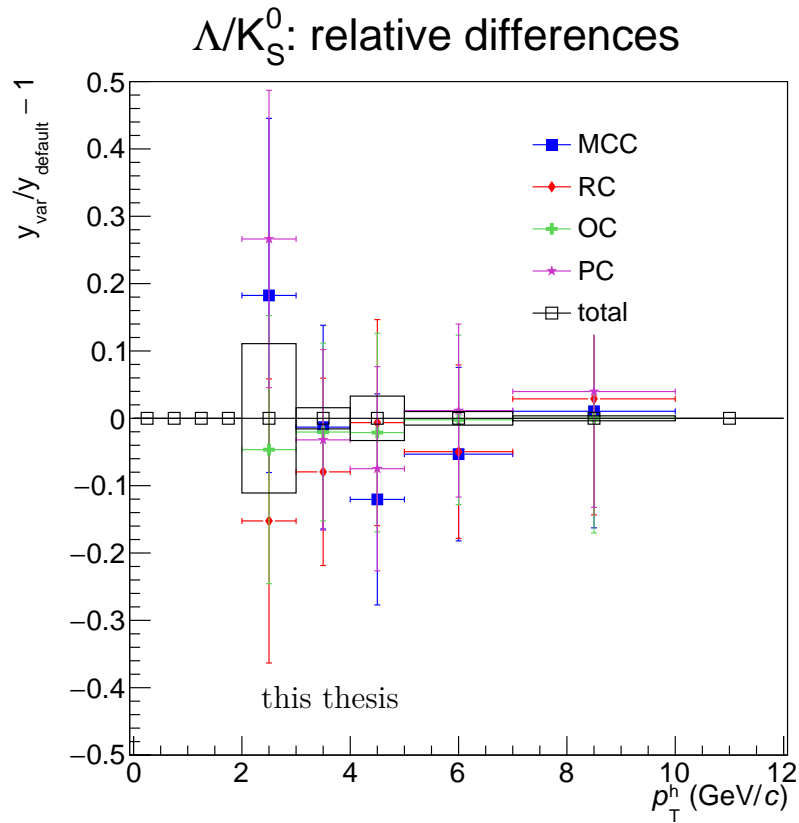
Figure 4.20: Deviations of the $(\Lambda + \overline{\Lambda})/2K_S^0$ ratio in jets ($R = 0.2$, $p_T^{\text{jet,ch}} > 10\,\text{GeV}/c$) in central (0–10 %) Pb–Pb collisions at $\sqrt{s_{\text{NN}}} = 2.76\,\text{TeV}$ from year 2011 resulting from using different methods of estimating the spectra of V^{0}s in the underlying event.

Subtraction of the feed-down fraction

Uncertainty of the subtraction of the feed-down fraction of Λ in jets is determined by the difference between the fraction of inclusive Λ in Pb–Pb collisions and the fraction obtained for Λ in jets in p–p collisions simulated by PYTHIA 8 (see Fig. 4.13). This uncertainty comes from ignorance of spectra of Ξ particles in jets and so is not related to the analysis methods. For this reason, the difference is considered as a separate asymmetric uncertainty, i.e. is not combined with uncertainties from other sources. The propagated relative uncertainty caused by this difference is displayed in Fig. 4.21.
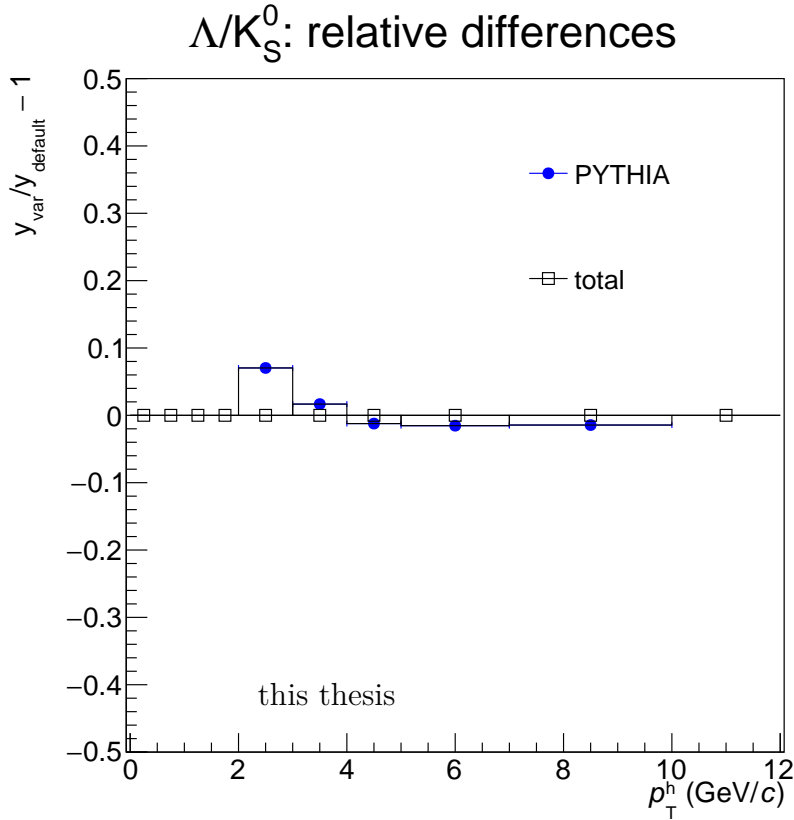
Figure 4.21: Deviations of the $(\Lambda + \overline{\Lambda})/2\mathrm{K}_S^0$ ratio in jets ($R = 0.2$, $p_T^{\mathrm{jet,ch}} > 10\,\mathrm{GeV}/c$) in central (0–10 %) Pb–Pb collisions at $\sqrt{s_{\mathrm{NN}}} = 2.76\,\mathrm{TeV}$ from year 2011 resulting from using the feed-down fraction estimated using jets in events generated by PYTHIA 8.

Material budget

Uncertainty related to the determination of the thickness of the detector material crossed by particles ("material budget") is considered to be the same as for V^0s in p–p collisions at $\sqrt{s} = 0.9\,\mathrm{TeV}$ [115] since the tracking detectors are the same. Authors of this analysis estimated the uncertainties at $p_T^{\mathrm{V}^0} \approx 3\,\mathrm{GeV}/c$ to be 1.1 % for K_S^0, 1.6 % for Λ and 4.5 % for $\overline{\Lambda}$.

Under the assumption that the spectra of Λ and $\overline{\Lambda}$ are very similar, the relative

uncertainties can be propagated into the ratio as:

$$R = \frac{\Lambda + \overline{\Lambda}}{2K_S^0}, \qquad \Lambda \approx \overline{\Lambda} \quad \Rightarrow \quad \sigma_{R,\text{rel.}}^2 \approx \sigma_{K_S^0,\text{rel.}}^2 + \frac{1}{4}\left(\sigma_{\Lambda,\text{rel.}}^2 + \sigma_{\overline{\Lambda},\text{rel.}}^2\right). \quad (4.39)$$

The final relative uncertainty of the ratio R is then $2.6\,\%$.

Discrepancy between data from years 2010 and 2011

A crucial test of the analysis is the successful reproduction of the results of the inclusive analysis performed by the LF group. If the analysis is repeated with the same settings, it should give the same results. For the cross-check I used almost the same procedures as those used in the original analysis but there were some remaining differences that concerned data format, simulation data set and signal extraction method. Ratio of the spectra obtained with my analysis and the published spectra, using the 2010 data and centrality range 0–5 %, is shown in Fig. 4.22. Only statistical uncertainties from both spectra are included in each ratio. The agreement is better than 5 % for almost all data points and is compatible with the statistical uncertainties.
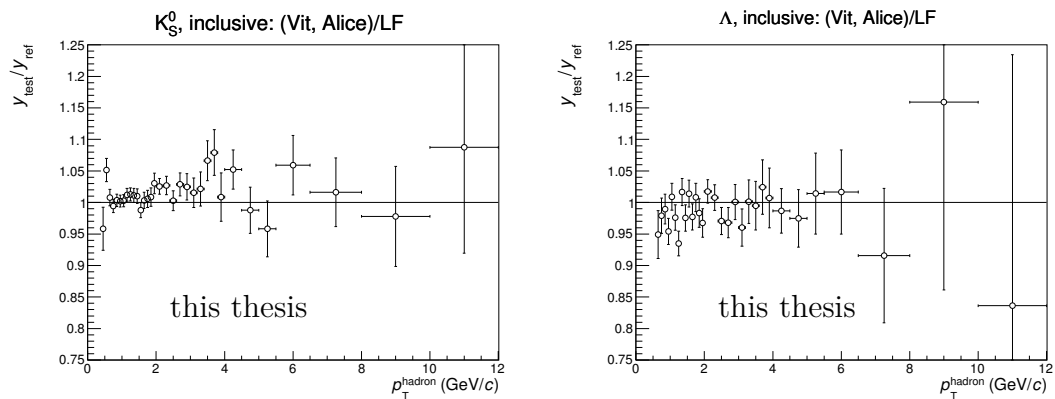
Figure 4.22: Comparison of inclusive V^0 spectra in the 2010 data and the published results in Pb–Pb collisions at $\sqrt{s_{\text{NN}}} = 2.76\,\text{TeV}$, using events with centrality 0–5 %.

Results of the analysis performed on data taken in 2011 should also be compatible with the results based on data taken in 2010, since both data sets were acquired with the same type of collisions so the measured physics processes are identical and detector conditions should not affect results of the measurement. The corresponding ratio is plotted in Fig. 4.23. Surprisingly, the spectra obtained with data taken in 2011 differ significantly from the spectra in the 2010 data. The effect for K_S^0 is about $10\,\%$ at $p_T^{V^0}$ above $2\,\text{GeV}/c$ and about $20\,\%$ for Λ at larger $p_T^{V^0}$.

In order to identify the source of this discrepancy, I made a ratio of uncorrected inclusive spectra obtained with my analysis in both data sets. Ratios of uncorrected inclusive V^0 spectra obtained with this analysis in the 2010 and 2011 data are shown in Fig. 4.24. Except for the range of $p_T^{V^0}$ below $2\,\text{GeV}/c$, the uncorrected spectra agree within $5\,\%$, therefore the discrepancy is unambiguously associated with the corrections.
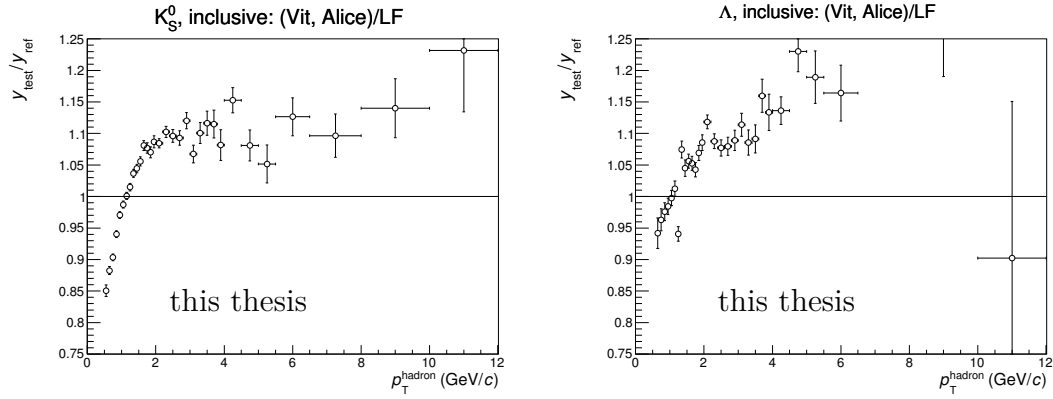
Figure 4.23: Comparison of inclusive V^0 spectra in the 2011 data and the published results in Pb–Pb collisions at $\sqrt{s_{\mathrm{NN}}} = 2.76\,\mathrm{TeV}$, using events with centrality 0–5 %.
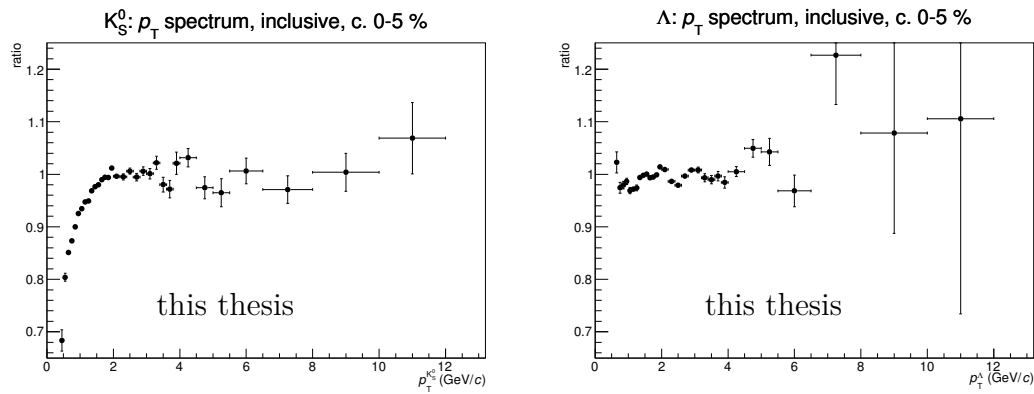
Figure 4.24: Comparison of uncorrected inclusive V^0 spectra obtained with this analysis in the 2010 and 2011 data in Pb–Pb collisions at $\sqrt{s_{\mathrm{NN}}} = 2.76\,\mathrm{TeV}$, using events with centrality 0–5 %.

The reconstruction efficiencies of V^0 particles in 2010 and 2011 are compared in the ratio in Fig. 4.25. The efficiency ratio manifests for both particle species a trend that is strikingly similar to the original discrepancy displayed in Fig. 4.23. One can conclude that the difference between simulated data is the main source of the discrepancy between spectra of V^0 particles at $p_T^{V^0} > 2\,\mathrm{GeV}/c$ obtained in the 2010 and 2011 data.
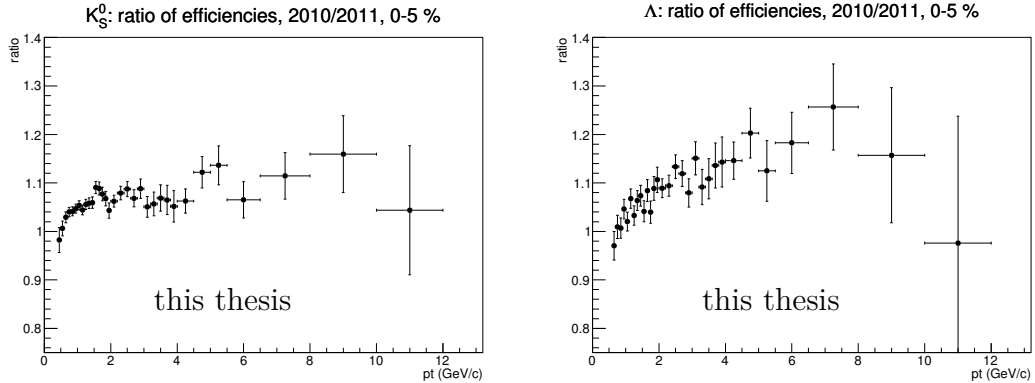
Figure 4.25: Comparison of the reconstruction efficiency in 2010 and 2011 data in Pb–Pb collisions at $\sqrt{s_{\mathrm{NN}}} = 2.76\,\mathrm{TeV}$, using events with centrality 0–5 %.

Because of a similar trend, the differences of spectra partially cancel out in the Λ/K_S^0 ratio at low $p_T^{V^0}$ but a remaining deviation persists. An additional symmetric systematics uncertainty of 10 % in the Λ/K_S^0 ratio in jets has been assigned to this discrepancy.

The effect has been confirmed by other analyses and extensive effort has been made to identify its source. The problem is believed to be related to a bad calibration of the tracking detectors including the TPC but its origin remains unclear.

Discrepancy between Λ and $\overline{\Lambda}$ spectra

In the collisions at the LHC, the productions of particles and anti-particles are assumed to be symmetrical. However, the inclusive spectra of Λ and $\overline{\Lambda}$ particles obtained with this analysis are different. The ratio of both spectra is plotted in Fig. 4.26. The asymmetry is observed also in other collision systems (p–p, p–Pb) and depends on particle pseudorapidity and on polarity of the magnetic field of the solenoid magnet. The difference is more pronounced for negative pseudorapidty and for positive polarity.

Similarly to the discrepancy between 2010 and 2011 data, this discrepancy is expected to have origin in the TPC calibration but has not been resolved yet. An additional symmetric systematics uncertainty of 6 % in the Λ/K_S^0 ratio in jets has been assigned to this discrepancy.

Other sources

Uncertainty related to the choice between scalar and vectorial subtraction of the average background density ρ has not been studied yet.

Uncertainties coming from the fluctuations of ρ have been studied using simulated jets embedded into real Pb–Pb events. Based on the first results of the
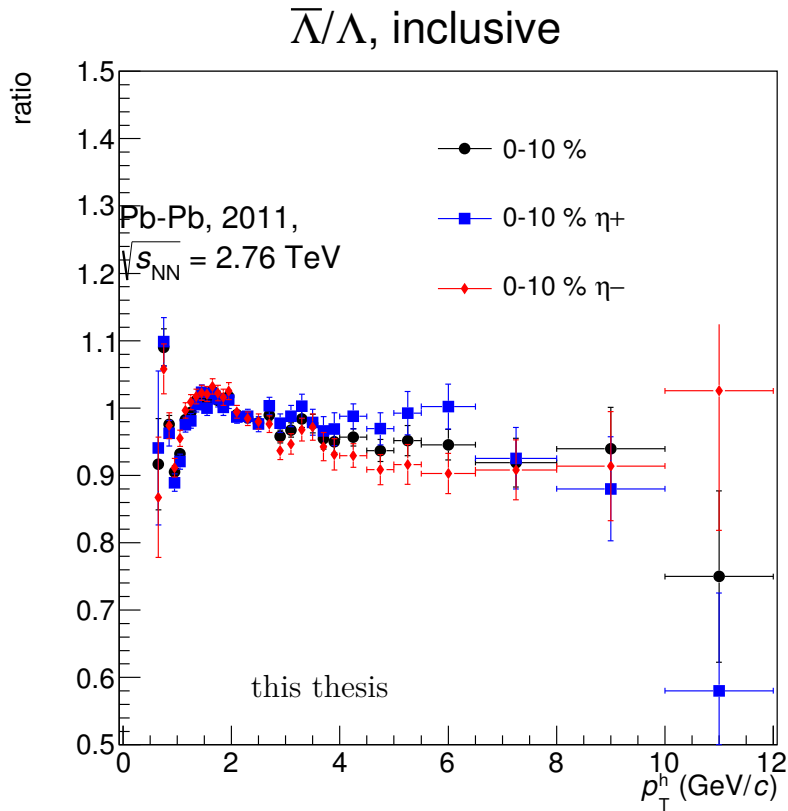
Figure 4.26: Ratio of corrected inclusive spectra of Λ and $\overline{\Lambda}$ in central (0–10 %) Pb–Pb collisions at $\sqrt{s_{\mathrm{NN}}} = 2.76\,\mathrm{TeV}$ from year 2011. Square data points show the ratio for particles in the region of positive pseudorapidity, diamond data points correspond to the region of negative pseudorapidity, circle data points include particles in both regions.

embedding studies, these uncertainties were neglected in the preliminary results using $R = 0.2$.

4.7.3 Overview of uncertainties from individual sources

Contributions from different sources were combined quadratically except for the feed-down subtraction which is treated as a separate asymmetric uncertainty. Uncertainties from individual sources are plotted in Fig. 4.27 together with the resulting total uncertainty. Dominant contributions to the uncertainties come from the two discrepancies and from the subtraction of the underlying event in the lowest $p_{\mathrm{T}}^{\mathrm{V}^0}$ region.
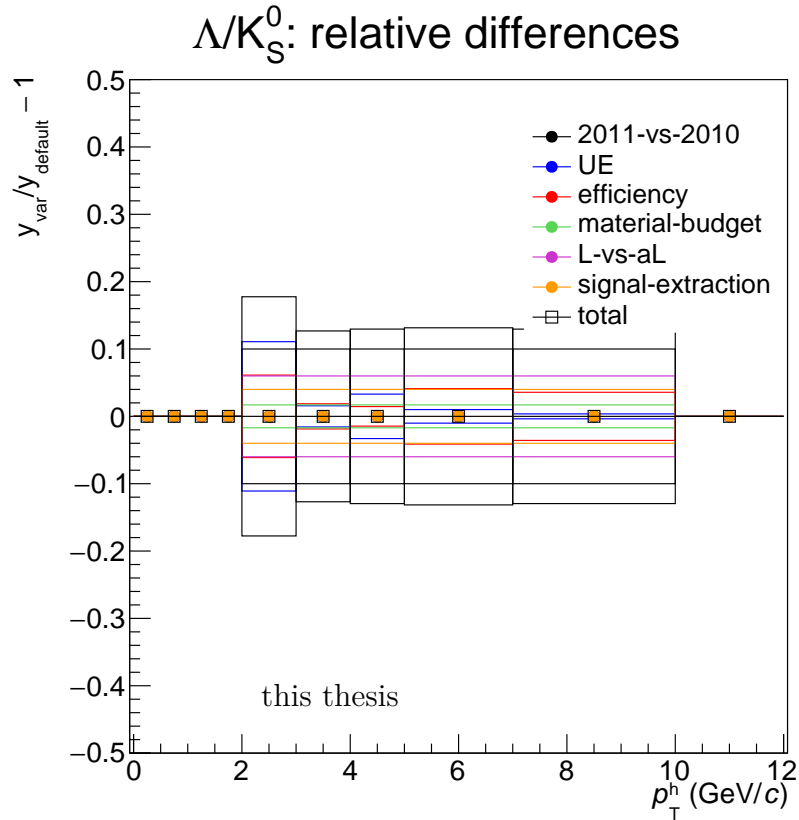
Figure 4.27: Combined systematic uncertainties of the $\Lambda/\mathrm{K}_{\mathrm{S}}^0$ ratio in jets ($R = 0.2$, $p_{\mathrm{T}}^{\mathrm{jet,ch}} > 10\,\mathrm{GeV}/c$) in central (0–10 %) Pb–Pb collisions at $\sqrt{s_{\mathrm{NN}}} = 2.76\,\mathrm{TeV}$ from year 2011.

5. Results

5.1 Spectra of V^0 particles in jets

The measured spectra of V^0 particles in charged jets for $D = R = 0.2$ and for two p_T^{jet} thresholds $(10\,\text{GeV}/c,\ 20\,\text{GeV}/c)$ are presented for K_S^0 in Fig. 5.1, for Λ in Fig. 5.2 and for $\overline{\Lambda}$ in Fig. 5.3. The systematic uncertainties for feed-down of Λ and $\overline{\Lambda}$ are in this case included in the combined systematic uncertainties of the respective spectra.

For all particle species, there is a visible difference in slope and magnitude between spectra with different p_T^{jet} thresholds. Spectra of particles in jets with lower p_T^{jet} threshold are clearly steeper, indicating that production of jets with lower mean p_T^{jet} is accompanied by production of V^0 particles with lower mean $p_T^{V^0}$ and vice versa, i.e. that softer jets consist of softer particles than harder jets. Second observation is that spectra of particles in jets with higher p_T^{jet} threshold are always higher than spectra in jets with lower threshold. This can mean that more particles are produced in harder jets or that harder jets are more collimated. Both interpretations are in agreement with the results of measurement of properties of jets in p–p collisions at $\sqrt{s} = 7\,\text{TeV}$ [116] where the mean number of charged particles in jets as well as the collimation of particles around the jet axis increase with jet momentum.
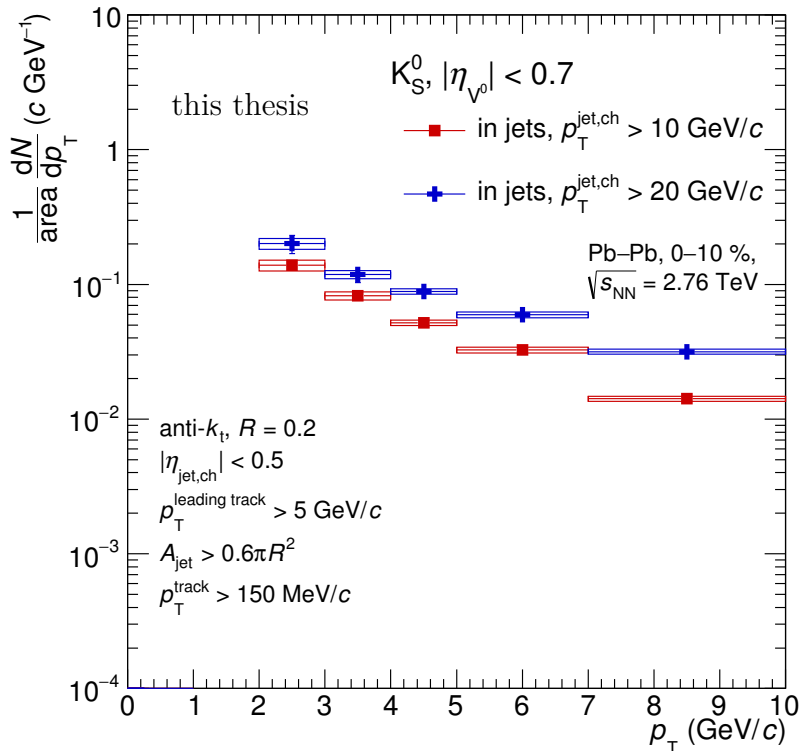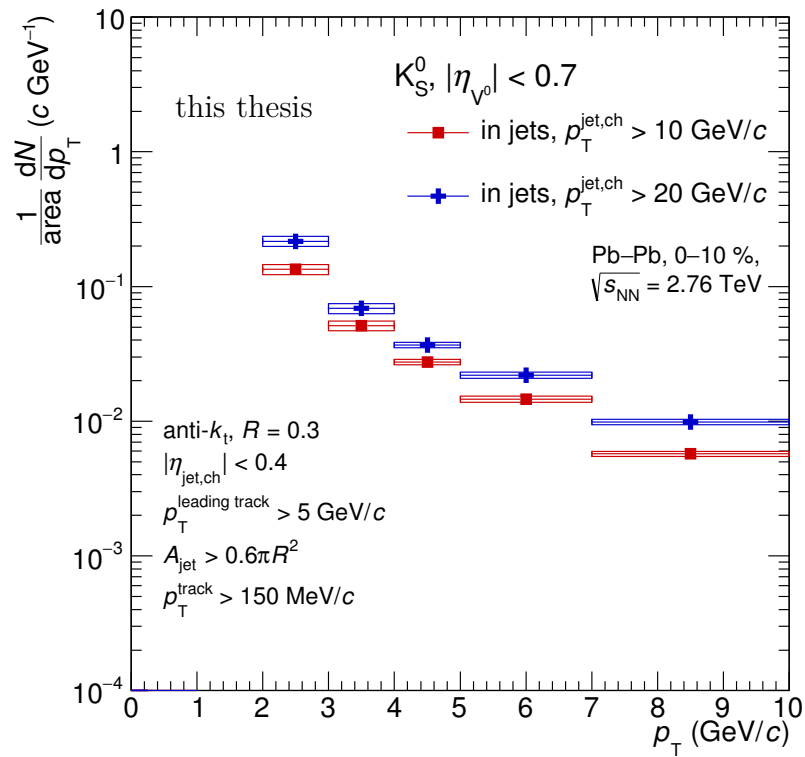

Figure 5.1: Spectrum of K_S^0 in charged jets reconstructed with $R = 0.2$ in central (0–10 %) Pb–Pb collisions at $\sqrt{s_{\text{NN}}} = 2.76\,\text{TeV}$ from year 2011.
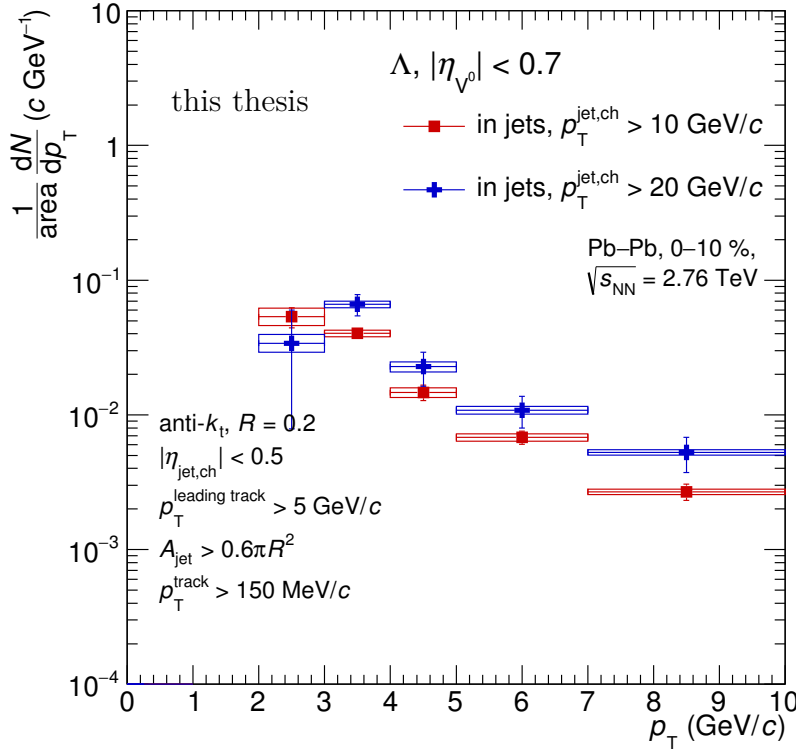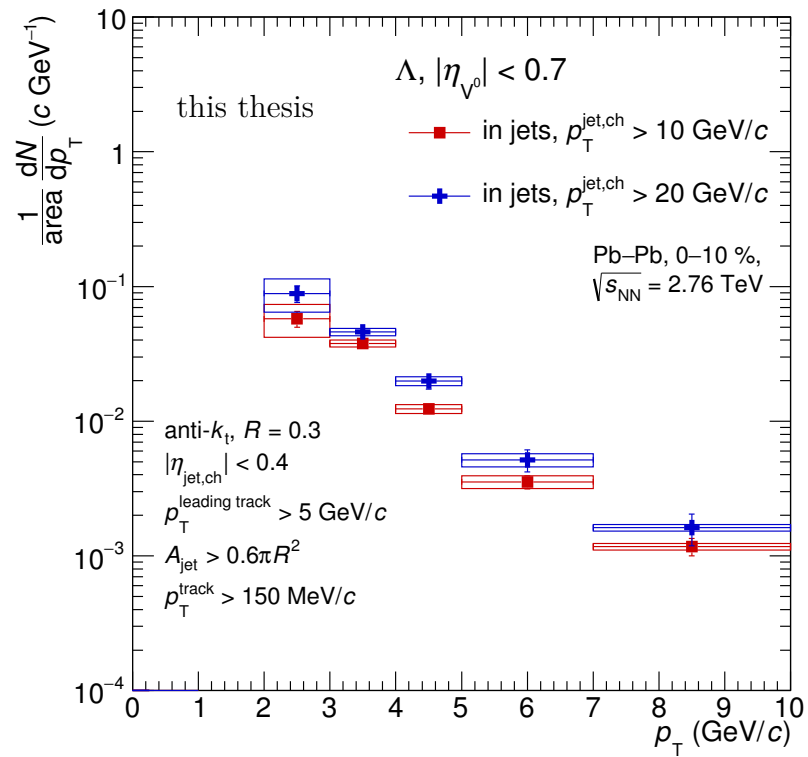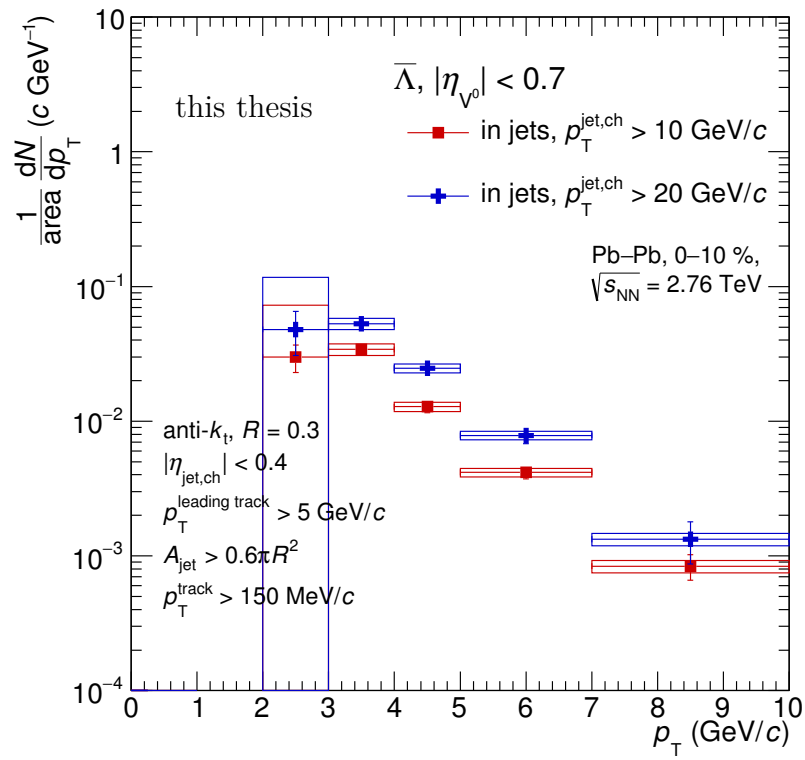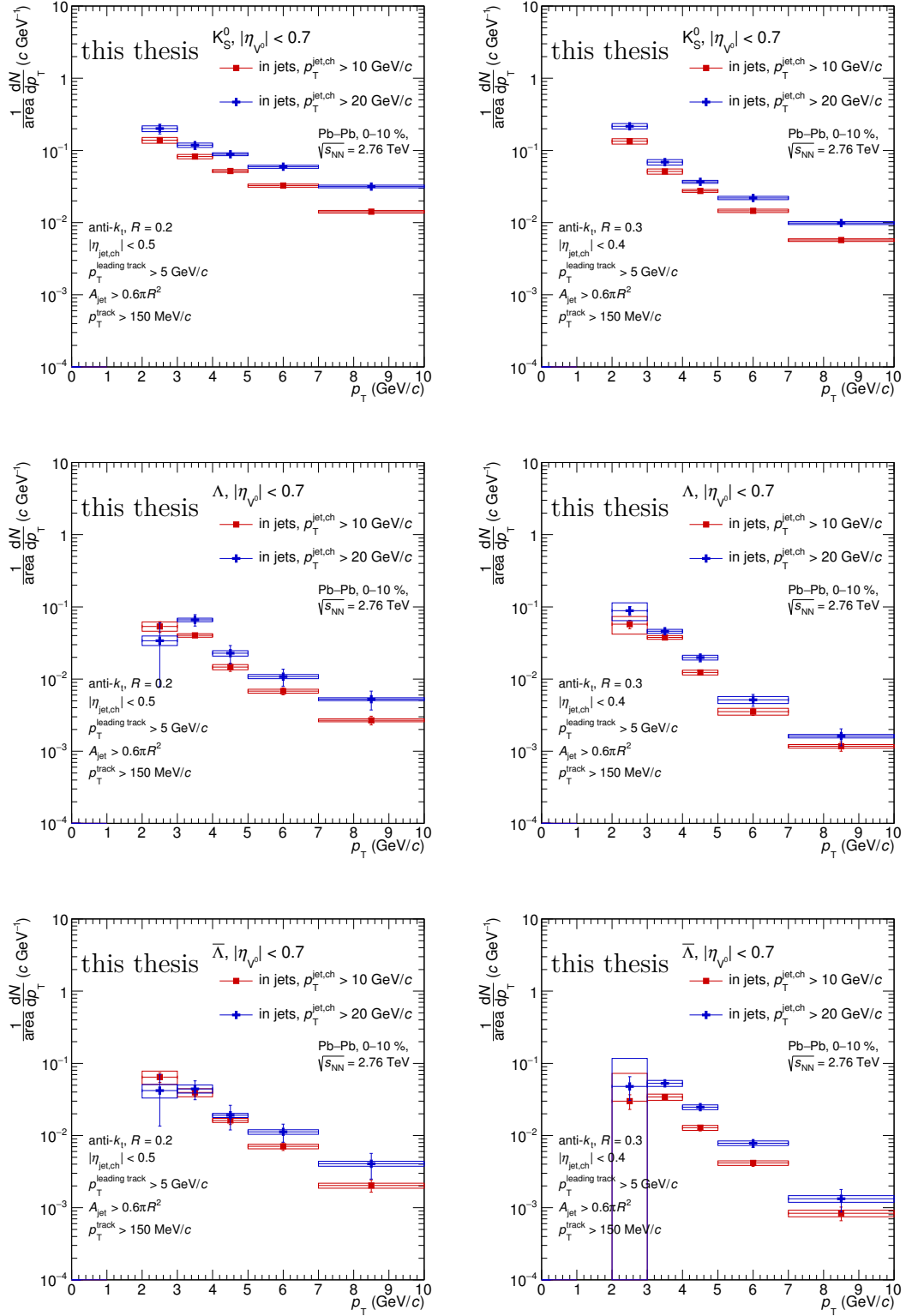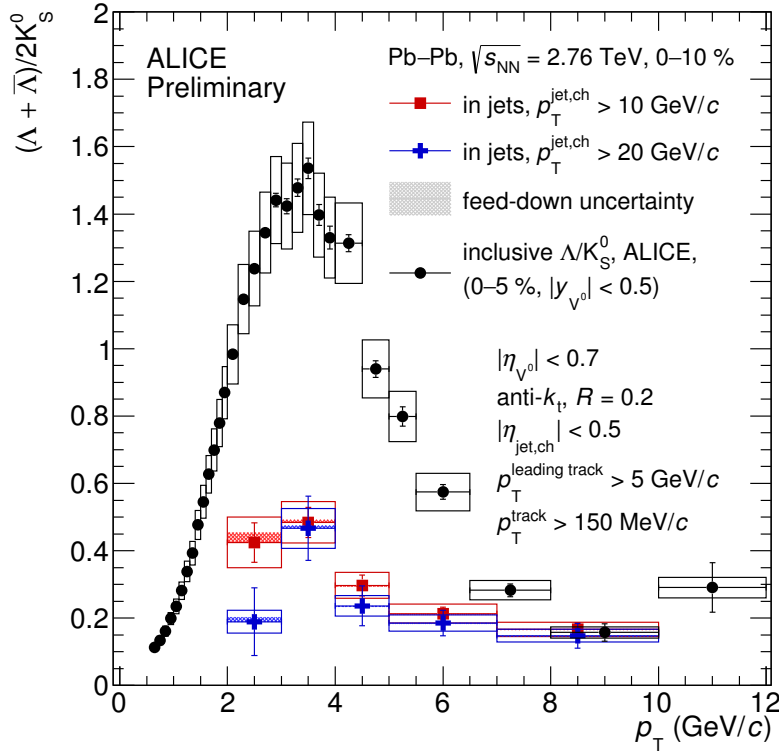
Figure 5.2: Spectrum of Λ in charged jets reconstructed with $R = 0.2$ in central (0–10 %) Pb–Pb collisions at $\sqrt{s_{\mathrm{NN}}} = 2.76$ TeV from year 2011.

The measured spectra of V^0 particles in charged jets for $D = R = 0.3$ and both $p_{\mathrm{T}}^{\mathrm{jet}}$ thresholds are presented for K_S^0 in Fig. 5.4, for Λ in Fig. 5.5 and for $\overline{\Lambda}$ in Fig. 5.6. The spectra exhibit similar features as the spectra measured for $D = R = 0.2$.

Spectra of particles in jets obtained for $R = 0.2$ and $R = 0.3$ are compared for all particle species in Fig. 5.7.

Compared to the spectra obtained for smaller jet cones, the spectra of particles in jets reconstructed with $R = 0.3$ are softer (i.e. steeper), lower (at larger $p_{\mathrm{T}}^{V^0}$) and there is no significant difference between slopes of spectra in the two $p_{\mathrm{T}}^{\mathrm{jet}}$ intervals. One reason for the density of particles at larger $p_{\mathrm{T}}^{V^0}$ in jet cones with $R = D = 0.3$ being lower with respect to $R = D = 0.2$ could be the fact that harder particles appear closer to the jet axis. However, this effect would be of the same order as the ratio of the respective cone areas so it cannot explain the much larger difference. A more likely explanation of this effect consists in the dependence of the measured jet momentum on the resolution parameter. A jet reconstructed in a region of an event with a given resolution R has a larger p_{T} than a jet reconstructed in the same region with a smaller R, even after the background subtraction, since it collects jet constituents from a larger area of the event. If the same $p_{\mathrm{T}}^{\mathrm{jet}}$ thresholds are imposed on samples reconstructed with different resolutions, some jets with the smaller R that are considered too soft, as they did not pass the selection, correspond to jets with the larger R that did pass the selection. Therefore, the sample of jets that passed the selection cuts
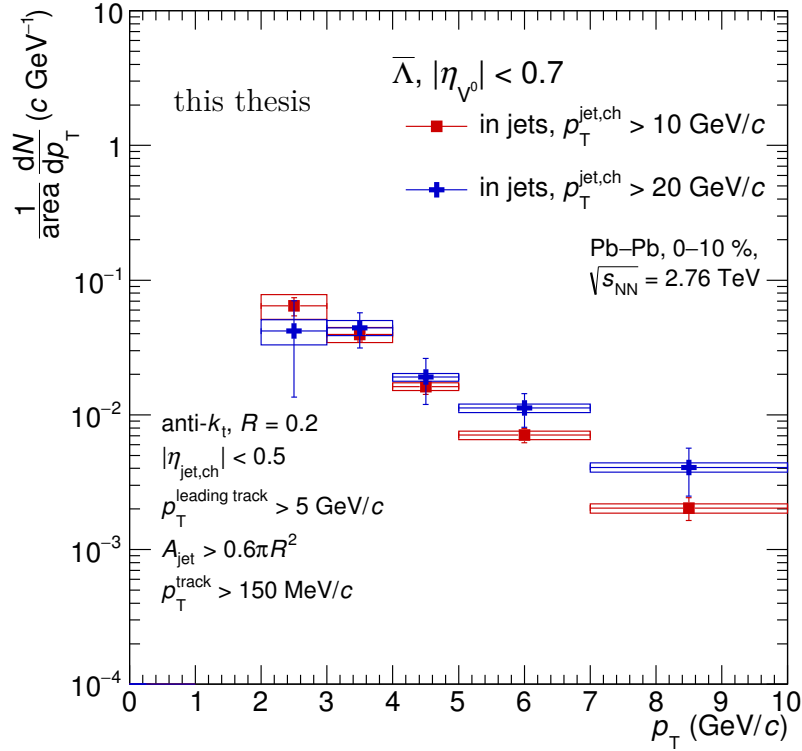
Figure 5.3: Spectrum of $\overline{\Lambda}$ in charged jets reconstructed with $R = 0.2$ in central (0–10 %) Pb–Pb collisions at $\sqrt{s_{\mathrm{NN}}} = 2.76\,\mathrm{TeV}$ from year 2011.

while using the larger resolution parameter contains a smaller fraction of jets produced from hard partons and a larger contribution of softer jets which do not contain so many hard particles. The same argument can be used to explain the disappearance of the dependence of the slopes of spectra on the $p_{\mathrm{T}}^{\mathrm{jet}}$ threshold. The number of jets reconstructed with the larger resolution is decreased by a smaller (more restricted) acceptance in η but those jets that are selected have larger mean p_{T}. (For jets with $p_{\mathrm{T}}^{\mathrm{jet}} > 10\,\mathrm{GeV}/c$, $\langle p_{\mathrm{T}}^{\mathrm{jet}} \rangle = 15.5\,\mathrm{GeV}/c$ for $R = 0.2$ and $\langle p_{\mathrm{T}}^{\mathrm{jet}} \rangle = 17.2\,\mathrm{GeV}/c$ for $R = 0.3$.) So while there is about the same number of jets with $p_{\mathrm{T}} > 10\,\mathrm{GeV}/c$ reconstructed with $R = 0.2$ and with $R = 0.3$ (6.7×10^5), jets with $p_{\mathrm{T}}^{\mathrm{jet}} > 20\,\mathrm{GeV}/c$ represent 23.7 % of them in case of $R = 0.3$ compared to only 12.6 % for $R = 0.2$. Therefore, the difference between the jet samples selected with the two $p_{\mathrm{T}}^{\mathrm{jet}}$ thresholds is smaller for $R = 0.3$ than for $R = 0.2$. An additional process modifying the shape of spectra of particles in jets by affecting the composition of the sample of selected jets is residual contribution of soft background to the jet momenta. As the background density is not isotropic within events but is subtracted from reconstructed jet momenta only as a mean value for the entire given event, upward fluctuations of the background level shift the p_{T} of soft jets upwards and increase the contribution of the underlying event to the spectra of selected jets.

Figure 5.4: Spectrum of K_S^0 in charged jets reconstructed with $R = 0.3$ in central (0–10 %) Pb–Pb collisions at $\sqrt{s_{\mathrm{NN}}} = 2.76\,\mathrm{TeV}$ from year 2011.

Figure 5.5: Spectrum of Λ in charged jets reconstructed with $R = 0.3$ in central (0–10 %) Pb–Pb collisions at $\sqrt{s_{NN}} = 2.76\,\text{TeV}$ from year 2011.

Figure 5.6: Spectrum of $\overline{\Lambda}$ in charged jets reconstructed with $R = 0.3$ in central (0–10 %) Pb–Pb collisions at $\sqrt{s_{\mathrm{NN}}} = 2.76$ TeV from year 2011.

Figure 5.7: Spectra of V^0 particles in charged jets in central (0–10 %) Pb–Pb collisions at $\sqrt{s_{\mathrm{NN}}} = 2.76\,\mathrm{TeV}$ from year 2011, compared for $R = 0.2$ and $R = 0.3$.

5.2 Λ/K_S^0 ratio in jets

The fully corrected results of the measurement of the Λ/K_S^0 ratio in charged jets in central Pb–Pb collisions obtained with this analysis for $D = R = 0.2$ are presented in Fig. 5.8. The p_T dependence of the ratio is plotted in the range $2\,\text{GeV}/c < p_T^{V^0} < 10\,\text{GeV}/c$ for both jet p_T thresholds and compared with the inclusive ratio measured by the ALICE Collaboration in the centrality range 0–5 % and the rapidity window $|y_{V^0}| < 0.5$.

Figure 5.8: Λ/K_S^0 ratio in charged jets reconstructed with $R = 0.2$ in central (0–10 %) Pb–Pb collisions at $\sqrt{s_{NN}} = 2.76\,\text{TeV}$ from year 2011 for $p_T^{\text{jet,ch}} > 10\,\text{GeV}/c$ and $p_T^{\text{jet,ch}} > 20\,\text{GeV}/c$, compared with the inclusive ratio.

The ratio measured for particles in jets is significantly lower than the inclusive ratio at intermediate p_T without exhibiting any dependence on the p_T^{jet} threshold. The ratio in jets is consistent with or slightly below the inclusive ratio in p–p collisions [115] (not shown, see Fig. 1.8 for comparison) and meets with the inclusive ratio in Pb–Pb collisions at higher $p_T^{V^0}$ ($> 7\,\text{GeV}/c$) where production by jet fragmentation starts to be the dominant hadronization process.

The current results obtained for $D = R = 0.3$ are presented in Fig. 5.9. Their relevance is limited by a large assumed contamination of jet constituents with soft background particles and also by the related large systematic uncertainty of the estimation of V^0 spectra in the underlying event.

The main message emerging from the presented results of this analysis is that the production of strange particles associated with jet fragmentation in central Pb–Pb collisions differs significantly from the inclusive production and the ratio of
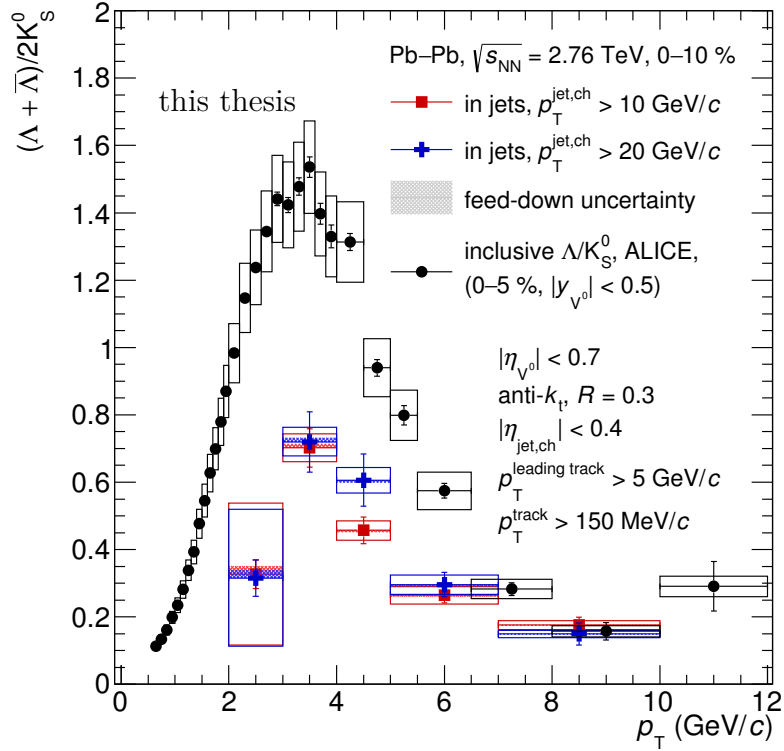
Figure 5.9: Λ/K_S^0 ratio in charged jets reconstructed with $R = 0.3$ in central (0–10 %) Pb–Pb collisions at $\sqrt{s_{NN}} = 2.76\,\text{TeV}$ from year 2011 for $p_T^{\text{jet,ch}} > 10\,\text{GeV}/c$ and $p_T^{\text{jet,ch}} > 20\,\text{GeV}/c$, compared with the inclusive ratio.

the yields of baryons in jets to the yields of mesons in jets does not seem to depend on the minimum transverse momentum of jets in the p_T^{jet} range accessible within this analysis. The Λ/K_S^0 ratio measured in jets indicates that the enhancement, observed in the ratio of inclusive spectra, is not present in the production of the selected jets and fragmentation of these jets therefore does not seem to be modified in the relative production of strange baryons and mesons. This implies that the dominant source of the enhancement comes from collective phenomena in the underlying event associated with soft processes in high-multiplicity collisions.

5.2.1 Dependence on D

An interesting insight can be provided by comparing the Λ/K_S^0 ratios in jets obtained for different combinations of values of the R and D parameters. Fig. 5.10 shows the results of determining the Λ/K_S^0 in jets for $R = 0.2, 0.3$ and several values of the D parameter. Ratios in jets are plotted together with the ratio in the underlying event (used for the UE subtraction) up to $p_T^{V^0} = 10\,\text{GeV}/c$ and compared with the inclusive ratio obtained in this analysis. Only statistical uncertainties are included.

The ratio in jets increases progressively as the cone widens from $D = 0.1$ up to $D = 0.3$ while keeping the jet resolution constant at $R = 0.2$. The comparison of the ratios obtained with the same cone size $D = 0.3$ and different jet resolutions
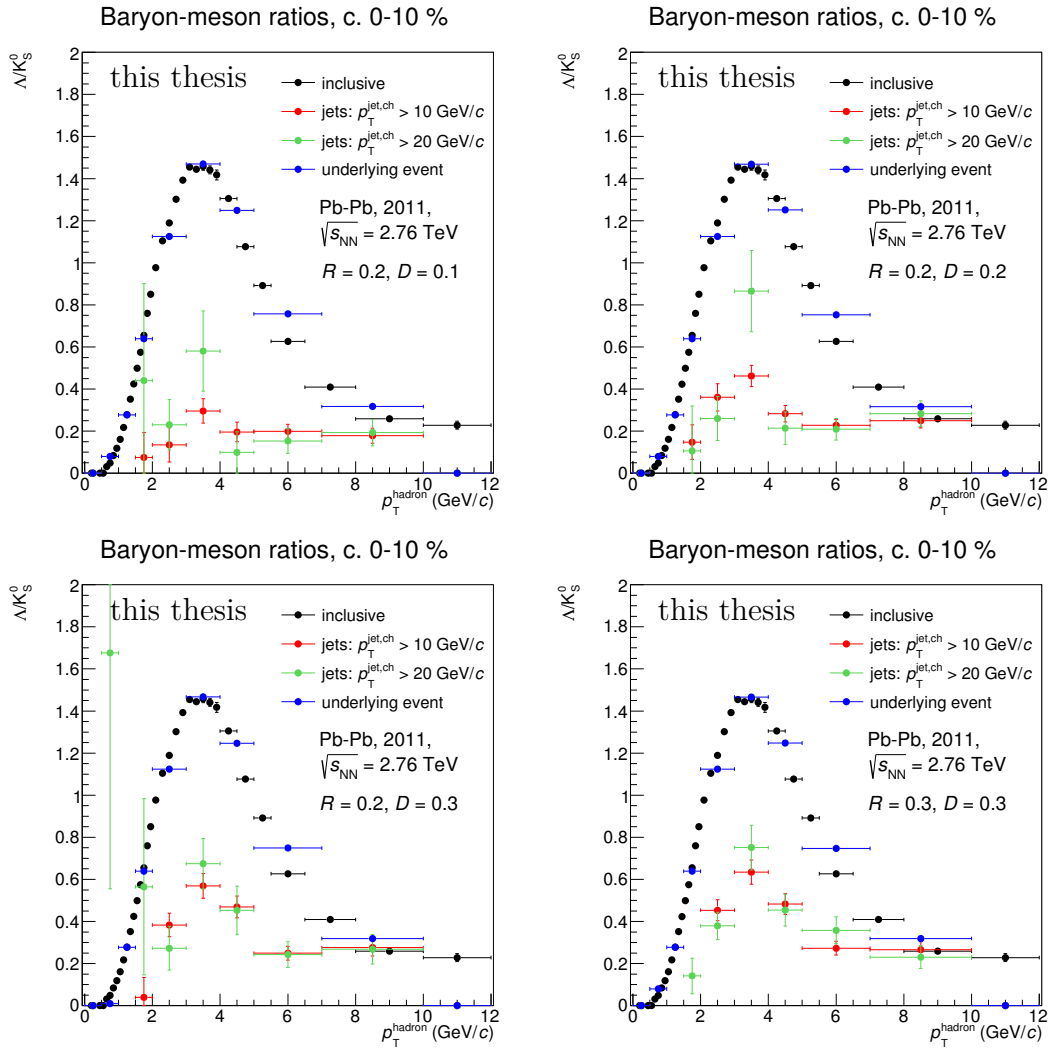
Figure 5.10: Λ/K_S^0 ratio in jets for $R = 0.2, D = 0.1, 0.2, 0.3$ and $R = D = 0.3$ in central (0–10 %) Pb–Pb collisions at $\sqrt{s_{\mathrm{NN}}} = 2.76\,\mathrm{TeV}$ from year 2011.

$R = 0.2$ and $R = 0.3$ suggests that the dependence on the resolution is not significant, if any, and that the ratio dependence is given by the cone size. Whereas the dependence of the ratio on D is clear at low $p_{\mathrm{T}}^{\mathrm{V}^0}$, it disappears in the region above $5\,\mathrm{GeV}/c$ where the ratio looks the same within statistical uncertainties for all parameter combinations. An agreement within statistical uncertainties for all parameter combinations can be seen also between ratios in jets measured for different $p_{\mathrm{T}}^{\mathrm{jet}}$ thresholds.

One way to interpret the increasing $\Lambda/\mathrm{K_S^0}$ ratio in jets as a function of the cone size D would be to deduce that $\mathrm{K_S^0}$ are more collimated around the jet axis than Λ and their number in the jets increases more slowly than the number of Λ as the cone is opening. A more plausible explanation however is an increasing fraction of the residual underlying event at low $p_{\mathrm{T}}^{\mathrm{V}^0}$, since as the cone gets wider, the ratio in jets becomes closer to the inclusive ratio. The region of larger $p_{\mathrm{T}}^{\mathrm{V}^0}$ above $5\,\mathrm{GeV}/c$ appears to be robust with respect to the estimation and subtraction of the underlying event, possibly because at $p_{\mathrm{T}}^{\mathrm{V}^0} = 4$–$5\,\mathrm{GeV}/c$ the spectra of V^0s in jets reach the same order of magnitude as the spectra in UE for both particle species and therefore the fraction of particles produced in jets becomes significant enough to make the resulting ratio of spectra stable with respect to changes of the analysis parameters R and D.

5.3 Comparison with related analyses

Another analysis focusing on the phenomenon of the $\Lambda/\mathrm{K_S^0}$ enhancement has been performed within the ALICE Collaboration using the same data from Pb–Pb collisions at $\sqrt{s_{\mathrm{NN}}} = 2.76\,\mathrm{TeV}$ but a different analysis approach [69]. The baryon-to-meson ratio is studied in jet-like angular correlations of V^0 particles with high-p_{T} charged primary trigger particles for $5\,\mathrm{GeV}/c < {p_{\mathrm{T}}^{\mathrm{trigger}}} < 10\,\mathrm{GeV}/c$ which serve as a tool for selection of event regions with particles produced in hard processes. Figure 5.11 shows the results obtained in the near-side peak and in the underlying event ("bulk"), compared with inclusive ratios in Pb–Pb and p–p collisions measured by ALICE and with ratios in reconstructed jets measured by the CDF Collaboration in p–$\overline{\mathrm{p}}$ collisions at $\sqrt{s} = 1.96\,\mathrm{TeV}$ [117]. The $\Lambda/\mathrm{K_S^0}$ ratio measured in the near-side peak is consistent with the inclusive ratio in p–p collisions and with the ratio in jets for $R = D = 0.2$ presented in this thesis.

The STAR Collaboration has recently presented results of measuring the $\Lambda/\mathrm{K_S^0}$ ratio in jet-like correlations in Cu–Cu collisions at $\sqrt{s_{\mathrm{NN}}} = 200\,\mathrm{GeV}$ in the centrality range 0–60 % for strange particles in the momentum range $2\,\mathrm{GeV}/c < p_{\mathrm{T}}^{\mathrm{V}^0} < 3\,\mathrm{GeV}/c$ and for trigger particles with momenta $3\,\mathrm{GeV}/c < p_{\mathrm{T}}^{\mathrm{trigger}} < 6\,\mathrm{GeV}/c$ [70]. The $\Lambda/\mathrm{K_S^0}$ ratio measured in the near-side peak is consistent with the inclusive particle ratios measured by STAR and ALICE in p–p collisions at energies $\sqrt{s} = 200\,\mathrm{GeV}$ and $\sqrt{s} = 7\,\mathrm{TeV}$, respectively. The comparison of the results with the inclusive ratios and with predictions of different PYTHIA tunes is shown in Fig. 5.12.

Results of the measurement of the $\Lambda/\mathrm{K_S^0}$ ratio in reconstructed jets in proton–nucleus collisions are available for the p–Pb collisions at $\sqrt{s_{\mathrm{NN}}} = 5.02\,\mathrm{TeV}$ measured by ALICE using a technique almost identical to the one presented in this thesis [71]. Figure 5.13 shows the $\Lambda/\mathrm{K_S^0}$ ratio measured in charged jets in high-multiplicity p–Pb collisions for two $p_{\mathrm{T}}^{\mathrm{jet}}$ thresholds. The ratio is compared with
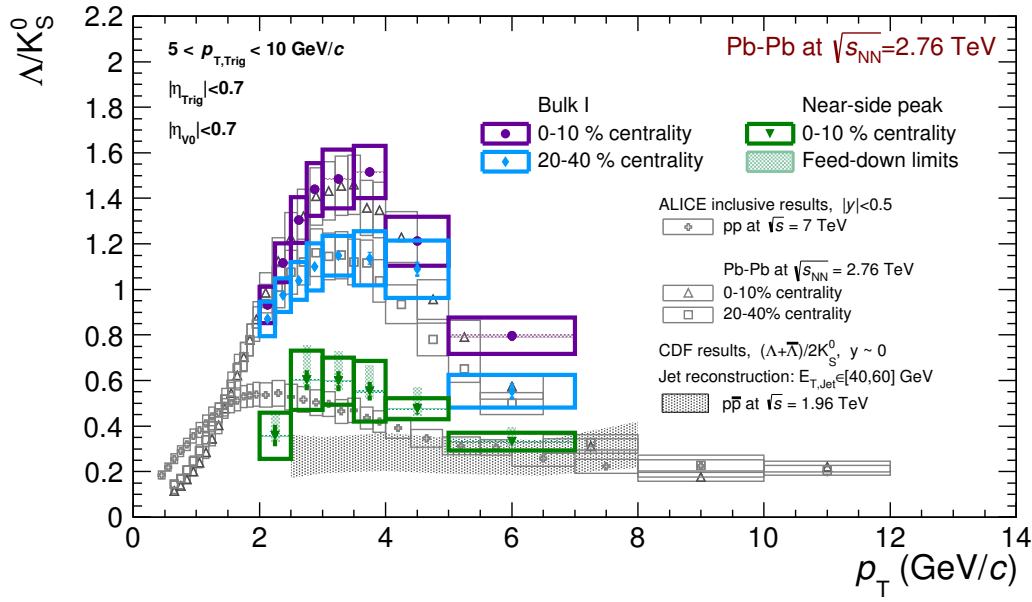
Figure 5.11: Λ/K_S^0 ratio in jet-like correlations in Pb–Pb collisions at $\sqrt{s_{NN}} = 2.76$ TeV measured within the ALICE Collaboration [69]. The ratios obtained in the near-side peak and the underlying event ("bulk") are compared with inclusive ratios in Pb–Pb and p–p collisions measured by ALICE and with ratios in reconstructed jets measured by the CDF Collaboration in p–$\bar{\text{p}}$ collisions at $\sqrt{s} = 1.96$ TeV.
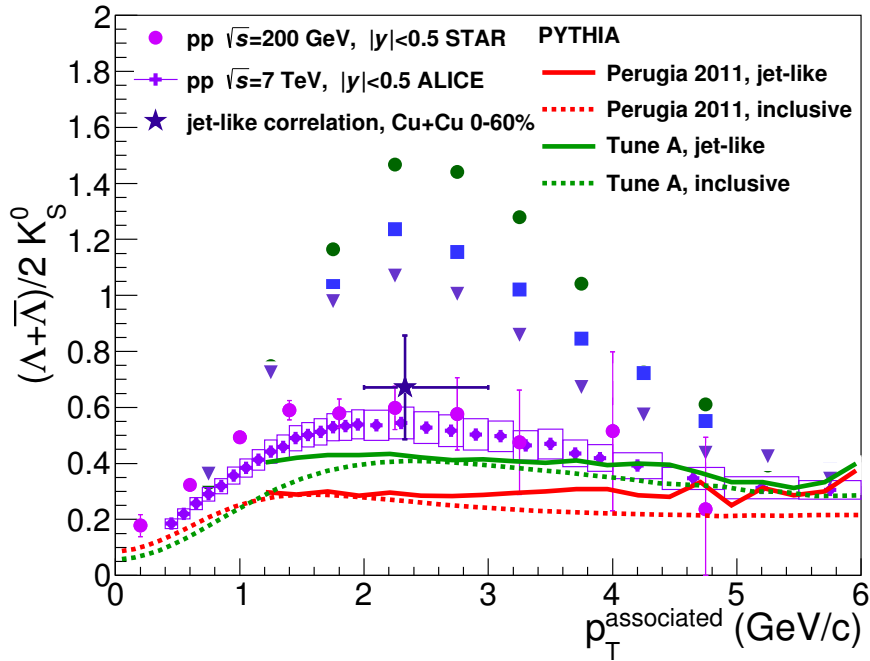
Figure 5.12: Λ/K_S^0 ratio in jet-like correlations in Cu–Cu collisions at $\sqrt{s_{NN}} = 200$ GeV in the centrality range 0–60 % measured by the STAR Collaboration [70]. The ratio obtained in the near-side peak is compared with inclusive ratios in p–p collisions measured by STAR and ALICE and with predictions of different PYTHIA tunes.
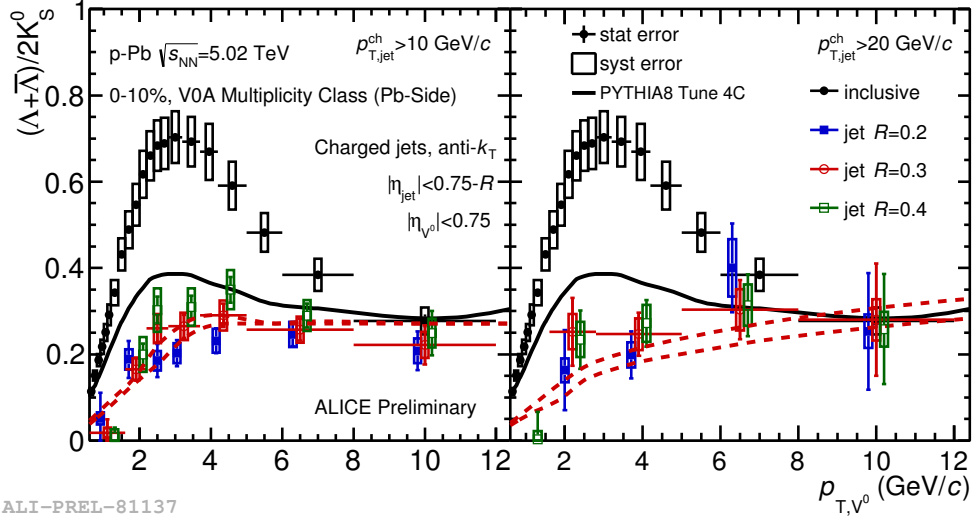
Figure 5.13: Λ/K_S^0 ratio in charged jets for $R = D = 0.2, 0.3, 0.4$ in p–Pb collisions at $\sqrt{s_{\mathrm{NN}}} = 5.02\,\mathrm{TeV}$ for $p_T^{\mathrm{jet,ch}} > 10\,\mathrm{GeV}/c$ (left) and $p_T^{\mathrm{jet,ch}} > 20\,\mathrm{GeV}/c$ (right), compared with the inclusive ratio in p–Pb and simulation results in p–p. The black solid line indicates the inclusive ratio from PYTHIA 8. The red dashed lines denote the spread of ratios in PYTHIA jets for all used values of R [71].

the measured inclusive ratio and with ratios obtained from the simulations of p–p collisions performed with PYTHIA 8. The measured baryon-to-meson ratio in jets in p–Pb collisions is below the inclusive ratio measured in p–Pb collisions, below the inclusive ratio measured in p–p collisions [115] (not shown) and also below the inclusive ratio obtained with PYTHIA simulations. Moreover, although PYTHIA underestimates the inclusive ratio in p–p collisions, the ratio measured in jets in p–Pb collisions exhibits a surprising similarity to the ratios of particles in jets simulated in PYTHIA. The ratio in jets does not evince any significant dependence on the p_T^{jet} threshold and only a mild dependence on R (or D).

The results of all three mentioned analyses deliver a coherent message, in agreement with the results of the analysis presented in this thesis, indicating that strangeness production in hard processes in larger collision systems compared to p–p collisions differs significantly from the strangeness production in soft processes associated with collective phenomena in collisions involving nuclei.

In order to evaluate whether jet fragmentation is modified in the relative production of strange hadrons in heavy-ion collisions and to what extent, the results would have to be compared with an appropriate reference which would be the Λ/K_S^0 ratio measured in jets in p–p collisions. Analyses dedicated to this task are already ongoing within the ALICE Collaboration.

5.4 Discussion

Although the current results presented in this thesis allow to draw conclusions about strangeness production in jets in heavy-ion collisions, there are several aspects of the analysis that could be further studied or improved.

Systematic uncertainties are greatly increased because of the discrepancy between simulated data for years 2010 and 2011 and by the discrepancy between

spectra of Λ and $\bar{\Lambda}$ particles. Solving these issues has a high priority also for other analyses within the ALICE Collaboration and would improve the significance of the results. In case a new Monte Carlo production would be required for the 2011 data, it might be beneficial to simulate a larger number of V^0 particles which would allow to apply the efficiency correction as a function of $p_T^{V^0}$ and η_{V^0} without increasing noticeably the statistical uncertainties of the results.

The main constraint of this analysis in terms of understanding the physics processes seems to be the accuracy of estimating and subtracting the contributions from the underlying event. The contamination by particles from background processes affects the reconstruction and selection of jets and also the extraction of spectra of particles in jets from the samples collected inside the jet cones. A more accurate determination of the level of the underlying event would provide a better stability of the Λ/K_S^0 ratio in jets with respect to the choice of the jet cone size and might enable reliable measurement of spectra in jets reconstructed with $R = 0.3$.

Other constraints are due to the limited available statistics in real data. With more data, one could afford applying stricter cuts on the selection of hard scatterings and further reduce the impact of the contamination by particles from the underlying event. If the number of V^0 particles collected in jet cones was larger, the signal extraction could be performed as a function of $p_T^{V^0}$ and η_{V^0} which would enable a direct application of the efficiency correction without any necessity for scaling of the η_{V^0} distributions. Larger statistics might also allow to perform the two-dimensional unfolding of the $p_T^{V^0}$–$p_T^{\text{jet,ch}}$ distributions that would provide a more accurate determination of the dependence of the V^0 spectra on jet momenta. Smaller statistical uncertainties would also facilitate the effort to distinguish systematic deviations from statistical fluctuations.

A potential effect of the underlying event on the directions of the reconstructed jets has been neglected in this analysis. The extent of such a modification could be studied using the 4-vector method of subtraction of the average p_T density of background ρ.

Some jets are rejected by the η acceptance requirement but fulfil the remaining criteria. Some of those signal jets overlap partially with the accepted region. Since this effect has not been taken into account, particles in these jets contribute to the underlying event estimation. It would be interesting to investigate whether excluding cones of the partially included jets would improve the agreement of different methods of estimating the spectra of V^0 particles in the underlying event.

In events where several jets are reconstructed and selected, it can occur that cones of some jets overlap. This cannot cause any V^0 particle to be considered in both jet cones but it might introduce a dependence of the particle spectra on the order in which jets are picked and it might slightly alter areas of the acceptance regions that should be considered for normalization of the spectra of particles in jet cones and in the underlying event. Based on the fraction of events containing several selected jets and the distribution of the distance between pairs of jets in those events, it has been concluded that cone overlapping concerns less than 1% of selected jets and therefore can be neglected.

The centrality distribution of events containing selected jets is slightly different from the centrality distribution of no-jet events. The events with selected jets

are on average biased towards more central events ($\langle c.\rangle = 4.80\,\%$ for $R = 0.2$) whereas the no-jet events are biased towards less central events ($\langle c.\rangle = 4.86\,\%$ for $R = 0.2$) compared to the overall distribution ($\langle c.\rangle = 4.85\,\%$). The effect of this difference is assumed to be reflected in the comparison of the spectra of particles in no-jet events with the other methods of estimating the underlying event using events with selected jets.

Azimuthal distributions of particles and jets in heavy-ion collisions are known to be modulated with respect to the reaction plane, determined by the impact parameter vector and the collision axis. The magnitude of this anisotropy is expressed by the "flow" coefficients v_n. A correction for this effect might be introduced by subtracting modulation contributions of the dominant terms v_2 and v_3.

Systematic uncertainties related to the cuts of the V^0 selection could be repeated with more variations, providing a distribution of results that could be characterized by a width that would be interpreted as the related systematic uncertainty.

Conclusions

The goal of this doctoral thesis was to study the production of neutral strange particles (K^0_S mesons and Λ baryons) in charged jets in Pb–Pb collisions in order to determine to what extent spectra of particles produced in hard scattering processes are modified in the context of the enhancement of the baryon-to-meson ratio observed for the inclusive production.

The analysis was performed using data recorded by the ALICE experiment at the LHC in central Pb–Pb collisions at the centre-of-mass energy of $\sqrt{s_{\mathrm{NN}}} = 2.76\,\mathrm{TeV}$.

Tracks of charged particles in the mid-rapidity region $|\eta| < 0.9$ were reconstructed using the Inner Tracking System and the Time-Projection Chamber. The centrality of collisions was estimated from the multiplicity of charged particles detected by scintillator arrays of the V0 detector placed at forward pseudorapidities.

Neutral strange particles were identified using the topology of their weak decays into charged particles. Combinatorial background was suppressed by applying cuts to the parameters of the decay vertex and the daughter tracks. The signal yields were extracted from the invariant-mass distributions of the selected particle candidates.

Charged jets were reconstructed by the anti-k_{t} algorithm using tracks of charged primary particles. The mean density of background coming from soft processes was estimated in each event from clusters reconstructed with the k_{t} algorithm and subtracted from the momentum of each jet. Jets were filtered by applying selection criteria on jet momentum, momentum of the leading track in the jet and jet area to further suppress the contribution of fake jets and to favour selection of hard scatterings instead.

Strange particles were associated with selected jets if found inside cones of a defined radius D around jet axes. The spectra of strange particles coming from the underlying event and contributing to the spectra of particles in jet cones were estimated using event regions without jet activity and were subtracted. The reconstruction efficiency of strange particles was determined using data from simulations of the passage of particles through the detectors. The spectra of K^0_S mesons and Λ baryons were corrected using their respective efficiencies. The spectra of particles in jets were further corrected by subtracting the estimated fraction of Λ particles coming from weak decays of jet constituents.

Systematic uncertainties were estimated by using parameter values and methods different from the default settings.

The spectra of K^0_S and Λ particles in jets were studied for transverse momenta in the range $2\,\mathrm{GeV}/c < p_{\mathrm{T}}^{\mathrm{V}^0} < 10\,\mathrm{GeV}/c$, for jets reconstructed with resolution parameters $R = 0.2, 0.3$, in two intervals of jet transverse momentum: $p_{\mathrm{T}}^{\mathrm{jet,ch}} > 10\,\mathrm{GeV}/c$, $p_{\mathrm{T}}^{\mathrm{jet,ch}} > 20\,\mathrm{GeV}/c$, and collected within jet cones of the default size $D = R$.

The magnitudes and shapes of spectra as a function of the minimum $p_{\mathrm{T}}^{\mathrm{jet}}$ indicate that softer jets consist of softer particles than harder jets and that more particles are produced in harder jets and/or harder jets are more collimated, which is in agreement with properties of jets measured in p–p collisions.

The spectra of particles in jets reconstructed with $R = 0.3$ are steeper than for $R = 0.2$ and lower at larger p_T^{V0} and their slopes do not seem to depend on the minimum p_T^{jet}. The differences between spectra of particles in jets reconstructed with different resolution parameters can be attributed to the differences between samples of selected jets and by increasing contamination by the underlying event as a function of increasing size of the jet cone.

The main results of this analysis consist in the comparison between the Λ/K_S^0 ratio in jets and the inclusive ratio. The Λ/K_S^0 ratio measured for particles in jets obtained with parameters $D = R = 0.2$ is significantly lower than the inclusive ratio and does not show any difference between the two p_T^{jet} intervals. The ratio is consistent with or slightly below the inclusive ratio in p–p collisions and meets with the inclusive ratio in Pb–Pb collisions at higher p_T^{V0} where the hadron production starts to be dominated by jet fragmentation. These results indicate that jet fragmentation in the studied sample of jets is not (significantly) modified in the relative production of Λ baryons and K_S^0 mesons. The enhancement of the inclusive Λ/K_S^0 ratio is therefore predominantly coming from collective phenomena associated with soft processes in high-multiplicity collisions.

The conclusions drawn from the presented results are compatible with the findings of other analyses addressing the enhancement of the Λ/K_S^0 ratio in Pb–Pb and p–Pb collisions at the LHC as well as in Cu–Cu collisions at RHIC. However, a direct comparison with the reference provided by the measurement of the Λ/K_S^0 ratio in jets in p–p collisions will be essential to evaluate whether there is a component of the enhancement coming from modified jet fragmentation.

Bibliography

[1] K. A. Olive, et al. (Particle Data Group). "Review of Particle Physics". Chin. Phys. C **38** (2014) 090001. `doi:10.1088/1674-1137/38/9/090001`.

[2] G. Dissertori, I. G. Knowles, M. Schmelling. Quantum Chromodynamics: High Energy Experiments and Theory. International Series of Monographs on Physics. Oxford University Press, 2009. `doi:10.1093/acprof:oso/9780199566419.001.0001`.

[3] U. W. Heinz. "Concepts of Heavy-Ion Physics". In "2002 European School of High-Energy Physics, Pylos, Greece, 25 Aug – 7 Sep 2002: Proceedings", pp. 127–178. 2004. URL: `http://cds.cern.ch/record/735568`, `arXiv:hep-ph/0407360`, `doi:10.5170/CERN-2004-001.127`.

[4] J. Wambach. "Phases of Strongly-Interacting Matter" [online]. 2009. Presentation. URL: `http://physik.uni-graz.at/~dk-user/talks/Wambach20090119.pdf` [cited 2016-07-06].

[5] S. Borsányi, et al. (Wuppertal–Budapest Collaboration). "Is there still any T_c mystery in lattice QCD? Results with physical masses in the continuum limit III". JHEP **09** (2010) 073. `arXiv:1005.3508`, `doi:10.1007/JHEP09(2010)073`.

[6] A. Bazavov, et al. "The chiral and deconfinement aspects of the QCD transition". Phys. Rev. D **85** (2012) 054503. `arXiv:1111.1710`, `doi:10.1103/PhysRevD.85.054503`.

[7] K. Yagi, T. Hatsuda, Y. Miake. Quark–Gluon Plasma: From Big Bang to Little Bang. Cambridge Monographs on Particle Physics, Nuclear Physics and Cosmology. Cambridge University Press, 2008.

[8] U. W. Heinz, M. Jacob. "Evidence for a New State of Matter: An Assessment of the Results from the CERN Lead Beam Programme" `arXiv:nucl-th/0002042`.

[9] CERN. "CERN Press Release – New State of Matter created at CERN" [online]. 2000. URL: `http://press-archive.web.cern.ch/press-archive/PressReleases/Releases2000/PR01.00EQuarkGluonMatter.html` [cited 2016-07-07].

[10] RHIC. "'Perfect' Liquid Hot Enough to be Quark Soup" [online]. 2010. URL: `https://www.bnl.gov/rhic/news2/news.asp?a=1074&t=pr` [cited 2016-07-07].

[11] B. Abelev, et al. (ALICE Collaboration). "Centrality determination of Pb–Pb collisions at $\sqrt{s_{\mathrm{NN}}} = 2.76\,\mathrm{TeV}$ with ALICE". Phys. Rev. C **88**, no. 4 (2013) 044909. `arXiv:1301.4361`, `doi:10.1103/PhysRevC.88.044909`.

[12] R. J. Glauber. "High-Energy Collision Theory". In W. E. Brittin, L. G. Dunham (editors) "Lectures in Theoretical Physics", volume 1, pp. 315–414. Interscience, New York, 1959.

[13] M. L. Miller, K. Reygers, S. J. Sanders, P. Steinberg. "Glauber modeling in high energy nuclear collisions". Ann. Rev. Nucl. Part. Sci. **57** (2007) 205–243. `arXiv:nucl-ex/0701025`, `doi:10.1146/annurev.nucl.57.090506.123020`.

[14] B. Alessandro, et al. (ALICE Collaboration). "ALICE: Physics Performance Report, volume II". J. Phys. G **32** (2006) 1295–2040. `doi:10.1088/0954-3899/32/10/001`.

[15] D. d'Enterria. "Jet quenching". Landolt–Börnstein **23** (2010) 471. `arXiv:0902.2011`, `doi:10.1007/978-3-642-01539-7_16`.

[16] N. Armesto, et al. "Comparison of jet quenching formalisms for a quark–gluon plasma "brick"". Phys. Rev. C **86** (2012) 064904. `arXiv:1106.1106`, `doi:10.1103/PhysRevC.86.064904`.

[17] R. Baier, Y. L. Dokshitzer, A. H. Mueller, S. Peigné, D. Schiff. "The Landau–Pomeranchuk–Migdal effect in QED". Nucl. Phys. B **478** (1996) 577–597. `arXiv:hep-ph/9604327`, `doi:10.1016/0550-3213(96)00426-9`.

[18] R. Baier, Y. L. Dokshitzer, A. H. Mueller, S. Peigné, D. Schiff. "Radiative energy loss of high energy quarks and gluons in a finite-volume quark–gluon plasma". Nucl. Phys. B **483** (1997) 291–320. `arXiv:hep-ph/9607355`, `doi:10.1016/S0550-3213(96)00553-6`.

[19] R. Baier, Y. L. Dokshitzer, A. H. Mueller, S. Peigné, D. Schiff. "Radiative energy loss and $p_\perp$-broadening of high energy partons in nuclei". Nucl. Phys. B **484** (1997) 265–282. `arXiv:hep-ph/9608322`, `doi:10.1016/S0550-3213(96)00581-0`.

[20] R. Baier, D. Schiff, B. G. Zakharov. "Energy loss in perturbative QCD". Ann. Rev. Nucl. Part. Sci. **50** (2000) 37–69. `arXiv:hep-ph/0002198`, `doi:10.1146/annurev.nucl.50.1.37`.

[21] R. Baier, Y. L. Dokshitzer, S. Peigné, D. Schiff. "Induced gluon radiation in a QCD medium". Phys. Lett. B **345** (1995) 277–286. `arXiv:hep-ph/9411409`, `doi:10.1016/0370-2693(94)01617-L`.

[22] C. A. Salgado, U. A. Wiedemann. "Calculating quenching weights". Phys. Rev. D **68** (2003) 014008. `arXiv:hep-ph/0302184`, `doi:10.1103/PhysRevD.68.014008`.

[23] T. Renk, H. Holopainen, R. Paatelainen, K. J. Eskola. "Systematics of the charged-hadron P_T spectrum and the nuclear suppression factor in heavy-ion collisions from $\sqrt{s_{\mathrm{NN}}} = 200\,\mathrm{GeV}$ to $\sqrt{s_{\mathrm{NN}}} = 2.76\,\mathrm{TeV}$". Phys. Rev. C **84** (2011) 014906. `arXiv:1103.5308`, `doi:10.1103/PhysRevC.84.014906`.

[24] K. Werner, I. Karpenko, M. Bleicher, T. Pierog, S. Porteboeuf-Houssais. "Jets, bulk matter, and their interaction in heavy ion collisions at several TeV". Phys. Rev. C **85** (2012) 064907. `arXiv:1203.5704`, `doi:10.1103/PhysRevC.85.064907`.

[25] M. Gyulassy, P. Lévai, I. Vitev. "Reaction operator approach to non-Abelian energy loss". Nucl. Phys. B **594** (2001) 371–419. `arXiv:nucl-th/0006010`, `doi:10.1016/S0550-3213(00)00652-0`.

[26] M. Djordjevic, M. Gyulassy. "Heavy quark radiative energy loss in QCD matter". Nucl. Phys. A **733** (2004) 265–298. `arXiv:nucl-th/0310076`, `doi:10.1016/j.nuclphysa.2003.12.020`.

[27] X.-f. Guo, X.-N. Wang. "Multiple scattering, parton energy loss and modified fragmentation functions in deeply inelastic eA scattering". Phys. Rev. Lett. **85** (2000) 3591–3594. `arXiv:hep-ph/0005044`, `doi:10.1103/PhysRevLett.85.3591`.

[28] X.-N. Wang, X.-f. Guo. "Multiple parton scattering in nuclei: Parton energy loss". Nucl. Phys. A **696** (2001) 788–832. `arXiv:hep-ph/0102230`, `doi:10.1016/S0375-9474(01)01130-7`.

[29] P. B. Arnold, G. D. Moore, L. G. Yaffe. "Transport coefficients in high temperature gauge theories, 1. Leading-log results". JHEP **11** (2000) 001. `arXiv:hep-ph/0010177`, `doi:10.1088/1126-6708/2000/11/001`.

[30] P. B. Arnold, G. D. Moore, L. G. Yaffe. "Photon emission from ultrarelativistic plasmas". JHEP **11** (2001) 057. `arXiv:hep-ph/0109064`, `doi:10.1088/1126-6708/2001/11/057`.

[31] B. Andersson, G. Gustafson, G. Ingelman, T. Sjöstrand. "Parton Fragmentation and String Dynamics". Phys. Rept. **97** (1983) 31–145. `doi:10.1016/0370-1573(83)90080-7`.

[32] T. Sjöstrand. "Jet Fragmentation of Nearby Partons". Nucl. Phys. B **248** (1984) 469–502. `doi:10.1016/0550-3213(84)90607-2`.

[33] B. R. Webber. "A QCD Model for Jet Fragmentation Including Soft Gluon Interference". Nucl. Phys. B **238** (1984) 492–528. `doi:10.1016/0550-3213(84)90333-X`.

[34] K. Adcox, et al. (PHENIX Collaboration). "Suppression of Hadrons with Large Transverse Momentum in Central Au + Au Collisions at $\sqrt{s_{NN}} = 130\,\text{GeV}$". Phys. Rev. Lett. **88** (2001) 022301. `arXiv:nucl-ex/0109003`, `doi:10.1103/PhysRevLett.88.022301`.

[35] C. Adler, et al. (STAR Collaboration). "Centrality dependence of high p_T hadron suppression in Au + Au collisions at $\sqrt{s_{NN}} = 130\,\text{GeV}$". Phys. Rev. Lett. **89** (2002) 202301. `arXiv:nucl-ex/0206011`, `doi:10.1103/PhysRevLett.89.202301`.

[36] J. Adams, et al. (STAR Collaboration). "Evidence from d + Au measurements for final state suppression of high p_T hadrons in Au + Au collisions at RHIC". Phys. Rev. Lett. **91** (2003) 072304. `arXiv:nucl-ex/0306024`, `doi:10.1103/PhysRevLett.91.072304`.

[37] J. Adams, et al. (STAR Collaboration). "Direct Observation of Dijets in Central Au + Au Collisions at $\sqrt{s_{NN}} = 200\,\text{GeV}$". Phys. Rev. Lett. **97** (2006) 162301. `arXiv:nucl-ex/0604018, doi:10.1103/PhysRevLett.97.162301`.

[38] A. Adare, et al. (PHENIX Collaboration). "Trends in Yield and Azimuthal Shape Modification in Dihadron Correlations in Relativistic Heavy Ion Collisions". Phys. Rev. Lett. **104** (2010) 252301. `arXiv:1002.1077, doi:10.1103/PhysRevLett.104.252301`.

[39] C. Adler, et al. (STAR Collaboration). "Disappearance of Back-To-Back High-p_T Hadron Correlations in Central Au + Au collisions at $\sqrt{s_{NN}} = 200\,\text{GeV}$". Phys. Rev. Lett. **90** (2003) 082302. `arXiv:nucl-ex/0210033, doi:10.1103/PhysRevLett.90.082302`.

[40] M. Płoskoń (STAR Collaboration). "Inclusive cross section and correlations of fully reconstructed jets in $\sqrt{s_{NN}} = 200\,\text{GeV}$ Au+Au and p+p collisions". Nucl. Phys. A **830** (2009) 255C–258C. `arXiv:0908.1799, doi:10.1016/j.nuclphysa.2009.10.095`.

[41] G. Aad, et al. (ATLAS Collaboration). "Observation of a Centrality-Dependent Dijet Asymmetry in Lead–Lead Collisions at $\sqrt{s_{NN}} = 2.76\,\text{TeV}$ with the ATLAS Detector at the LHC". Phys. Rev. Lett. **105** (2010) 252303. `arXiv:1011.6182, doi:10.1103/PhysRevLett.105.252303`.

[42] K. Aamodt, et al. (ALICE Collaboration). "Suppression of charged particle production at large transverse momentum in central Pb–Pb collisions at $\sqrt{s_{NN}} = 2.76\,\text{TeV}$". Phys. Lett. B **696** (2011) 30–39. `arXiv:1012.1004, doi:10.1016/j.physletb.2010.12.020`.

[43] S. Chatrchyan, et al. (CMS Collaboration). "Observation and studies of jet quenching in PbPb collisions at $\sqrt{s_{NN}} = 2.76\,\text{TeV}$". Phys. Rev. C **84** (2011) 024906. `arXiv:1102.1957, doi:10.1103/PhysRevC.84.024906`.

[44] CMS Collaboration. "Centrality dependence of the nuclear modification factor for charged particle transverse momentum spectra in PbPb collisions at $\sqrt{s_{NN}} = 2.76\,\text{TeV}$". Technical Report CMS-PAS-HIN-10-005, CERN, Geneva, 2011. URL: `http://cds.cern.ch/record/1352777`.

[45] B. Abelev, et al. (ALICE Collaboration). "Measurement of charged jet suppression in Pb–Pb collisions at $\sqrt{s_{NN}} = 2.76\,\text{TeV}$". JHEP **1403** (2014) 013. `arXiv:1311.0633, doi:10.1007/JHEP03(2014)013`.

[46] G. C. Blazey, et al. "Run II Jet Physics". In "QCD and weak boson physics in Run II. Proceedings, Batavia, USA, March 4–6, June 3–4, November 4–6, 1999", pp. 47–77. 2000. URL: `http://lss.fnal.gov/cgi-bin/find_paper.pl?conf-00-092`, `arXiv:hep-ex/0005012`.

[47] J. E. Huth, et al. "Toward a Standardization of Jet Definitions". In "Proceedings of the 1990 Summer Study on High Energy Physics: Research Directions for the Decade, Snowmass, Colorado, June 25 – July 13, 1990",

pp. 134–136. 1990. URL: `http://lss.fnal.gov/cgi-bin/find_paper.pl?conf-90-249`.

[48] M. Cacciari, G. P. Salam, G. Soyez. "The anti-k_t jet clustering algorithm". JHEP **0804** (2008) 063. `arXiv:0802.1189, doi:10.1088/1126-6708/2008/04/063`.

[49] S. Catani, Y. L. Dokshitzer, M. H. Seymour, B. R. Webber. "Longitudinally-invariant $k_\perp$-clustering algorithms for hadron–hadron collisions". Nucl. Phys. B **406** (1993) 187–224. `doi:10.1016/0550-3213(93)90166-M`.

[50] S. Sapeta, U. A. Wiedemann. "Jet hadrochemistry as a characteristics of jet quenching". Eur. Phys. J. C **55** (2008) 293–302. `arXiv:0707.3494, doi:10.1140/epjc/s10052-008-0592-8`.

[51] R. J. Fries, B. Müller, C. Nonaka, S. A. Bass. "Hadronization in Heavy-Ion Collisions: Recombination and Fragmentation of Partons". Phys. Rev. Lett. **90** (2003) 202303. `arXiv:nucl-th/0301087, doi:10.1103/PhysRevLett.90.202303`.

[52] S. A. Voloshin. "Anisotropic flow". Nucl. Phys. A **715** (2003) 379–388. `arXiv:nucl-ex/0210014, doi:10.1016/S0375-9474(02)01450-1`.

[53] R. J. Fries, V. Greco, P. Sorensen. "Coalescence Models for Hadron Formation from Quark–Gluon Plasma". Ann. Rev. Nucl. Part. Sci. **58** (2008) 177–205. `arXiv:0807.4939, doi:10.1146/annurev.nucl.58.110707.171134`.

[54] R. J. Fries, B. Müller, C. Nonaka, S. A. Bass. "Hadron production in heavy ion collisions: Fragmentation and recombination from a dense parton phase". Phys. Rev. C **68** (2003) 044902. `arXiv:nucl-th/0306027, doi:10.1103/PhysRevC.68.044902`.

[55] V. Greco, C. M. Ko, P. Lévai. "Parton coalescence and anti-proton/pion anomaly at RHIC". Phys. Rev. Lett. **90** (2003) 202302. `arXiv:nucl-th/0301093, doi:10.1103/PhysRevLett.90.202302`.

[56] V. Greco, C. M. Ko, P. Lévai. "Parton coalescence at RHIC". Phys. Rev. C **68** (2003) 034904. `arXiv:nucl-th/0305024, doi:10.1103/PhysRevC.68.034904`.

[57] V. Greco, C. M. Ko, I. Vitev. "Hadron production from quark coalescence and jet fragmentation in intermediate energy collisions at RHIC". Phys. Rev. C **71** (2005) 041901. `arXiv:nucl-th/0412043, doi:10.1103/PhysRevC.71.041901`.

[58] R. C. Hwa, C. B. Yang. "Scaling behavior at high p_T and the p/π ratio". Phys. Rev. C **67** (2003) 034902. `arXiv:nucl-th/0211010, doi:10.1103/PhysRevC.67.034902`.

[59] R. C. Hwa, C. B. Yang. "Recombination of shower partons at high p_T in heavy-ion collisions". Phys. Rev. C **70** (2004) 024905. `arXiv:nucl-th/0401001, doi:10.1103/PhysRevC.70.024905`.

[60] R. C. Hwa, C. B. Yang. "Production of strange particles at intermediate p_T in central Au + Au collisions at high energies". Phys. Rev. C **75** (2007) 054904. `arXiv:nucl-th/0602024`, `doi:10.1103/PhysRevC.75.054904`.

[61] B. I. Abelev, et al. (STAR Collaboration). "Identified Baryon and Meson Distributions at Large Transverse Momenta from Au + Au collisions at $\sqrt{s_{\mathrm{NN}}} = 200\,\mathrm{GeV}$". Phys. Rev. Lett. **97** (2006) 152301. `arXiv:nucl-ex/0606003`, `doi:10.1103/PhysRevLett.97.152301`.

[62] M. Lamont (STAR Collaboration). "Identified particles at large transverse momenta in STAR in Au + Au collisions @ $\sqrt{s_{\mathrm{NN}}} = 200\,\mathrm{GeV}$". J. Phys. G **30** (2004) S963–S968. `arXiv:nucl-ex/0403059`, `doi:10.1088/0954-3899/30/8/039`.

[63] J. Adams, et al. (STAR Collaboration, STAR-RICH Collaboration). "Measurements of identified particles at intermediate transverse momentum in the STAR experiment from Au + Au collisions at $\sqrt{s_{\mathrm{NN}}} = 200\,\mathrm{GeV}$" `arXiv:nucl-ex/0601042`.

[64] B. Abelev, et al. (ALICE Collaboration). "K_S^0 and Λ Production in Pb–Pb Collisions at $\sqrt{s_{\mathrm{NN}}} = 2.76\,\mathrm{TeV}$". Phys. Rev. Lett. **111** (2013) 222301. `arXiv:1307.5530`, `doi:10.1103/PhysRevLett.111.222301`.

[65] B. Abelev, et al. (ALICE Collaboration). "Multiplicity dependence of pion, kaon, proton and lambda production in p–Pb collisions at $\sqrt{s_{\mathrm{NN}}} = 5.02\,\mathrm{TeV}$". Phys. Lett. B **728** (2014) 25–38. `arXiv:1307.6796`, `doi:10.1016/j.physletb.2013.11.020`.

[66] C. Shen, U. Heinz, P. Huovinen, H. Song. "Radial and elliptic flow in Pb + Pb collisions at energies available at the CERN Large Hadron Collider from viscous hydrodynamics". Phys. Rev. C **84** (2011) 044903. `arXiv:1105.3226`, `doi:10.1103/PhysRevC.84.044903`.

[67] R. J. Fries, V. Greco, P. Sorensen. "Coalescence Models for Hadron Formation from Quark–Gluon Plasma". Ann. Rev. Nucl. Part. Sci. **58** (2008) 177–205. `arXiv:0807.4939`, `doi:10.1146/annurev.nucl.58.110707.171134`.

[68] K. Werner. "Lambda-to-Kaon Ratio Enhancement in Heavy Ion Collisions at Several TeV". Phys. Rev. Lett. **109** (2012) 102301. `arXiv:1204.1394`, `doi:10.1103/PhysRevLett.109.102301`.

[69] X. Sánchez Castro, C. Kuhn. K_S^0 and Λ production associated to high-p_T particles in Pb–Pb collisions at $\sqrt{s_{\mathrm{NN}}} = 2.76\,\mathrm{TeV}$ with ALICE: Comparison between soft- and hard-processes in hadron production. Ph.D. thesis, Strasbourg U., 2015. Presented 31 Mar 2015. URL: `http://cds.cern.ch/record/2043201`.

[70] B. Abelev, et al. (STAR Collaboration). "Near-side azimuthal and pseudorapidity correlations using neutral strange baryons and mesons in d + Au, Cu + Cu and Au + Au collisions at $\sqrt{s_{\mathrm{NN}}} = 200\,\mathrm{GeV}$" `arXiv:1603.05477`.

[71] X. Zhang (ALICE Collaboration). "K_S^0 and Λ production in charged particle jets in p–Pb collisions at $\sqrt{s_{NN}} = 5.02\,\text{TeV}$ with ALICE". Nucl. Phys. A **931** (2014) 444–448. `arXiv:1408.2672`, `doi:10.1016/j.nuclphysa.2014.08.102`.

[72] K. Aamodt, et al. (ALICE Collaboration). "The ALICE experiment at the CERN LHC". JINST **3** (2008) S08002. `doi:10.1088/1748-0221/3/08/S08002`.

[73] ALICE Collaboration. "41 countries, 174 institutes, approx. 1852 members | ALICE Collaboration" [online]. URL: `https://alice-collaboration.web.cern.ch/general/index.html` [cited 2016-08-19].

[74] ALICE Collaboration. "3D ALICE Schematic - with Description | ALICE Figure Repository" [online]. URL: `https://aliceinfo.cern.ch/Figure/node/3400`.

[75] B. Abelev, et al. (ALICE Collaboration). "Performance of the ALICE Experiment at the CERN LHC". Int. J. Mod. Phys. A **29** (2014) 1430044. `arXiv:1402.4476`, `doi:10.1142/S0217751X14300440`.

[76] K. Aamodt, et al. (ALICE Collaboration). "Alignment of the ALICE Inner Tracking System with cosmic-ray tracks". JINST **5** (2010) P03003. `arXiv:1001.0502`, `doi:10.1088/1748-0221/5/03/P03003`.

[77] F. Carminati, et al. (ALICE Collaboration). "ALICE: Physics Performance Report, Volume I". J. Phys. G **30** (2004) 1517–1763. `doi:10.1088/0954-3899/30/11/001`.

[78] J. Alme, et al. "The ALICE TPC, a large 3-dimensional tracking device with fast readout for ultra-high multiplicity events". Nucl. Instrum. Meth. A **622** (2010) 316–367. `arXiv:1001.1950`, `doi:10.1016/j.nima.2010.04.042`.

[79] M. Ivanov (ALICE Collaboration). "Identified charged hadron production measured with ALICE at the LHC". Nucl. Phys. A **904**–**905** (2013) 162c–169c. `doi:10.1016/j.nuclphysa.2013.01.058`.

[80] E. Abbas, et al. (ALICE Collaboration). "Performance of the ALICE VZERO system". JINST **8** (2013) P10016. `arXiv:1306.3130`, `doi:10.1088/1748-0221/8/10/P10016`.

[81] P. Cortese, et al. (ALICE Collaboration). "ALICE Electromagnetic Calorimeter Technical Design Report". Technical Report CERN-LHCC-2008-014. ALICE-TDR-14, CERN, Geneva, 2008. URL: `https://cds.cern.ch/record/1121574`.

[82] J. Allen, et al. "ALICE DCal: An Addendum to the EMCal Technical Design Report Di-Jet and Hadron-Jet correlation measurements in ALICE". Technical Report CERN-LHCC-2010-011. ALICE-TDR-14-add-1, CERN, Geneva, 2010. URL: `https://cds.cern.ch/record/1272952`.

[83] K. Aamodt, et al. (ALICE Collaboration). "Centrality dependence of the charged-particle multiplicity density at mid-rapidity in Pb–Pb collisions at $\sqrt{s_{NN}} = 2.76\,\text{TeV}$". Phys. Rev. Lett. **106** (2011) 032301. `arXiv:1012.1657`, `doi:10.1103/PhysRevLett.106.032301`.

[84] ALICE Collaboration. "Welcome | ITS Upgrade" [online]. URL: `http://aliceinfo.cern.ch/ITSUpgrade/` [cited 2016-06-23].

[85] B. Abelev, et al. (ALICE Collaboration). "Technical Design Report for the Upgrade of the ALICE Inner Tracking System". J. Phys. G **41** (2014) 087002. URL: `https://cds.cern.ch/record/1625842`, `doi:10.1088/0954-3899/41/8/087002`.

[86] ALICE ITS ALPIDE development team. "pALPIDEfs datasheet" [online]. version 1.0b. URL: `https://indico.cern.ch/event/309388/contribution/0/material/0/0.pdf`.

[87] ALICE Collaboration. "ITS upgrade characterisation" [online]. Meeting of the working group WP5. URL: `https://indico.cern.ch/event/452785/`.

[88] ALICE Collaboration. "ITS upgrade characterisation" [online]. Meeting of the working group WP5. URL: `https://indico.cern.ch/event/475249/`.

[89] L. S. Barnby, et al. (ALICE Collaboration). "Measurement of K_S^0 and Λ spectra and yields in Pb–Pb collisions at $\sqrt{s_{NN}} = 2.76\,\text{TeV}$ with the ALICE experiment" [online]. Analysis note. URL: `https://aliceinfo.cern.ch/Notes/node/88`.

[90] ALICE Collaboration. "2011 Pb–Pb track QA" [online]. URL: `https://twiki.cern.ch/twiki/bin/viewauth/ALICE/JELHC11hTrackQA`.

[91] D. Keijdener (ALICE Collaboration). "QA LHC11h PbPb Data, AOD 145 (extended)" [online]. URL: `https://indico.cern.ch/event/310177/contribution/0/material/slides/0.pdf`.

[92] J. Bielčíková (ALICE Collaboration). "Update on track QA of Run 2011 Pb + Pb data" [online]. URL: `https://indico.cern.ch/getFile.py/access?contribId=3&resId=0&materialId=slides&confId=181339`.

[93] ALICE Collaboration. "Run Condition Table" [online]. URL: `http://alimonitor.cern.ch/configuration/index.jsp?partition=LHC11h&pass=2`.

[94] ALICE Collaboration. "MonALISA Repository for ALICE" [online]. URL: `http://alimonitor.cern.ch/`.

[95] R. Brun, F. Rademakers. "ROOT – An object oriented data analysis framework". Nucl. Inst. & Meth. in Phys. Res. A **389**, no. 1–2 (1997) 81–86. URL: `http://root.cern.ch/`, `doi:10.1016/S0168-9002(97)00048-X`.

[96] ALICE Collaboration. "PUB CERN central GIT service - AliRoot.git/summary" [online]. ALICE Offline framework for simulation, reconstruction and analysis. URL: `http://git.cern.ch/pubweb/AliRoot.git`.

[97] ALICE Collaboration. "PUB CERN central GIT service - AliPhysics.git/summary" [online]. ALICE Offline physics working groups repository. URL: `http://git.cern.ch/pubweb/AliPhysics.git`.

[98] M. Cacciari, G. P. Salam, G. Soyez. "FastJet user manual". Eur. Phys. J. C **72** (2012) 1896. `arXiv:1111.6097, doi:10.1140/epjc/s10052-012-1896-2`.

[99] "FastJet Contrib" [online]. 3rd party extensions of FastJet. URL: `https://fastjet.hepforge.org/contrib/`.

[100] T. Sjöstrand, S. Mrenna, P. Z. Skands. "PYTHIA 6.4 physics and manual". JHEP **0605** (2006) 026. `arXiv:hep-ph/0603175, doi:10.1088/1126-6708/2006/05/026`.

[101] T. Sjöstrand, S. Mrenna, P. Z. Skands. "A brief introduction to PYTHIA 8.1". Comput. Phys. Commun. **178** (2008) 852–867. `arXiv:0710.3820, doi:10.1016/j.cpc.2008.01.036`.

[102] V. Kučera (ALICE Collaboration). "AliAnalysisTaskV0sInJetsEmcal" [online]. Analysis task for the analysis of K_S^0 and (anti-)Λ in charged jets using the EMCal framework. Documentation at `http://aliroot-docs.web.cern.ch/aliroot-docs/AliAnalysisTaskV0sInJetsEmcal.html`. URL: `http://git.cern.ch/pubweb/AliPhysics.git/blob/HEAD:/PWGJE/EMCALJetTasks/UserTasks/AliAnalysisTaskV0sInJetsEmcal.cxx`.

[103] V. Kučera (ALICE Collaboration). "AliAnalysisTaskV0sInJets" [online]. Analysis task for the analysis of K_S^0 and (anti-)Λ in charged jets using the JETAN framework. Documentation at `http://aliroot-docs.web.cern.ch/aliroot-docs/AliAnalysisTaskV0sInJets.html`. URL: `http://git.cern.ch/pubweb/AliPhysics.git/blob/HEAD:/PWGJE/StrangenessInJets/AliAnalysisTaskV0sInJets.cxx`.

[104] A. Zimmermann (ALICE Collaboration). "AliAnalysisTaskJetChem" [online]. Analysis task for the analysis of K_S^0 and (anti-)Λ in charged jets using the JETAN framework. Documentation at `http://aliroot-docs.web.cern.ch/aliroot-docs/AliAnalysisTaskJetChem.html`. URL: `http://git.cern.ch/pubweb/AliPhysics.git/blob/HEAD:/PWGJE/StrangenessInJets/AliAnalysisTaskJetChem.cxx`.

[105] J. Podolanski, R. Armenteros. "III. Analysis of V-events". Phil. Mag. **45** (1954) 13–30. `doi:10.1080/14786440108520416`.

[106] ALICE Collaboration. "Hybrid Tracks" [online]. URL: `https://twiki.cern.ch/twiki/bin/viewauth/ALICE/HybridTracks`.

[107] C. Loizides, M. Verweij, S. Aiola (ALICE Collaboration). "AliEmcalJetTask" [online]. General jet finder task. URL: `http://git.cern.ch/pubweb/AliPhysics.git/blob/HEAD:/PWGJE/EMCALJetTasks/AliEmcalJetTask.cxx`.

117

[108] M. Cacciari, G. P. Salam, G. Soyez. "The catchment area of jets". JHEP **04** (2008) 005. `arXiv:0802.1188, doi:10.1088/1126-6708/2008/04/005`.

[109] B. Abelev, et al. (ALICE Collaboration). "Measurement of Event Background Fluctuations for Charged Particle Jet Reconstruction in Pb–Pb collisions at $\sqrt{s_{NN}} = 2.76\,\text{TeV}$". JHEP **1203** (2012) 053. `arXiv:1201.2423, doi:10.1007/JHEP03(2012)053`.

[110] M. Cacciari, J. Rojo, G. P. Salam, G. Soyez. "Jet Reconstruction in Heavy Ion Collisions". Eur. Phys. J. C **71** (2011) 1539. `arXiv:1010.1759, doi: 10.1140/epjc/s10052-011-1539-z`.

[111] M. Cacciari, G. P. Salam. "Pileup subtraction using jet areas". Phys. Lett. B **659** (2008) 119–126. `arXiv:0707.1378, doi:10.1016/j.physletb.2007. 09.077`.

[112] B. B. Abelev, et al. (ALICE Collaboration). "Multi-strange baryon production at mid-rapidity in Pb–Pb collisions at $\sqrt{s_{NN}} = 2.76\,\text{TeV}$". Phys. Lett. B **728** (2014) 216–227. [Erratum: Phys. Lett. B **734** (2014) 409–410, doi:10.1016/j.physletb.2014.05.052]. `arXiv:1307.5543, doi:10.1016/ j.physletb.2013.11.048`.

[113] D. Elia (ALICE Collaboration). "Measurement of multi-strange baryons in Pb–Pb collisions at $\sqrt{s_{NN}} = 2.76\,\text{TeV}$" [online]. Analysis note. URL: `https://aliceinfo.cern.ch/Notes/node/48`.

[114] R. Barlow. "Systematic Errors: Facts and Fictions". In M. Whalley, L. Lyons (editors) "Advanced Statistical Techniques in Particle Physics. Proceedings, Conference, Durham, UK, March 18–22, 2002", pp. 134–144. Inst. For Particle Physics Phenomenology, Durham, UK, 2002. URL: `http://www.ippp.dur.ac.uk/Workshops/02/statistics/ proceedings/barlow.pdf`, `arXiv:hep-ex/0207026`.

[115] K. Aamodt, et al. (ALICE Collaboration). "Strange particle production in proton–proton collisions at $\sqrt{s} = 0.9\,\text{TeV}$ with ALICE at the LHC". Eur. Phys. J. C **71** (2011) 1594. `arXiv:1012.3257, doi:10.1140/epjc/ s10052-011-1594-5`.

[116] B. B. Abelev, et al. (ALICE Collaboration). "Charged jet cross sections and properties in proton–proton collisions at $\sqrt{s} = 7\,\text{TeV}$". Phys. Rev. D **91**, no. 11 (2015) 112012. `arXiv:1411.4969, doi:10.1103/PhysRevD.91. 112012`.

[117] T. Aaltonen, et al. (CDF Collaboration). "Production of K_S^0, $K^{*\pm}(892)$ and $\varphi^0(1020)$ in minimum bias events and K_S^0 and Λ^0 in jets in $p\overline{p}$ collisions at $\sqrt{s} = 1.96\,\text{TeV}$". Phys. Rev. D **88** (2013) 092005. `arXiv:1308.3371, doi:10.1103/PhysRevD.88.092005`.

List of Figures

List of Tables